TESI DI DOTTORATO

UNIVERSITA' DEGLI STUDI DI NAPOLI FEDERICO II

DIPARTIMENTO DI INGEGNERIA ELETTRONICA

E DELLE TELECOMUNICAZIONI

DOTTORATO DI RICERCA IN

INGEGNERIA ELETTRONICA E DELLE TELECOMUNICAZIONI

Design, Realization and Characterization of *In Vitro* Exposure Systems for the Remote Control of Nanomachines and Biological Processes by Electromagnetic Fields

MARIA LUCIA CALABRESE

Il Coordinatore del Corso   Il Tutore
Ch.mo Prof. Giovanni Poggi   Ch.ma Prof.ssa Rita Massa

Anno Accademico 2006-2007

This thesis is dedicated to the memory of
Prof. Guglielmo d'Ambrosio,
my tutor in the first year of my Ph.D.course

INDEX

Purpose of the research

The use of electromagnetic fields (EMFs) in medical applications dates back to the early decades of the twentieth century. Technological progress has led over the years to the development of various devices, however, linked to their use, and the rapid development of telecommunications, is related the problem of possible risks to human health. There are numerous studies in the literature aimed at identifying any biological effects induced by EMFs, which are based mainly on *in vitro* experiments. The results presented were not always indicative of the presence or absence of effect, being not reproducible and comparable, because of different involved parameters, but also, and very often, because of the limited accuracy of the characterization of the EMF exposure system. Therefore, in order to carried out a proper experimentation devoted to the study of possible interaction mechanisms between EMFs and biomolecules, both for medical applications and for evaluating possible effects induced by EMFs, it is necessary to have apparatuses that enable to perform exposures under controlled and reproducible conditions.

The main aim of the thesis is the design, realization and characterization of *in vitro* exposure systems in order to evaluate the interaction mechanisms between biological structures and EMFs, with particular reference to the possibility of using them for the remote control of nanomachines and biological processes.

In the first part of the thesis is presented the so-called "bioelectromagnetic context", referring to the studies reported in literature.

In the second part of the thesis is presented the methodology used for the design of exposure systems and some examples of applicators designed and actually used in various research programs for the evaluation of possible carcinogenic effects induced by EMFs at frequencies of the wireless communications systems (GSM, UMTS).

The third part of the thesis is devoted to the study of the remote control of nanomachines by EMC. Indeed, the opportunity to highlight any reversible effects induced by EMC on biostructures conjugated to nanocrystals (nanomachines) appeared particularly attractive, especially on the basis of the results recently presented in literature. One of the reported examples is the study of Hamad-Schifferli et al. (Nature, 2002), which evidentiated the possibility of interaction between the magnetic field and structures of DNA appropriately linked to gold nanocrystals. During EMF exposure (1 GHz) the opening and closing of the double helix of DNA, namely its denaturation and naturation, are optically observed. For a study of the mechanisms underlying this effect was therefore designed, realized and characterized an helical coil applicator in order to expose similar structures. After an analysis of the theoretical model, using numerical simulations the performances in terms of absorbed power per unit mass (SAR Specific Absorption Rate) and distribution of the field into the sample have been evaluated. The obtained numerical results were then compared with those observed experimentally. In addition, in order to highlight reversible effects induced by the radiation, the exposure system has been integrated with a fiber optic apparatus, to carry out spectrophotometric analysis contemporary to the exposures, and with a unit for temperature monitoring. The results of the experimentation, presented in this part of the thesis, suggest that the effect, we found, is probably due to bulk heating of solution; in addition these results induced to investigate on the applicability of other nanocrystals like magnetic nanopartices appropriately functionalized. It was therefore necessary to design a magnetic field applicator, which is the subject of the fourth part of the thesis. For this purpose a theoretical model of a double tape applicator has been developed: it enables to minimize electric field with respect to the magnetic field. The performances of the applicator, which included the sample and the thermostating system, were determined by numerical simulations in the frequency range 500 kHz - 10 MHz. The applicator has been realized, and a preliminary electromagnetic characterization has been carried out.

PART I

THE BIOELECTROMAGNETIC CONTEXT

Chapter 1

Open problems in bioelectromagnetic studies

The interaction mechanisms between electromagnetic fields (EMFs) and biological systems have been studying extensively for different purposes.

Rapid technological advances in electronics, electro-optics and computer science have set the stage for an unprecedented drive toward the improvement of existing medical devices and for the development of new ones. Frequencies, from low frequencies (LF) through microwave frequencies, are presently being investigated for therapeutic applications in areas such as cardiology, urology, surgery, ophthalmology, cancer therapy and others, and for diagnostic applications in cancer detection, organ imaging, and more.

At the same time, safety concerns regarding the biological effects of electromagnetic radiation have been raised, including those at a low-level of exposure. A variety of waves and signals have to be considered, from pure or almost pure sine waves to digital signals like in digital radio, digital television, and digital mobile phone systems. The field has become rather sophisticated, and the complexity of the problem requires an interdisciplinary effort for the convergence of different scientific disciplines towards a common research environment.

In this chapter the main concepts that are at the base of the interaction mechanisms between EMFs and biological systems will be described. In particular, several classification approaches that are commonly used in literature will be presented.

1.1   Basic Concepts

The evaluation of biological effects, including hazards, and of medical applications is related to situations where biological tissues and living systems are placed in specific electromagnetic environments. Generally antennas transmit the fields. They may be placed for instance in free space and have other purposes than illuminating human beings, like transmitting television, FM-radio or mobile telephony signals. They may also be placed in specific locations, within a part of a human body, for instance, to exert a specific medical effect. In this case, the antennas are often called *applicators*.

The reactive near field region is the region immediately surrounding the antenna, and where the reactive field predominates. For most antennas, this region is commonly taken as interior to a distance $0.62(D^3/\lambda)^{1/2}$ from the antenna surface, where λ is the wavelength and D the largest dimension of the antenna. The region is called reactive because the reactive power density predominates in this region. The radiating near field (Fresnel) region extends from the reactive near-field limit to a distance $2D^2/\lambda$ where D is the largest dimension of the antenna. For this expression to be valid, D must be large compared to the wavelength.

The far field (Fraunhofer) region is commonly taken to exist at distances greater than $2D^2/\lambda$ from the antenna. This criterion is based on a maximum phase error of $\lambda/8$. In this region the fields are essentially transverse and the angular distribution is independent of the radial distance where the measurements are made.

When evaluating biological effects, it is very important to clearly distinguish between near-field and far-field exposure.

The evaluation of hazards, due to RF/Microwave exposure on human beings or animals, is usually made in far-field conditions. Transmitting stations, indeed, are normally far enough from living and working situations on one hand, while the antenna of a mobile telephone is so small with respect to the wavelength that the head of an end-user is in the far field of the antenna. On the contrary, the evaluation of specific biological effects in medical applications is usually made in near-field conditions.

When the antenna is used to deliver microwave power to heat tissue, the size and location of the microwave field have to be carefully located to control the affected tissue. Hence, the type and shape of the antenna are very much depending upon the specific application, and there are a variety of applicators.

1.1.1 *Thermal* and *Non Thermal* Effects

The EMFs from the extremely low frequencies (ELF, 30 - 300 Hz) to radiofrequency and microwaves (100 kHz - 300 GHz) are usually known as the *Non-Ionizing Radiation* (NIR), characterized by a wavelength larger than 10^{-7} m and by a related energy smaller than 12 eV. Being the energy intensity not sufficient to induce molecules ionization phenomena or to broke chemical bonds even if very weak, until some decades these non-ionizing radiation have been considered enable to interact with the biological systems. Only more recently, with the development of the technology and, consequently, of the use of he EMFs at different frequencies and with different intensities, the scientific community has become to investigate to the possible biological effects induced by the EMFs.

A way to classify the biological effects of electromagnetic fields is based on the transfer of thermal energy from the incident radiation to the biological system. We can distinguish between *thermal* effects and *specific* or *non-thermal* effects.

The *thermal* effects are due to a sharp increase in temperature that can be systemic or localized; the produced heat quantity depends by the characteristics of the biological material, by the frequency and intensity of the field, by the exposure time and by the water content of the irradiated biological tissues.

The *specific* or *non-thermal* effects are due to phenomena in which temperature is just one of the parameters that play a role, not the dominant one.

The thermal effects induced by EMFs have been investigated from many researchers for a long time and results can now be believed as reliable. Mechanisms underlying the acute effects of exposure to high-level (both at low and high frequencies) are well assessed and on the basis of them the exposure safety levels have been defined [1].

It is to be noted that for many years it has been considered that the only effect induced by the EMFs was the increase of temperature in the exposed biological object; only in the last years the researchers involved in this sector have paved the possibility of specific interaction mechanisms due to low-levels electromagnetic exposure. Nowadays this type of interaction mechanisms is not completely established, due to the complexity of the systems involved (atomic or molecular lengths, physical quantities too weak to be detected, very unstable experimental samples).

1.2   Well Assessed Mechanisms Underlying the Biological Effects induced by EMFs

The evaluation of possible biological effects induced by EM exposure is usually carried out by following two different approaches that can be considered tightly bound each other: the *macroscopic* level, which deals with the entire biological system ant the *microscopic* level, which deals with the mechanisms at the lowest level (cellular and sub-cellular).

At the microscopic level the interaction take place by means of forces that the local electromagnetic field exerts on the electrical charges inside the biological structure. On the atomic scale it is necessary to distinguish between *unipolar* charges and *dipolar* charges. The first are essentially due to ions while the dipolar charges refer to water molecules, neutral proteins and the cell itself.

The electromagnetic forces and moment result in four different actions, which can be summarized as follows:

- Displacement of free charges (ions) from the equilibrium state;
- Vibrations of fixed charges (electrons bound to the atom, atom bound to molecules);
- Rotation and reorientation of dipolar molecules (water molecules and proteins);
- Displacement and rotation of cells.

At the macroscopic level there are three different basic coupling mechanisms through which time-varying electric and magnetic fields interact with living matter [1]:

- interaction with low-frequency electric fields;
- interaction with low-frequency magnetic fields;
- interaction at high frequency with electromagnetic field.

Exposure to time-varying EMF results in internal body currents and energy absorption in tissues that depend on the coupling mechanisms and the frequency involved. At low frequency the exposure to electric and magnetic fields implies negligible energy absorption and no measurable temperature increase in the body. However at higher frequencies exposure to electromagnetic fields can result in significant energy absorption and in temperature increases.

1.2.1 Low Frequency Electric Fields

The interaction with time-varying electric fields results in the flow of electric charges, in the polarization of bound charge and in the reorientation of electric dipoles already present in tissue. The relative magnitudes of these different effects depend on the electrical properties of the part of the body under test, that is, electrical conductivity and permittivity. Electrical conductivity and permittivity vary with the type of body tissue and also depend on the frequency of the applied field.
At low frequencies electric fields external to the body induce a surface charge on the body; this results in induced currents in the body, the distribution of which depends on the exposure conditions, on the size and shape of the body, and on the body's position respect to the incident field.

1.2.2 Low Frequency Magnetic Fields

The physical interaction of time-varying magnetic fields with the human body results in induced electric fields and circulating electric currents. The magnitudes of the induced field and the current density are proportional to the radius of the loop, the electrical conductivity of

the tissue, and the rate of change and magnitude of the magnetic flux density. For a given magnitude and frequency of magnetic field, the strongest electric fields are induced where the loop dimensions are greatest. The exact path and magnitude of the resulting current induced in any part of the body will depend on the electrical conductivity of the tissue.

Sine the body is not electrically homogeneous, the induced current densities can be calculated using anatomically and electrically realistic models of the body (*phantom*) with computational methods, which have a high degree of resolution.

1.2.3 High Frequency EMFs

At RF and microwaves, the electric and magnetic fields are simultaneously present: if there is an electric field, then there is a coupled magnetic field and *vice-versa*. If one is known, the other can be calculated: they are linked together by the well-known Maxwell's equations. It is interesting to be able to separate some biological effects due to one field from some due to the other field.

In living tissues, electromagnetic phenomena are usually slow, when compared to the extremely broad variety of phenomena to be evaluated. The shortest biological response time indeed is of the order of 10^{-4} second, while most of biological reactions are much slower. Hence, Maxwell's equations are most generally not used for evaluating biological effects in living tissues and systems: in practice, quasi-static approaches are quite satisfactory in biological material, and the electric and magnetic field are often considered separately, even at RF/Microwaves [2]. When the frequency increases, however, we need to account for the coupling effects between the two fields component.

In general, exposure to a uniform (plane-wave) electromagnetic field results in a highly non-uniform deposition and distribution of energy within the body, which must be assessed by *dosimetric* measurements and calculation.

As regards absorption of energy by the human body, electromagnetic fields can be divided into four ranges [1]:

- frequencies from about 100 kHz to less than about 20 MHz, at which absorption in the trunk decreases rapidly with

decreasing frequency, and significant absorption may occur in the neck and legs;
- frequencies in the range from about 20 MHz to 300 MHz, at which relatively high absorption can occur in the whole body, and to even higher values if partial body (e.g., head) resonances are considered;
- frequencies in the range from about 300 MHz to several GHz, at which significant local, non-uniform absorption occurs;
- frequencies above about 10 GHz, at which energy absorption occurs primarily at the body surface.

As it can be observed, most part of high frequency interaction is related to the energy absorption (per unit mass), the resulting distribution of energy can be described in terms of the *Specific Absorption Rate* (*SAR*), which is defined as the time derivative of the incremental energy (dW) absorbed by (dissipated in) an incremental mass (dm) contained in a volume element (dV) of a given density (ρ) [1]

$$SAR = \frac{d}{dt}\left(\frac{dW}{dm}\right) = \frac{d}{dt}\left(\frac{dW}{\rho dV}\right) \quad \text{W/kg}$$

The SAR is related to the internal -field by

$$SAR = \frac{\sigma |E|^2}{\rho} \quad \text{W/kg}$$

where σ is the effective conductivity of the tissue in siemens per meter, ρ is the mass density in kg/m and E is the rms electric field strength in volts per meter.

1.2.4 Dielectric properties of tissues

For a deeper comprehension about the interaction mechanisms between biological systems and EMFs at increasing frequencies, it can be useful to introduce the dielectric properties of tissues.
It is known that water is the major constituent in most tissues. The water contained in tissues is sometimes called *biological water*. It is obviously difficult to evaluate the differences between bulk tissue water and bulk water [3].
The complex permittivity is given by:

$$\varepsilon = \varepsilon_r \varepsilon_0 + j \frac{\sigma}{\omega}$$

where $\varepsilon_0 = 8.86 \times 10^{-12}$ f/m , and σ is the conductivity.

The relative dielectric constant (ε_r) and the conductivity of various tissues have been tabulated in popular references [4-5].

Following the model of H. P. Schwan [3]-[6-7], it is possible to consider the behaviour of permittivity for increasing frequencies:

- at ELF (until about 100 kHz) theory predicts a dielectric increment of the order of 10^6; ε shows a two-order decrease while the conductivity σ increases of a factor 2 or 3. This behaviour (*alpha-dispersion*) can be largely ascribed to the optimum dielectric properties of the membrane that at those frequencies blocks the induced currents flux across it. Although the alpha-dispersion is very striking in the permittivity, it does not appear in the conductivity. Assuming a dielectric increment of 10^6 and a relaxation frequency of 100 Hz, the Kramer and Kronig's relations yield a total increase in conductivity associated with the alpha-dispersion of about 0.005 Sm^{-1} while the ionic conductivity is about 200 times larger. Thus, at low frequencies, tissues are essentially resistive despite their tremendous permittivity values.

- The *beta-dispersion* occurs at radiofrequencies: as ε decreases σ increases. It arises principally from the capacitive charging of cellular membranes in tissues. A small contribution might also come from dipolar orientation of tissue proteins at high radiofrequencies. As an example, blood exhibits a total dielectric increment of 2000 and a beta relaxation frequency of 3 MHz [2]. The associated increase ion conductivity is about 0.4 Sm^{-1}. For tissues, the static permittivity and relaxation times of this dispersion are typically larger than in blood.

- The *gamma-dispersion* occurs with a centre frequency near 25 GHz at body temperature: σ continues to increase with a correspondent decrease of ε. It is due to the dipolar relaxation of the water that accounts for 80% of the volume of most soft tissues, yielding a total dielectric increment of 50. These values of dielectric increment and relaxation frequency yield a total increase in conductivity of about 70 Sm^{-1} [2].

- Some authors have called *delta-dispersion* a small dispersion occurring in tissues and other biological materials between 0.1 and 3 GHz. The lack of a single dominant mechanism makes the interpretation of this dispersion region difficult [7].

A good knowledge of the complex permittivity of biological media is necessary for evaluating biological effects as well as in medical applications. As examples the dielectric properties of some biological tissues will be discussed.

The low-frequency conductivity of *muscle tissues* has been reviewed in detail [8]. Muscle exhibits an extreme anisotropy in its configuration and hence in its electrical properties: there is a seven- to ten-fold variation in conductivity and permittivity (of dog skeletal muscle) at low frequencies. Similar variations have been reported in skeletal and heart muscle from many other species. For muscle tissue oriented perpendicular to the external field, the plateau between the alpha- and the beta-dispersion is at about 10^5 and the relaxation frequency is around 250 kHz. In the longitudinal orientation, the conductivity at low frequencies is higher and varies much less as a

function of frequency. At microwaves, there is not really a distinct separation between the beta- and higher-frequency dispersions.

There has been interest on other *soft tissues* with high water content, like liver or breast tissue, either normal or tumoral. The main non-water component of soft tissue is *protein*. At radiofrequencies, beta-dispersion is related to a broad distribution of relaxation times, which arises principally from the presence of membrane-bound structures of widely varying dimensions. A simple model for liver, assuming that the contributions to the permittivity from each major tissue structure are additive, yields remarkably good agreement with the measured properties of the tissue above 1 MHz [9]. One main result is that the dielectric dispersion in liver tissue in the range of 1 to 100 MHz represents the high-frequency end of the beta-dispersion of the cells together with the organelles.

Tumour tissues have often been found noticeably different from normal tissues, but not in all the experimental data [2].

They have significantly higher water content than normal tissues. Necrosis in the tumour leads to breakdown of cell membranes, so that a larger fraction of the tissue can carry current at low frequencies. Experimental data showed that necrosis yields a five- to ten-fold higher conductivity while the permittivity is generally smaller than that of normal tissue.

The infiltration in normal tissue of neoplastic tissues of high water content leads to pronounced changes in the dielectric properties, for instance in breast tissues. The practical significance of these differences however is unclear.

The dielectric properties of *bone* have also been investigated under near-normal physiological conditions. The conductivity of bone at low frequencies is associated with fluid-filled channels that permeate the tissue, and is proportional to the conductivity of the medium surrounding the tissue. The DC-conductivity varies by a factor of three with orientation. The corresponding variation of permittivity is largely unknown. Fluid-saturated bones exhibit a permittivity of about 1000 at audio frequencies, decreasing to 10-20 at 100 MHz. The conductivity increases by about 0.05 Sm^{-1} over the same frequency range.

Adipose tissues like fat and bone marrow are distinguished by their low water content and by cells largely filled with lipids. Fat and bone

marrow show a large alpha-dispersion between 104 and 105 Hz. The beta-dispersion is either absent or small in comparison with that of soft tissues. It has been observed that the conductivity of fat samples is higher than that of a soft tissue like liver, probably because of its larger extra-cellular fluid fraction [10].

Information about the influence of *temperature* on the electric parameters of the material may be needed for some applications. At low frequencies, below the beta-dispersion, the conductivity reflects the volume fraction of extra-cellular space. For small temperature increases, it has been reported that the conductivity properties of tumour and normal tissue, at 44 kHz and at 1 MHz, varied reversibly, with a temperature coefficient of about 2% per °C. These changes reflect thermally induced changes in the conductivity of tissue electrolyte. For large temperature increases (above about 44.5°C), however, the dielectric properties exhibit abrupt and irreversible changes, reflecting *thermal damage* to the tissue. In excised tissue maintained at 44°C, the low-frequency conductivity decreased initially by approximately 10% during the first hour, then gradually increased by approximately 50% during the next 8 hours; tenfold changes were reported in the permittivity over similar periods [2].

1.2.5 Penetration in biological tissue and skin effect

Biological materials are not good conductors. They do conduct a current, however, because the losses can be significant: they cannot be considered as lossless. Solving the diffusion equation, which is valid mainly for good conductors where the conduction current is large with respect to the displacement current, shows that the amplitude of the fields decays exponentially.

The penetration depth , i.e., the distance from the boundary of a medium to the point at which the field strengths or induced current densities have been reduced to $1/e$ of their initial boundary value in the medium, is given by (1) as follows for a plane-wave incident on a planar surface:

$$\delta = \frac{1}{\omega}\left[\left(\mu_0\varepsilon_r\varepsilon_0\right)\left(\sqrt{1+\left(\frac{\sigma}{\omega\varepsilon_r\varepsilon_0}\right)^2}\right)\right]^{-\frac{1}{2}} \quad \text{m} \qquad\qquad (1)$$

The parameter δ is called the *skin-depth (m).*
One main remark is that the skin-depth decreases when the frequency increases, being inversely proportional to the square root of frequency. It also decreases when the conductivity increases: the skin-depth is smaller in a good conductor that in another material.
Shielding is much easier to achieve at high frequencies than at low frequencies. Skin effect implies that the higher the frequency the smaller the penetration, which may lower the efficiency of a medical application. Hence, the choice of frequency is important. On the other hand, it also implies that if a human being, for instance, is submitted to a microwave field, its internal organs are more protected at higher than at lower frequencies. As an example, the skin-depth is 3 times smaller at 900 MHz, a mobile telephony frequency, than at 100 MHz, an FM-radio frequency, which means that the fields are 3 times more concentrated near the surface of the body at 900 MHz than at 100 MHz. It also means that internal organs of the body are submitted to higher fields at lower than at higher frequency.

1.3 Overview of the main results presented in literature

The world literature on microwave bioeffects is immense, with an estimated total of over 20000 papers. These can be classified as [11]:

- Experimental data on humans;
- Epidemiological;
- Experiments on animals-in vivo,
- In vitro experiments with biological tissue or cells, animal or human;

- • Dosimetry, the art and science of relating internal measures of exposure to external fields for a given animal.

1.3.1 Epidemiological Studies

The goal of much research into the biological consequences of exposure to EMFs is the understanding of how such exposure may compromise the normal biological functioning of human beings.

For a more comprehensive analysis it is useful to distinguish between low frequency and high frequency exposure biological effects.

Low Frequency

There have been many reviews of epidemiological studies of cancer risk in relation to exposure to power-frequency fields.

Research into the potential health effects of exposure to EMF has been underway for several decades. The catalyst for public awareness came from Wertheimer and Leeper (1979) who published an association between residences near certain types of power lines and increased incidence of childhood leukaemia and brain cancer. Data on cancer risk associated with exposure to ELF fields among individuals living close to power lines are apparently consistent in indicating a slightly higher risk of leukaemia among children, although more recent studies question the previously observed weak association [1].

Over the years there also has been substantial interest in whether there is an association between magnetic field exposure and childhood brain cancer, the second most frequent type of cancer found in children. Three studies [12-14] fail to provide support for an association between brain cancer and children's exposure to magnetic fields, whether the source was power lines or electric blankets, or whether magnetic fields were estimated by calculations or by wire codes.

A large number of epidemiological studies have been carried out to assess possible links between exposure to ELF fields and cancer risk among workers in electrical occupations. There have been reports of an increased risk of certain types of cancer, such as leukaemia, nervous tissue tumours, and, to a limited extent, breast cancer, among electrical workers. In most studies, job titles were used to classify subjects according to presumed levels of magnetic field exposure took advantage of a death certificate database that included both job titles and information on cancer mortality [15-16]. A few more recent

studies, however, have used more sophisticated methods of exposure assessment; overall, these studies suggested an increased risk of leukaemia or brain tumours but were largely inconsistent with regard to the type of cancer for which risk is increased. The data are insufficient to provide a basis for ELF field exposure guidelines. In a large number of epidemiological studies, no consistent evidence of adverse reproductive effects has been provided [1].

High Frequency

Data on human responses to high-frequency EMF that produce detectable heating have been obtained from controlled exposure of volunteers and from epidemiological studies on workers exposed to sources such as radar, medical diathermy equipment, and heat sealers [1]. Epidemiological studies on exposed workers and the general public have shown no major health effects associated with typical exposure environments. Although there are deficiencies in the epidemiological work, such as poor exposure assessment, the studies have yielded no convincing evidence that typical exposure levels lead to adverse reproductive outcomes or an increased cancer risk in exposed individuals. Epidemiological studies on exposed workers and the general public have provided limited information and failed to demonstrate any health effects. Reports of severe retinal damage have been challenged following unsuccessful attempts to replicate the findings.

Shocks and burns can be the adverse indirect effects of high-frequency EMF involving human contact with metallic objects in the field. At frequencies of 100 kHz – 110 MHz (the upper limit of the FM broadcast band), the threshold levels of contact current that produce effects ranging from perception to severe pain do not vary significantly as a function of the field frequency. The threshold for perception ranges from 25 to 40 mA in individuals of different sizes, and that for pain from approximately 30 to 55 mA; above 50 mA there may be severe burns at the site of tissue contact with a metallic conductor in the field.

Over 20 recent epidemiological studies of humans chronically exposed to assorted RF/MW sources (radar, mobile phones, etc.) have suffered from multiple technical deficiencies, especially an absence of exposure assessment and, thus, have had limited utility. Many of these studies targeted cancer as an endpoint and, at best, the findings were

equivocal or contradictory. In 2002, however, an european research program (INTERPHONE) has begun to investigate firstly on the assessment to the RF exposure from mobile telephones associated with cancer risk. A secondary objective of the studies was to investigate the relationship between these diseases and a number of potential environmental and endogenous risk factors. Participating countries are Australia, Canada, Denmark, Finland, France, Germany, Israel, Italy, Japan, New Zealand, Norway, Sweden and the UK. In order to maximise the power of finding a risk if it exists, the studies have been mainly focused on tumours in relatively young people (30-59 – who had the highest prevalence of mobile phone use 5 to 10 years ago) and on regions within the participating countries with longest and highest use of mobile phones. In order to exploit the information on occupational exposures collected within INTERPHONE study a work is currently undergoing [17].

The low quantum energy of RF/MW fields would not be expected to initiate or promote carcinogenesis, at least in terms of classical physical principles. In general, only a few frequencies have been studied, usually one at a time with limited field intensities. The worst case is believed to involve exposure at the resonant frequency, where the longest body dimension is and the RF/MW energy penetrates maximally [8].

The specific causes for the development of different types of human cancers are still poorly understood. However, several in vivo and in vitro investigations using mammalian cells have provided sufficient mechanistic information relevant to the assessment of whether an acute or chronic exposure to environmental (physical, chemical, and/or biological) agent has the potential to contribute to carcinogenesis.

1.3.2 *In vitro* and *in vivo* studies

Since many experimental manoeuvres cannot be performed on human subjects, studies of animal subjects must often be substituted. Most studies that report biological effects have involved acute (minutes to hours) RF/MW exposures of animal subjects or *in vitro* preparations.

The *in vitro* studies deals with all experimentations made in laboratory on isolated biological systems, such as tissues, cells and molecules, while *in vivo* studies refer to experiments done on the living tissue of a whole living organism. *In vitro* studies are relatively less expensive, are more rapid and less complicated than the *in vivo* studies; moreover they give the possibility of obtaining a lot of data in short times, providing a large base for statistical analysis. By means of this kind of studies it is possible to make targeted experimentations, in order to evaluate a possible effect induced by an electromagnetic field with fixed characteristics on a determinate biologic parameter, i.e. cellular proliferation, DNA duplication/repair. On the contrary, *in vitro* experimentation is characterized by the difficulty of choosing the biological system to be analyzed (cellular type, normal or tumoral cells); besides, the results are not always simple to interpret, to compare and to extrapolate to the whole individual, as they have obtained in the absence of the complexity of the whole organism.

Low Frequency
With the possible exception of mammary tumours, there is little evidence from laboratory studies that power-frequency magnetic fields have a tumour promoting effect. Although further animal studies are needed to clarify the possible effects of ELF fields on signals produced in cells and on endocrine regulation, both of which could influence the development of tumours by promoting the proliferation of initiated cells, it can only be concluded that there is currently no convincing evidence for carcinogenic effects of these fields and that these data cannot be used as a basis for developing exposure guidelines.

Laboratory studies on cellular and animal systems have found no established effects of low-frequency fields that are indicative of adverse health effects when induced current density is at or below 10 mA/m^2. At higher levels of induced current density (10–100 mA/m^2), more significant tissue effects have been consistently observed, such as functional changes in the nervous system and other tissue effects [18].

A recent excellent review of Vijayalaxmi and Guenter Obe [19] examine the studies, published in peer reviewed scientific journals during the years 1990– 2003, in which freshly collected and/or cultured mammalian somatic cells were exposed in vivo and in vitro

to extremely low frequency EMFs. The end points deal exclusively with genotoxic and epigenetic effect induced by EMFs.

The current understanding points to at least two pathways, which are not mutually exclusive, in the causation of cancer:

1) A ''genotoxic'' pathway where exposure to an environmental agent induces a single or a series of very specific damages to the genetic material (DNA) in a cell. Cells so damaged could undergo through death or go repair processes. Fidelity in the repair of damaged DNA has no subsequent adverse effects while the unrepaired and/or misrepaired damage will result in single (SSB) and double strand breaks (DSB) in the DNA leading to the formation of chromosomal aberrations (CA), micronuclei (MN), sister chromatid exchanges (SCE), and mutations; some of these lead to the development of cancer.

2) An ''epigenetic'' pathway where environmental agents, which may not cause genotoxicity or cancer by themselves, can contribute to carcinogenesis by increasing the genotoxic potential of other agents, interfering with the DNA repair processes, allowing a cell with DNA damage to survive and stimulating the cell division resulting in alteration in normal functions of the cell. The evidence for epigenetic action of an agent, especially for its relevance to human carcinogenicity under real life exposure conditions, must be evaluated carefully since very few environmental agents are documented to be epigenetic carcinogens.

The conclusions from 29 investigations (46%) did not identify increased cytogenetic damage following EMF exposure per se while those from 14 studies (22%) indicated a genotoxic potential of EMF exposure. The observations in 20 other reports (32%) were inconclusive. Among the 23 combination exposure investigations, the data from 10 studies did not identify epigenetic effects of EMF, while the data from one study indicated such an effect. The results from 12 other reports were inconclusive. Most of the reports that indicated an absence of genotoxic effect have described the EF, MF, and EMF exposure conditions and experimental protocols in detail so that the observations could be verified by independent researchers. The data are not in conflict with the other established characteristics of EMF. On the other hand, the interpretations presented for the presence of a genotoxic effect were not substantiated by experimental data.

Considering the ''weight of scientific evidence'' approach for genotoxicity investigations, as adopted by IARC [20], the preponderance of data thus far available in the literature shows that EMF exposure per se is not genotoxic (and little evidence for epigenetic influences) in mammalian cells. The collected informations indicates the variables existing in EMF exposure conditions and experimental protocols; further, direct comparisons of the data obtained in different investigations and by independent researchers seem to be almost impossible. The data from a well coordinated, multicenter collaborative study with adequate statistical power will be needed to identify the factors contributing to these controversial observations about the genotoxic potential of EMF.

High Frequency

Animal data indicate a threshold for behavioural responses in the same SAR range. Exposure to more intense fields, producing SAR values in excess of 4 W/kg, can overwhelm the thermoregulatory capacity of the body and produce harmful levels of tissue heating. Many laboratory studies with rodent and nonhuman primate models have demonstrated the broad range of tissue damage resulting from either partial-body or whole-body heating producing temperature rises in excess of 1–2°C. The sensitivity of various types of tissue to thermal damage varies widely, but the threshold for irreversible effects in even the most sensitive tissues is greater than 4 W/kg under normal environmental conditions. These data form the basis for an occupational exposure restriction of 0.4 W/kg, which provides a large margin of safety for other limiting conditions such as high ambient temperature, humidity, or level of physical activity.

Both laboratory data and the results of limited human studies [21] make it clear that thermally stressful environments and the use of drugs or alcohol can compromise the thermoregulatory capacity of the body. Under these conditions, safety factors should be introduced to provide adequate protection for exposed individuals.

Vijayalaxmi and Obe [22] review the investigations published in scientific journals during 1990–2003 to determine the genotoxic potential of exposure to radiofrequency (RF) radiation and attempts to identify probable reason(s) for the conflicting results. They stressed in particular the possibility of effects of exposure to RF radiation on genetic material (DNA).

Genotoxicity investigations in mammalian cells exposed to RF radiation increased in the 1980s. Among the 53 reports published during 1990–2003, the conclusions from 31 investigations (58%) did not identify increased cytogenetic damage after RF-radiation exposure, while those from 12 studies (23%) indicated a genotoxic potential of RF-radiation exposure. The observations in 10 other reports (19%) were inconclusive. Among the six combination exposure investigations, the data from three studies did not reveal epigenetic effects of RF radiation; the results from one report indicated an effect, while two other publications from the same researchers were inconclusive. The strength of most of the reports that did not indicate significantly increased genotoxicity after *in vivo* and *in vitro* exposure of mammalian somatic cells to RF radiation comes from the following: (a) the studies were experimentally sound with adequate temperature controls and validated dosimetry. (b) The investigations were conducted by independent researchers in independent laboratories. (c) There were ''replication'' investigations conducted under conditions duplicating the original study as well as ''confirmation'' studies in which conditions similar to those original investigations were used. (d) In general, the experimental protocols were described in detail so that the observations could be verified by independent researchers. (e) The data were not in conflict with the other established characteristics of RF radiation. (f) These studies also included larger sample sizes than the other studies. In contrast, the reports that suggested the genotoxic potential of RF radiation had confounding factors that were described and/or commented on by the investigators. The interpretation of some of the data was hypothetical and was not substantiated by experimental evidence. More importantly, the data were not confirmed by the same researchers in subsequent experiments. Also, multiple attempts by independent investigators did not confirm the observations. The importance of conducting cytogenetic investigations comes from the fact that most genotoxic agents are also carcinogens. Nongenotoxic agents (which may not cause cancer by themselves) can also contribute to the development of cancer by enhancing the damage induced by known genotoxic agents (i.e., they have an epigenetic effect). The absence of an increase in genotoxicity in mammalian somatic cells exposed to RF radiation, reported in the great majority of investigations, agrees with the large volume of published epidemiological and experimental

findings that do not support the concept that *in vivo* and *in vitro* exposure to RF radiation is carcinogenic. Also, the limited cytogenetic data from the combination exposure studies described above did not point to a clear epigenetic potential of RF radiation. The genotoxic (and epigenetic) potential of RF-radiation exposure should not be considered as ''established'' unless a significant increase in genotoxicity in cells exposed to RF radiation is (a) replicated by the same investigators (b) replicated and/or confirmed by independent investigators in independent laboratories and (c) such data are published in peer-reviewed journals. The preponderance of scientific evidence thus far available in the literature shows that RF-radiation exposure itself is not genotoxic in mammalian somatic cells.

1.4   Conclusions

In this chapter basic concepts of the interaction mechanisms between EMFs and biological systems have been described. The main classifications and the possible approaches in the evaluations of biological effects induced by EMFs are reported. In addition an overview of the main results of bioelectromagnetic studies are presented both for low and high frequencies. The reported results seem to be still not sufficient for give a definitive answer to the problem, though to date great efforts and great progress have been made. In the last years, however greater emphasis is addressed to the medical application of EMFs and in particular to the therapeutic effects induced by EMFs, as this seems to be the area with the greatest future potential [23].

References

[1] ICNIRP Guidelines, "Guidelines for Limiting Exposure to Time-varying Electric, Magnetic and Electromagnetic Fields", Health Physics, vol. 74, no, 4, pp. 494-522, 1998

[2] K.R. Foster, H.P. Schwan, Dielectric properties of tissues, in C. Polk, E. Postow (Eds.), Handbook of Biological Effects of Electromagnetic Fields. Boca Raton: CRC Press, 1996.

[3] A. Van der Wrost, Microwave Review, November 2005.

[4] H.P. Schwan, "Electrical Properties of Tissue and Cell Suspension", in "Advances in Biological and Medical Physics", eds: J. H. Lawrence and C. A. Tobias, Academic Press New York, 1957.

[5] H.P. Schwan, Electrical properties of cells: principles, some recent results and some unresolved problems, in W.S. Aldeman, and D. Goldman (Eds.), The Biophysical Approach to Excitable Systems. New York: Plenum Press, 1981.

[6] R.D. Stoy, K.R. Foster, H.P. Schwan, "Dielectric properties of tumor and normal tissues at radio through microwave frequencies," Phys. Med. Biol., vol. 27, p. 107, 1981.

[7] J.D. Kosterich, K.R. Foster, S.R. Pollack, "Dielectric permittivity and electrical conductivity of fluid saturated bone," IEEE Trans. Biomed. Eng., vol. 30, p. 81, 1983.

[8] E. R. Adair, R. Petersen, "Biological Effects of Radio-Frequency/Microwave Radiation", IEEE Trans. Microwave Theory and Technique, vol. 50, no. 3, March 2002, pp. 953 –962.

[9] J.D. Kosterich, K.R. Foster, S.R. Pollack, "Dielectric properties of fluid saturated bone: effect of variation in conductivity of immersion fluid," IEEE Trans. Biomed. Eng., vol. 31, p. 369, 1984

[10] S.R. Smith, K.R. Foster, "Dielectric properties of low-watercontent tissues," Phys. Med. Biol., vol. 30, p. 965, 1985.

[11] Osepchuk, J.M. Petersen, R.C., "Safety standards for exposure to RF electromagnetic fields", IEEE Microwave Magazine, vol. 2, no. 2, June 2001, pp. 57-69.

[12] P. Guénel, J. Nicolau, E. Imbernon, A. Chevalier, M. Goldberg, "Exposure to 50-Hz electric field and incidence of leukemia, brain tumors, and other cancers among French electric utility workers", Am. J. Epidemiol., vol. 144, pp. 1107–1121, 1996.

[13] Preston-Martin S., Navidi W., Thomas D., Lee P.J., Bowman J., Pogoda J., "Los Angeles study of residential magnetic fields and childhood brain tumors", Am. J. Epidemiol., vol. 143, pp. 105–119, 1996.

[14] Tynes T., Haldorsen T., "Electromagnetic fields and cancer in children residing near Norwegian high-voltage power lines", Am. J. Epidemiol., vol. 145, pp. 219 –226, 1997.

[15] Milham, S. Jr., "Mortality from leukemia in workers exposed to electrical and magnetic fields", New Engl. J. Med., vol. 307, p. 249, 1982.

[16] Savitz D. A., "Overview of epidemiological research on electric and magnetic fields and cancer", Am. Ind. Hyg. Ass. J., vol. 54, pp. 197–204, 1993.

[17] INTERPHONE Study, Results Update – 25 September 2007, online   available: www.iarc.fr/eng/units/interphoneresultsupdate.pdf.

[18] Tenforde T. S., "Interaction of ELF magnetic fields with living systems", in: Polk C., Postow E., eds. Biological effects of electromagnetic fields, Boca Raton, FL, CRC Press, pp. 185-230, 1996.

[19] Vijayalaxmi, Guenter Obe, "Controversial Cytogenetic Observations in Mammalian Somatic Cells Exposed to Extremely Low Frequency Electromagnetic Radiation: A Review and Future Research Recommendations", Bioelectromagnetics, vol. 26, pp. 412-430, 2005.

[20] IARC, "Non-ionizing radiation. Part I. Static and extremely low-frequency electric and magnetic fields", IARC Monogr. Eval. Carcinog. Risks Hum., vol. 80, pp. 1–395, 2002.

[21] Michaelson S. M., Elson E. C., "Modulated fields and 'window' effects", in: Polk C., Postow E., eds. Biological effects of electromagnetic fields, Boca Raton, FL, CRC Press, pp. 435–533, 1996.

[22] Vijayalaxmi, Guenter Obe, "Controversial Cytogenetic Observations in Mammalian Somatic Cells Exposed to Radiofrequency Radiation", Radiation Research, vol. 162, pp. 481-496, 2004.

[23] Jörg Reißenweber, "Medical, epidemiological and dosimetric aspects. A meeting report from a physician's perspective", BEMS Meeting Newsletter 3/2004, pp. 32-45

Chapter 2

The EMFs in Medical Application

For many years, medical and biological applications of EMF have been investigated. Hyperthermia and the related radiometry has been a major subject of interest in investigating biological effects of EMFs.

Hyperthermia was used to treat cancer patients as nearly as 1893 by increasing patient temperature through administering bacterial toxins, and EM diathermy was used to produce hyperthermia as early as the 1920's. More recently the use of EMF have been applied also to the diagnostics leading to the development of a non invasive method of medical imaging, like the magnetic resonance imaging (NMR). However this chapter is focused mainly to the therapeutic applications of EMFs, being the NMR a field of research by itself.

In addition the use of magnetic nanoparticles in biomedical applications and in particular for cancer therapy is presented, evidentiating the attractive research fields but also some critical aspects.

2.1 State of scientific knowledge

The early application of electricity to medicine named Galvanocautery, after Luigi Galvani, an 18th century obstetrician and surgeon in Bologna, for his work on chemical effects of electric current, involved dc currents applied directly to the tissue through needle, wire, or knife-type electrodes. The technique was reported to destroy tumours, aneurysms, and fungoid growths, as well as to close fistulas and to stop bleeding. It was actually the caustic effect of the electricity in coagulating blood, rather than to heating effect, to which these early physicians attributed the beneficial effects. Oscillatory sources soon became available through the work of Hehmholtz, Kelvin, and Hertz. Joubert, in the year 1889, demonstrated that when the frequency of current applied to frog muscle was raised to a certain level, it would not cause the muscle to contract. In the following year, d'Arsonval began research on measuring the electrophysiological activity in muscles and nerves, as well as the effect of low-frequency currents on muscles. In measuring the intensity of muscle excitation as a function of frequency, he noticed that the excitation decreased until it was barely noticeable at 10 kHz, the maximum attainable frequency of his source. He was able to apply the high-frequency current to himself at a high level without sensing anything but warmth. D'Arsonval was looking for physiologic rather than thermal effects. Though the immediate sensations of the currents passing through his hands from large electrodes were nil, he found that after a period of time the skin was flushed with increased sweating. He attributed this to vasodilatation rather than a heating reaction and wrote that the high-frequency currents would be a great service to therapeutics, thinking in terms of direct effects on blood pressure and kidney output, rather than the indirect effect of heat. Continuing his work with better equipment, he reported that there were no physiological effects at frequencies above 10 kHz. Up until 1893, all medical applications of high-frequency currents were made by direct electrical contact with the tissues or conduction. At that time, d'Arsonval introduced what he called autoconduction, which was really induction; at first, he experimentally placed animals (and then humans) in

induction coils. The human-size solenoidal coils were huge with big gaps between the turns. Autocondensation, the forerunner of diathermy, remained popular for many years, especially with many optimistic reports being made. During the period 1894-1895, d'Arsonval clinically treated seventy-five patients suffering various ailments with his machine. Each was exposed for 15–20 min daily in the induction coil for a total of 2500 treatments. He found that most types of hysteria and certain forms of local neuralgia received no benefit, while on the other hand there was marked improvement in the health of patients suffering from arthritic, rheumatic, and gouty conditions. By 1910, diathermy machines were beginning to make their appearance in supply houses.

Diathermy was soon used for many conditions including arthritis, poliomyelitis, pelvic diseases, and pneumonia. The frequency of the current used in long-wave diathermy up to 1929 was approximately 1 MHz, then many scientists began to investigate the short-wave diathermy and to use it for the cancer therapy [1].

H. J. Johnson, using more precise quantitative methods than those employed by other investigators, reported on the action of shortwaves on transplanted tumours in vivo and in vitro. He developed a technique for continuously measuring elevated temperatures in tumours during exposure, studying the thermal sensitivity of the Jensen-rat sarcoma and the Walker-rat Carcinoma-256 over a range of temperatures (43.5 –47°C). Johnson found that the exposure durations, required to produce a 50% regression of the Walker-rat Carcinoma-256 at 47, 45, and 43.5°C, were, respectively, 45 min, 1.5 h and 6 h. Exposure durations for 50% regressions of the Jensen-rat sarcoma at the same set of temperatures were 25 min, 1 h and 3 h. Johnson measured temperatures via thermocouples embedded in hypodermic needles; he tried to eliminate coupling of high-frequency currents by using a tuning process. Considerable problems were encountered with wave trapping by thermocouples under certain conditions, but he was able to obtain reliable temperature measurements [1]. The proposal to use microwaves for therapeutic purposes originated in Germany when Hollman [1] (in 1938–1939) discussed the possibility of therapeutic applications of 25 cm waves; he predicted that the waves could be focused to produce heating of the deep tissues without excessive heating of the skin. Similar predictions were made shortly afterward

by Hemingway and Stenstrom [1] in the United States. The lack of hardware during the late 1930's prevented development and clinical application of these concepts, and diathermy continued to be applied at frequencies below 100 MHz. After the development of magnetron and klystron tubes therapeutic applications of microwaves started. After 1950, and until 1965, research on the use of microwave diathermy in physical medicine expanded significantly.

Although the use of microwaves in therapeutic heating gained in popularity in the 1950's and early 1960's, interest in the use of shortwaves also continued. Birkner and Wachsmann [1] reported regressions and cures in skin carcinoma of patients exposed to shortwaves and X-rays in combination. Exposure of each of the 82 patients for a period of 2.5 h to 6-m shortwaves (tumour temperatures of 42–44°C) alone produced regressions but not cures. When shortwave exposures were combined with X-irradiation, however, some cures were observed. Fuchs [1] reported good clinical results when 6-m shortwave exposures of 10–20 min durations were followed by X-irradiation, He claimed that the good clinical results arose from increased radiosensitivity incident to hyperaemia and to acceleration of metabolism. In addition to the use of combined RF-field and X-ray therapy, interest developed in the use of microwaves in selective heating of tumours to provide more effective therapy in conjunction with injected radioactive materials and chemotherapy. Copeland and Michelson [1] reported that the heating of Walker carcinoma 256 by selective radiation (2800-MHz microwaves at 260 mW/cm^2 for 5 min) induced a substantial increase in the amount of intravenously injected I^{133} fibrinogen that was localized in the tumour. They pointed out that this tumour-heating technique could potentially increase tumour radiation therapy dose from I^{133} fibrinogen by 400 percent. Zimmer et al. [2] reported the use of selective electromagnetic heating in tumours of animals in deep hypothermia to enhance the action of chemotherapy. They treated spontaneous mammary tumours in C3H mice and induced mammary tumours in Sprague-Dawley rats, and found that in 20 control mice there were no spontaneous regressions of tumours and in 20 mice treated with chemotherapy only, two animals showed regression of tumours with a regression time of 10 days. Only one tumour in the group treated by differential hyperthermia, regressed after seven days. In the group of 20 mice treated both by differential hyperthermia and by chemotherapy in

combination, 17 animals exhibited regression of tumours after 55+25 days. Similar results were obtained from the rats, all 10 animals exposed to S-band fields (2.45 GHz) exhibited regression of tumours; the average regression time was 22 days.

From the mid-1970 on, interest in use of RF fields, either alone or in combination with radiation, increased substantially; a large number of favourable reports on the use of combined therapy have appeared in symposia proceedings and publications.

Some examples of more recent applications of submicrowave RF fields are in the reports of von Ardenne [3], Overgaard [4], Kim et al., [5], Storm et al. [6], and Gibbs [7]. Continuing success is reported in the use of microwave hyperthermia as an adjunct in the treatment of tumor. Szmigielski et al. [8] reported prolonged survival of mice bearing Sarcoma-180 tumours after irradiation by 3000-MHz microwaves such that rectal temperature increased by 3-4°C. The inhibitory effect of microwave hyperthermia was enhanced by simultaneous treatment of the mice with interferon and interferon inducers. Mendecki et al. [9] completely eradicated transplanted mammary adenocarcinoma in C3H mice and, in several clinical cases, obtained favourable results in the treatment of basal-cell carcinoma, malignant melanoma, and skin metastasis of carcinoma of the breast by both 2450-MHz and 915-MHz fields. In these studies, the temperature of the tumours was raised to a temperature between 42.5 and 43°C. Interstitial application of low-frequency energy (500-lkHz) has also been successfully used in the treatment of tumours [10].

Nowadays the use of thermo ablation of cancer cells is particularly related to the use of magnetic particles. This argument will be presented in a following paragraph.

The use of electromagnetic field is also applied to medical imaging; a very benefits in diagnostics are due to the magnetic resonance imaging (NMR), a powerful non invasive method.

Felix Bloch and Edward Purcell discovered the magnetic resonance phenomenon independently in 1946. In the period between 1950 and 1970, NMR was developed and used for chemical and physical molecular analysis. In 1971 Raymond Damadian [11] showed that the nuclear magnetic relaxation times of tissues and tumours differed, thus motivating scientists to consider magnetic resonance for the detection of disease. In 1973 the x-ray-based computerized tomography (CT)

was introduced by Hounsfield [12].Magnetic resonance imaging was first demonstrated on small test tube samples that same year by Paul Lauterbur [13]. He used a back projection technique similar to that used in CT. In 1975 Richard Ernst [14] proposed magnetic resonance imaging using phase and frequency encoding, and the Fourier Transform. This technique is the basis of current MRI techniques. A few years later, in 1977, Peter Mansfield developed the echo-planar imaging (EPI) technique [15]. This technique will be developed in later years to produce images at video rates (30 ms / image). Edelstein and coworkers demonstrated imaging of the body using Ernst's technique in 1980. A single image could be acquired in approximately five minutes by this technique. By 1986, the imaging time was reduced to about five seconds, without sacrificing too much image quality. The same year people were developing the NMR microscope, which allowed approximately 10 μm resolution on approximately one cm samples. In 1987 echo-planar imaging was used to perform real-time movie imaging of a single cardiac cycle [16]. In this same year Charles Dumoulin was perfecting magnetic resonance angiography (MRA), which allowed imaging of flowing blood without the use of contrast agents [17]. In 1992 functional MRI (fMRI) was developed. This technique allows the mapping of the function of the various regions of the human brain. Five years earlier many clinicians thought echo-planar imaging's primary applications were to be in real-time cardiac imaging. The development of fMRI opened up a new application for EPI in mapping the regions of the brain responsible for thought and motor control [18-19]. In 1994, researchers at the State University of New York at Stony Brook and Princeton University demonstrated the imaging of hyperpolarized 129Xe gas for respiration studies [20]. MRI is clearly a young, but growing science.

2.2 Electromagnetic fields applicators for medical application

Medical and biological EM applications may be classified into two broad groups [21]: 1) therapeutic, and 2) informational (including diagnostics and measurement of material EM properties). Examples of therapeutic applications include diathermy, hyperthermia for cancer therapy, rewarming of hypothermic patients, enhancement of bone and

wound healing, nerve stimulation and neural prosthesis, microwave angioplasty, treatment of benign prostatic hyperplasia, and cardiac ablation. Some examples of informational applications are imaging (including electrical impedance, microwave, and nuclear magnetic resonance imaging), measurement of lung water content, tumour detection, and personnel dosimetry. Studies of how EM fields interact with biological systems (EM bioeffects) are other examples of informational applications and the corresponding applicators will be treated in the second part of the thesis. In this section the attention will be focused mainly on therapeutics applicators and in particular to applicators for hyperthermia, being magnetic resonance imaging a field of research by itself.

The potential of hyperthermia as a treatment for cancer was first predicted following observations that several types of cancer cells were more sensitive to temperatures in excess of 41°C than their normal counterparts [22-23]. In the past external means of heat delivery were used such as RF or microwave treatments; to this end different applicators have been developed. In the following an overview of the main EMF applicators used for cancer therapy is presented.

2.2.1   Noninvasive Applicators

Noninvasive (not penetrating the body) applicators may be classified as belonging to three main groups: 1) E-type (low-frequency) applicators, which produce mainly an E field that heats the tissue, 2) H-type (low-frequency) applicators, which produce mainly a magnetic field, which in turn induces the E field that heats the tissue, and 3) radiative applicators.

a) *E-type applicators:* Capacitor-plate applicators are typical E-type applicators. These applicators are usually operated at either 13.56 MHz or 27.12 MHz, two of the frequencies assigned to industrial, scientific, and medical use (ISM frequencies). Capacitive applicators heat deep tissue well, but they usually produce large components of E field normal to the fat muscle interface, which overheat the fat because boundary conditions require the normal E fields at the interface to be discontinuous by the ratio of the permittivities, and since fat has a lower permittivity than muscle, the E field in the fat is higher [24]. Injurious heating of surface tissues has been reduced with

cooled-contact electrodes, and intratumor temperatures to 57°C at 10 cm depth have occurred in selected individuals who had minimal overlaying fatty tissues [25]. With multiplate capacitor configurations [26], internal heating patterns can be adjusted by changing the relative voltages applied to the various plates. Ring capacitors can produce deep internal heating without overheating the surface if a proper gap is maintained between the rings and the body surface.

b) *H-type applicators*: Perhaps the simplest H-type applicator is a single coaxial current loop. A device called the magnetrode consists of a single sheet coaxial current loop [27]. Since the coaxial current loop produces eddy current type E fields that circulate around the axis of the loop, heating in the center of the body is minimal. Generally speaking, H-type applicators seem not to couple as strongly to the body as E-type applicators, and relatively high currents are usually needed to get adequate heating. H-type applicators have the advantage that they produce an E field mostly tangential to the fat, which therefore does not overheat the fat. Since most of them are designed to operate at ISM frequencies of 13.56, 27.12, or 40 MHz, the depth of penetration is typically a few centimetres.

The helical-coil applicator is like an H-type applicator in some respects, but its heating characteristics seem to be more like an E-type applicator, since the strong *E* field produced between the turns of the oil is mainly responsible for tissue heating. [28]. A surface semi cylindrical helical coil heats well internally, but tends to overheat the surface [29-30]. This aspect will be analyzed in more details in the chapter 5.

c) *Radiative applicators*: Various kinds of open-ended waveguide applicators, some loaded with dielectrics to provide better impedance matching and coupling to the body, have been studied over the years. These single waveguide applicators generally produce penetration less than the theoretical plane-wave penetration. Phased arrays at lower frequencies can provide better penetration, but not a small spot size because the wavelength is too long. An annular phased array (APA) consisting of two side-by-side arrays of eight dielectrically loaded apertures operating at frequencies from 55 to 110 MHz is used extensively to provide a deep regional heating pattern that can be adjusted to some extent by phasing the radiators. Operation in this frequency range provides deep penetration, but not a small focused spot.

2.2.2 Invasive Applicators

Invasive applicators can produce more uniform and controllable heating patterns than noninvasive applicators, but they require some kind of implantation in the tissue, this is not feasible for all tumours. Electrical invasive applicators are of three basic types: 1) arrays of needles that produce RF localized current fields (LCF), 2) radiating microwave antennas, and 3) inductively heated ferromagnetic seeds. In the RF LCF systems, RF currents produced by voltage sources connected between needle pairs, or between one set of needles and another set, produce ohmic heating. The heating pattern is affected by tissue inhomogeneities, since the current will tend to follow the paths of least resistance. Parallelism of the needles also affects uniformity of the pattern. Since current density concentrates near needle surfaces, the heating is strongest there, decreasing as the current spreads out between the needles. Heating patterns are adjusted by switching sources repeatedly between alternate pairs of needles and by dielectric coatings on a portion of each needle. Implanted radiating microwave antennas, either singly, or in arrays, both phased and nonphased, have been used extensively for heating certain kinds of tumours. Where it is feasible to implant antennas, well controlled heating patterns can be achieved. Implanted microwave antennas heat both through ohmic and dielectric losses. A typical implanted antenna consists of coaxial cable with the center conductor extended. Variations include steps in the diameter of the extended center conductor, various dielectric coatings on the center conductor, and helical coils wound around the center conductor. In the third method, ferromagnetic segments (or seeds) are implanted and then heated by an externally applied low-frequency (less than 500 kHz) magnetic field. The overall heating pattern is a function of the size, shape, and ferromagnetic properties of the seeds. Advantages are that no connections between the source and the seeds is required, and the size, shape, and properties of the seed can be chosen to optimize the heating pattern, but a strong magnetic field is required to produce the heating.

2.2.3 Other Therapeutic Applications [31]

Antennas and other EM applicators similar to those used for hyperthermia, particularly capacitive and inductive applicators, have been used for diathermy. EM applicators can produce deeper heating than methods that simply heat the body surface and rely on thermal conduction to carry the heat to the deeper tissues. Similar applicators have also been used to rewarm hypothermic patients. If peripheral tissues are warmed while the heart is still cold, as happens with conventional rewarming, the warmed peripheral tissues demand increased circulation that overloads the still cold heart. A better method is to rewarm the heart first by EM techniques, which increases cardiac output and circulates warmed blood to the peripheral tissues without overloading the heart.

2.3 Use of magnetic nanoparticles for cancer therapy

Magnetic nanoparticles offer some attractive possibilities in biomedicine [32]. First, they have controllable sizes ranging from a few nanometres up to tens of nanometres, which places them at dimensions that are smaller than or comparable to those of a cell (10–100μm), a virus (20–450 nm), a protein (5–50 nm) or a gene (2 nm wide and 10–100 nm long). Indeed, they can be coated with biological molecules to make them interact with or bind to a biological entity, thereby providing a controllable means of 'tagging' or addressing it. The nanoparticles are magnetic and can be manipulated by an external magnetic field gradient. This "action at a distance", combined with the intrinsic penetrability of magnetic fields into human tissue, opens up many applications. In this way they can be made to deliver a package, such as an anticancer drug, or a cohort of radionuclide atoms, to a targeted region of the body, such as a tumour. Third, the magnetic nanoparticles can be made to resonantly respond to a time-varying magnetic field, with advantageous results related to the transfer of energy from the exciting field to the nanoparticle. In particular the particle can be made to heat up, which leads to their use as hyperthermia agents, delivering toxic amounts of thermal energy to

targeted bodies such as tumours; or as chemotherapy and radiotherapy enhancement agents, where a moderate degree of tissue warming results in more effective malignant cell destruction.

2.3.1 Drug delivery with NMP

The major disadvantage of most chemotherapies is that they are relatively non-specific. The therapeutic drugs are administered intravenously leading to general systemic distribution, resulting in deleterious side-effects as the drug attacks normal, healthy cells in addition to the target tumour cells. For example, the side effects of anti-inflammatory drugs on patients who have chronic arthritis can lead to the discontinuation of their use. However, if such treatments could be localized, e.g. to the site of a joint, then the continued use of these very potent and effective agents could be made possible.

In the past some researchers proposed the use of magnetic carriers to target specific sites (generally tomoural sites) within the body [32]. This kind of research has two main purposes:

1) to reduce the amount of systemic distribution of the cytotoxic drug, thus reducing the associated side-effects;
2) to reduce the dosage required by more efficient, localized targeting of the drug.

In magnetically targeted therapy, a cytotoxic drug is attached to a biocompatible magnetic nanoparticle carrier. These drug/carrier complexes, usually in the form of a biocompatible ferrofluid, are injected into the patient via the circulatory system. When the particles have entered the bloodstream, external, high-gradient magnetic fields are used to concentrate the complex at a specific target site within the body. Once the drug/carrier is concentrated at the target, the drug can be released either via enzymatic activity or changes in physiological conditions such as pH, osmolality, or temperature [32], and be taken up by the tumour cells. This system, in theory, has major advantages over the normal, non-targeted methods of cytotoxic drug therapy.

The development of techniques that could selectively deliver drug molecules to the diseased site, without a concurrent increase in its level in healthy tissues, is currently one of the most active areas of cancer research. The first clinical trials in humans with a magnetic drug targeting worldwide were reported by Lübbe et al. [33], who

used a ferrofluid (particle size 100 nm) to which the drug epirubicin was chemically bound. Epirubicin is a well-known antibiotic antracylin that has a wide range of application for the treatment of solid tumours.

To understand this new form of pharmacological application as well as the mechanism of action, there are many considerations, which may be subdivided into several categories. In the first instance there is the ferrofluid's parameters, which include particle size, surface characteristics, concentration, volume and strength of drug–particle binding. Secondly there is access to the organism, where considerations involve the infusion route, such as the duration and rate of the injection. Finally there are the physiological parameters to consider, ranging from the organism's weight, blood volume, cardiac output, circulation time through to tumour volume/location/blood flow.

A recent attractive field of research involves the use of magnetic nanoparticles for the remote control of biological nanomachines by means of EMF. The magnetic nanoparticles, infact, can be conjugated to proteins able to selectively target them and to put localized in that specific site. This type of drug delivery could be achieved using nanomachines as transport vehicles; these nanomachines for chemical-biological properties bind themselfes to the target cells, then by means of a control signal (the electromagnetic field) deliver the drug.

2.3.2 Hyperthermia

The preferential killing of cancer cells without damaging normal cells has been a desired goal in cancer therapy for many years.

Since finite applicators typically produce less penetration than plane waves, heating a deep lying tumor at RF frequencies would overheat the surface, and operation at lower frequencies therefore seems desirable. At low frequencies, though, the wavelength is so long that the energy cannot be localized to a small region, and only large regional heating can be obtained. Worse than that, at low frequencies, the applicator will be electrically small if its physical size is manageable, and near fields will dominate. Since near fields decay rapidly with distance away from the applicator, dominant nearfields

often overheat the surface. Consequently, practical heating of internal body tumours without overheating the surface is very difficult at any frequency.

More recently research has focused on the injection of magnetic fluids directly into the tumour body, or into an artery supplying the tumour.

The method relies on the theory that any metallic objects when placed in an alternating magnetic field will have induced currents flowing within them. The amount of current is proportional to the size of the magnetic field and the size of the object. As these currents flow within the metal, the metal resists the flow of current and thereby heats, a process termed inductive heating. If the metal is magnetic, such as iron, the phenomenon is greatly enhanced. Therefore, when a magnetic fluid is exposed to an alternating magnetic field the particles become powerful heat sources, destroying the tumour cells.

Experimental investigations of the application of magnetic materials for hyperthermia date back to 1957 when Gilchrist *et al* [32] heated various tissue samples with 20–100 nm size particles of γ-Fe$_2$O$_3$ exposed to a 1.2 MHz magnetic field. Since then there have been numerous publications describing a variety of schemes using different types of magnetic materials, different field strengths and frequencies and different methods of encapsulation and delivery of the particles [32]. In broad terms, the procedure involves dispersing magnetic particles throughout the target tissue, and then applying an AC magnetic field of sufficient strength and frequency to cause the particles to heat. This heat conducts into the immediately surrounding diseased tissue whereby, if the temperature can be maintained above the therapeutic threshold of 42°C for 30 min or more, the cancer is destroyed. Whereas the majority of hyperthermia devices are restricted in their utility because of unacceptable coincidental heating of healthy tissue, magnetic particle hyperthermia is appealing because it offers a way to ensure only the intended target tissue is heated.

There are now two different approaches. The first is called magnetic hyperthermia and involves the generation of temperatures up to 45–47°C by the particles. This treatment is currently adopted in conjunction with chemotherapy or radiotherapy, as it also renders the cells more sensitive [34]. The second technique is called magnetic thermoblation, and uses temperatures of 43–55°C that have strong cytotoxic effects on both tumour and normal cells [35]. A number of

studies have demonstrated the therapeutic efficacy of this form of treatment in animal models [36]. To date, however, there have been no reports of the successful application of this technology to the treatment of a human patient. The challenge lies in being able to deliver an adequate quantity of the magnetic particles to generate enough heat in the target using AC magnetic field conditions that are clinically acceptable. Most of the laboratory and animal model based studies reported so far are characterized by the use of magnetic field conditions that could not be safely used with a human patient. In most instances, reducing the field strength or frequency to safer levels would almost certainly lead to such a reduction in the heat output from the magnetic material as to render it useless in this application.

The frequency and strength of the externally applied AC magnetic field used to generate the heating is limited by deleterious physiological responses to high frequency magnetic fields [32]. These include stimulation of peripheral and skeletal muscles, possible cardiac stimulation and arrhythmia, and non-specific inductive heating of tissue. Generally, the useable range of frequencies and amplitudes is considered to be $f = 0.05$–1.2 MHz and $H = 0$–15 kAm^{-1}. Experimental data on exposure to much higher frequency fields comes from groups such as Oleson et al. [32] who developed a hyperthermia system based on inductive heating of tissue, and Atkinson et al. [37] who developed a treatment system based on eddy current heating of implantable metal thermoseeds. Atkinson et al. concluded that exposure to fields where the product $H \cdot f$ does not exceed 4.85×10^8 Am^{-1} s^{-1} is safe and tolerable.

The amount of magnetic material required to produce the required temperatures depends to a large extent on the method of administration. For example, direct injection allows for substantially greater quantities of material to be localized in a tumour than do methods employing intravascular administration or antibody targeting, although the latter two may have other advantages. A reasonable assumption is that ca 5–10 mg of magnetic material concentrated in each cm^3 of tumour tissue is appropriate for magnetic hyperthermia in human patients. Regarding the choice of magnetic particle, the iron oxides magnetite (Fe_3O_4) and maghemite (γ-Fe_2O_3) are the most studied to date because of their generally appropriate magnetic properties and biological compatibility, although many others have been investigated. Particle sizes less than about 10μm are normally

considered small enough to enable effective delivery to the site of the cancer, either via encapsulation in a larger moiety or suspension in some sort of carrier fluid. Candidate materials are divided into two main classes; ferromagnetic or ferrimagnetic (FM) single domain or multi-domain particles, or superparamagnetic (SPM) particles; each of them has different heating generating mechanisms. There exist at least three different mechanisms by which magnetic materials can genertate heat in an alternating field:

- Generation of eddy currents in bulk magnetic materials;
- Hysteresis losses in bulk and multi-domain magnetic materials;
- Relaxation losses in SPM single-domain magnetic materials.

It is very important to be noted that for the different loss processes the specific loss power (SLP) strongly depends by structural (dimension) and magnetic properties on one hand, and amplitude and frequency of the external alternating magnetic field on the other hand.

FM particles possess hysteretic properties when exposed to a time varying magnetic field, which gives rise to magnetically induced heating. The amount of heat generated per unit volume is given by the frequency multiplied by the area of the hysteresis loop:

$$P_{FM} = \mu_0 f \oint \underline{H} d\underline{M} \qquad (1)$$

where H is the magnetic field and M is the magnetization, defined as the magnetic moment per unit volume.

This formula ignores other possible mechanisms for magnetically induced heating such as eddy current heating and ferromagnetic resonance, but these are generally irrelevant in the present context. The particles used for magnetic hyperthermia are much too small and the AC field frequencies much too low for the generation of any substantial eddy currents. Ferromagnetic resonance effects may become relevant but only at frequencies far in excess of those generally considered appropriate for this type of hyperthermia.

Over the last decade the field of magnetic particle hyperthermia has been revitalized by the advent of "magnetic fluid hyperthermia", where the magnetic entities are SPM nanoparticles suspended in water or a hydrocarbon fluid to make a "magnetic fluid" or "ferrofluid" [32]. When a ferrofluid is removed from a magnetic field its magnetization relaxes back to zero due to the ambient thermal energy of its environment. This relaxation can correspond either to the physical

rotation of the particles themselves within the fluid, or rotation of the atomic magnetic moments within each particle. Rotation of the particles is referred to as "Brownian rotation" while rotation of the moment within each particle is known as "Néel relaxation". Each of these processes is characterized by a relaxation time τ: τ_B for the Brownian process depends on the hydrodynamic properties of the fluid; while τ_N for the Néel process is determined by the magnetic anisotropy energy of the SPM particles relative to the thermal energy. Both Brownian and Néel processes may be present in a ferrofluid, whereas only τ_N is relevant in fixed SPM particles where no physical rotation of the particle is possible. The relaxation times τ_B and τ_N depend differently on particle size; losses due to Brownian rotation are generally maximized at a lower frequency than those are due to Néel relaxation for a given size.

The physical basis of the heating of SPM particles by AC magnetic fields has been reviewed by Rosensweig [38]. It is based on the Debye model, which was originally developed to describe the dielectric dispersion in polar fluids, and the recognition that the finite rate of change of M in a ferrofluid means that it will lag behind H. For small field amplitudes, and assuming minimal interactions between the constituent SPM particles, the response of the magnetization of a ferrofluid to an AC field can be described in terms of its complex susceptibility $\chi = \chi' + i\chi''$, where both χ' and χ'' are frequency dependent. The out-of-phase χ'' component is related to the volumetric power dissipation by the following expression:

$$P_{SPM} = \mu_0 \pi f \chi'' H^2 \qquad (2)$$

which can be interpreted physically as meaning that if M lags H there is a positive conversion of magnetic energy into internal energy.

This simple theory compares favourably with experimental results, for example, in predicting a square dependence of P_{SPM} on H, and the dependence of χ'' on the driving frequency [32].

Measurements of the heat generation from magnetic particles are usually quoted in terms of the specific absorption rate (SAR) in units of Wg^{-1}. Multiplying the SAR by the density of the particle yields P_{FM} and P_{SPM}, so the parameter allows comparison of the efficacies of magnetic particles covering all the size ranges [32]. It is clear from such comparisons that most real FM materials require applied field strengths of ca 100 kAm^{-1} or more before they approach a fully

saturated loop, and therefore only minor hysteresis loops can be utilized given the operational constraint of ca 15 kAm^{-1}, giving rise to low SARs. In contrast, SPM materials are capable of generating impressive levels of heating at lower fields. For example, the best of the ferrofluids reported by Hergt et al. [39] has a SAR of 45Wg^{-1} at 6.5 kAm^{-1} and 300 kHz which extrapolates to 209Wg^{-1} for 14 kAm^{-1}, compared to 75Wg^{-1} at 14 kAm^{-1} for the best FM magnetite sample.

This field of research has been largely investigated in the last five years, however in most investigations on magnetic particle hyperthermia seems that particles are chosen according to easy availability instead of maximum SLP. In a recent interesting study of R. Hergt and S. Dutz [40] an excellent analysis of magnetic particle hyperthermia is carried out with respect to SLP of magnetic nanoparticles under the condition of a limitation of the alternating magnetic field amplitude and frequency. Infact, though the specific loss power is an increasing function of frequency f and field amplitude H in a wide parameter range the opportunities for enhancement of SLP by an increase of f and H are limited for technical and biomedical reasons. From a technical point of view for increasing frequencies it is not simple to realize large magnetic field amplitudes in a volume needed for exposure of a human torso. Even more importantly a strict limitation $Hxf < 4.85\text{x}10^{8}$ Am^{-1} results for biomedical reasons; as already said, the alternating magnetic field causes also un unwanted non selective heating of both cancerous and healty tissues due to the generation of eddy currents.

2.4 Conclusions

In this chapter the main medical applications of EMF have been presented. In addition an overview of EM applicators generally used for therapeutical purposes is reported. Recently many researchers have been to investigate on the use of magnetic nanoparticles both for targeted drug delivery and the selective thermoablation of cancer cells by hyperthermia. Even if this line of research seems to be very interesting and attractive recent studies presented in literature evidentiated some critical aspect:

- The SLP is strictly depended on the size and concentration of the magnetic nanoparticles in the tissue volume.
- It is necessary to transfer a higher amount of energy in the tumoral tissue than the surrounding healthy tissue.
- It is necessary to verify that the magnetic nanoparticles can absorb energy enough from the applied magnetic field to activate the targeted biomolecule.

For this reason it is indispensable to carry out studies that involve on one hand a full investigation on the magnetic nanoparticles to be applied, and on the other hand the development of an electromagnetic field exposure apparatus opportunely designed for this type of research. A full comprehension of the interaction mechanisms between the exposed samples and the electromagnetic fields is possible only if there is a precise description of the EMF applicator and an accurate control of dosimetry.

References

[1] A. W. Guy, "Hystory of Biological Effects and Medical Applications of Microwave Energy", IEEE Trans. Microwave Theory and Technique, vol. 32, no. 9, pp. 1182-1200, 1984.

[2] R. P. Zimmer, H. A. Ecker, V. P. Popovic, "Selective electromagnetic heating of tumors in animals in deep hypothermia," IEEE Trans. Microwave Theory Tech., vol. 19, pp. 232-238, 1971.

[3] M. von Ardenne, "On a new physical principle for selective local hyperthermia of tumor tissues," in Cancer Therapy by Hyperthermia and Radiation, C. Streffer et al., Eds. Munich: Urban & Schwarzenberg,, pp. 96-104, 1978.

[4] J. Overgaard, "Biological effect of 27.12 MHz shortwave diathermic heating in experimental tumors," IEEE Trans. Mtcrowave Theory Tech., vol. 26, pp. 523–529, 1978.

[5] J. H. Kim, P. Antich, S. Ahmed, E. W. Hahn, "Clinical experience with radiofrequency hyperthermia," J. Microwave Power, vol. 16, no.2, pp. 193-197, 1981.

[6] F. K. Storm, W. Harrison, R. S. Elliot, L. R. Kaiser, A. W. Silberman, D. L. Morton, "Clinical radiofrequency hyperthermia by magnetic-loop induction," J. Microwave Power, vol. 16, no. 2, pp. 79-183, 1981.

[7] F. A. Gibbs, "Clinical evaluation of a microwave RF system (BSD Corporation) for induction of local and regional hyperthermia" J. Microwave Power, vol. 16, no. 2, pp. 185-191, 1981.

[8] S. Szmigielski, M. Bielec, M. Janiak, M. Kobus, M. Lcuzak, and E. DeClercq, "Inhibition of tumor growth in mice by microwave hyperthermia, polyriboinosinic-polyribocytidylic, and mouse interferon: IEEE Trans. Microwave Theory Tech., vol. 26, pp. 520-522, 1978.

[9] J. Mendecki, E. Friedenthal, C. L. Botstein, F. Sterzer, R. Paglione, M. Nowogrodski, and E. Beck, "Microwave-induced hypertherrnia in cancer treatment: apparatus and preliminary

results," Int. J. Radiation Oncology Biol. Phys., vol. 4, pp. 1095-1103, 1978.

[10] W. G. Connor, "Localized current field heating as an adjunct to radiation therapy", Radiation and Environmental Biophysics, vol. 17, no. 3, pp. 219-228, 1980.

[11] R.V. Damadian, "Tumor Detection by Nuclear Magnetic Resonance", Science, vol. 171, p. 1151, 1971.

[12] G.N. Hounsfield, Br. J. Radiol., vol. 46, pp. 1016-1022, 1973.

[13] P.C. Lauterbur, "Image formation by induced local interactions: examples employing nuclear magnetic resonance", Nature vol. 242, pp. 190-191, 1973.

[14] A. Kumar, D. Welti, R.R. Ernst, "NMR Fourier zeugmatography", J. Magn. Reson., vol. 18, pp. 69-83, 1975.

[15] P Mansfield, "Multi-planar image formation using NMR spin-echos", J. Phys. C: Solid State Physics, vol. 10, pp. L55-L58, 1977.

[16] A. Chapman, R. Turner, R.J. Ordidge, M. Doyle, M. Cawley, R. Coxon, P. Glover, P. Mansfield, "Real-Time Movie Imaging from a Single Cardiac Cycle by NMR", Magn. Reson. Med., vol. 5, pp. 246-254, 1987.

[17] A. C.L. Dumoulin, S.P. Souza, H.R. Hart, "Rapid Scan Magnetic Resonance Angiography", Magn. Reson. Med., vol. 5, pp. 238-245, 1987.

[18] K.K Kwong, J.W. Belliveau, D.A. Chesler, I.E. Goldberg, R.M. Weisskoff, B.P. Poncelet, D.N. Kennedy, B.E. Hoppel, M.S. Cohen, R. Turner, H.-M Cheng, T.J. Brady, B.R. Rosen, "Dynamic magnetic resonance imaging of human brain activity during primary sensory stimulation", Proc. Natl. Acad. Sci. (USA), vol. 89, p. 5675, 1992.

[19] P.A. Bandettini, E.C. Wong, R.S. Hinks, R.S. Tikofsky, J.S. Hyde, "Time course EPI of human brain function during task activation", Magn. Reson. Med., vol. 25, pp. 390-397, 1992.

[20] M.S. Albert, G.D. Cates, B. Driehuys, W. Happer, B. Saam, C.S. Springer Jr., A. Wishnia, "Biological magnetic resonance imaging using laser-polarized ^{129}Xe", Nature, vol. 370, pp. 199-201, 1994.

[21] C. H. Durney, "Antennas and Other Electromagnetic Applicators in Biology and Medicine", Proceedings of the IEEE, vol. 80, no. 1, 1992.

[22] Jordan A., Wust P., Scholz R., Tesche B., Fahling H., Mitrovics T., Vogl T., Cervos-Navarro J., Felix R., "Cellular uptake of magnetic fluid particles and their effects on human adenocarcinoma cells exposed to AC magnetic fields in vitro", Int. J. Hyperthermia, vol. 12, pp. 705–722, 1996.

[23] O. S. Nielsen, M. Horsman, J. Overgaard, "A future for hyperthermia in cancer treatment?", European Journal of Cancer Volume 37, Issue 13, pp. 1587-1589, 2001.

[24] N. M. S. Reddy, V. Maithreyan, A. Vasanthan, I. S. Balakrishnan, B. K. Bhaskar, R. Jayaraman, V. Shanta, S. Krishnamurthi, "Local RF capacitive hyperthermia: Thermal profiles and tumour response", Int. J. Hyperthermia, vol. 3, no. 4, pp. 379-387, 1987.

[25] F. K. Storm, R. S. Elliott, W. H. Harrison, and D. L. Morton, "Clinical RF hyperthermia by magnetic-loop induction: A new approach to human cancer therapy", IEEE Trans. Microwave Theory Tech., vol. 30, pp. 1124-1158, 1982.

[26] G. H. Nussbaum, J. Sidi, N. Rouhanizadeh, P. Morel, C. Jasmin, G. Convert, J. P. Mabire, G. Azam, "Manipulation of central axis heating patterns with a prototype, three-electrode capacitive device for deep-tumor hyperthermia", IEEE Trans. Microwave Theory Tech., vol. MIT-34, pp. 620-625, 1986.

[27] G. C. Van Rhoon, A. G. Visser, P. M. Van Den Berg, and H. S. Reinhold. "Evaluation of ring capacitor plates for regional deep heating", Int. J. Hyperthermia, vol. 4, pp. 133-142, 1988.

[28] M. J. Hagmann, "Optimization of helical coil applicators for hyperthermia", IEEE Trans. Microwave Theory Tech., vol. 36, pp. 148-150, 1988.

[29] F. K. Storm, R. S. Elliott, W. H. Harrison, D. L. Morton, "Clinical RF hyperthermia by magnetic-loop induction: A new approach to human cancer therapy", IEEE Trans. Microwave Theory Tech., vol. 30, pp. 1124-1158, 1982.

[30] P. G. Cottis, N. K. Uzunoglu, G. E. Chatzarakis, "A multiloop concentric hyperthermia applicator with enhanced penetration depth", IEEE Trans. Microwave Theory Tech., vol. 36, pp. 676-681, 1988.

[31] Veepsa Bhatia, "Antennas and Other Electromagnetic Applicators in Biology and Medicine", Proc. URSI, 2005.

[32] Q. A. Pankhurst, J. Connolly, S. K. Jones, J Dobson, "Applications of magnetic nanoparticles in biomedicine", J. Phys. D: Appl. Phys., vol. 36, pp. 167-181, 2003.

[33] Lübbe A. S., Bergemann C., Brock J., McClure D. G., "Physiological aspects in magnetic drug-targeting", J. Magn. Magn. Mater., vol. 194, pp. 149-55, 1999.

[34] Hilger I., Fruhauf K., Andra W., Hiergeist R., Hergt R., Kaiser W. A., "Heating potential of iron oxides for therapeutic purposes in interventional radiology", Acad. Radiol., vol. 9, pp. 198-202, 2002.

[35] Hilger I., Andra W., Hergt R., Hiergeist R., Schubert H.,Kaiser W. A., "Electromagnetic heating of breast tumours in interventional radiology: in vitro and in vivo studies in human cadavers and mice", Radiology vol. 218, pp. 570-575, 2001.

[36] Moroz P., Jones S. K., Gray B. N., "Magnetically mediated hyperthermia: current status and future directions", Int. J. Hyperthermia, vol. 18, pp. 267–284, 2002.

[37] Atkinson W. J., Brezovich I. A., Chakraborty D. P., "Usable frequencies in hyperthermia with thermal seeds", IEEE Trans. Biomed. Eng. BME vol. 31, pp. 70-75, 1984.

[38] Rosensweig R. E., "Heating magnetic fluid with alternating magnetic field", J. Magn. Magn. Mater., vol. 252, pp. 370-374, 2002.

[39] Hergt R., Andra W., d'Ambly C., Hilger I., Kaiser W., Richter U., Schmidt H., "Physical limits of hyperthermia using magnetite fine particles", IEEE Trans. Magn., vol. 34, pp.3745-3754, 1998.

[40] R. Hergt, S. Dutz, "Magnetic particle hyperthermia—biophysical limitations of a visionary tumour therapy", Magn. Mater., vol. 311, no. 1, pp. 187-192, 2007.

PART II

DESIGN OF EXPOSURE SYSTEMS FOR *IN VITRO* BIOEXPERIMENTS

Chapter 3

Electromagnetic Dosimetry

Although well-defined exposure conditions for biological experiments are an obvious and indispensable prerequisite for interpretation and reproducibility of results, the diffculties involved in obtaining such conditions have been severely underestimated by most groups conducting RF experiments. Consequently, design and characterization of exposure setups have become top priority within bioelectromagnetic research [1].

In this context, the need to assess criteria in order to ensure the repeatability and reproducibility of results has been suggested. The major shortcomings in the field of bioelectromagnetic research, resulting in inconclusive or conflicting results obtained by several laboratories, are attributable to inaccurate dosimetry control or, more simply, a lack of identical exposure conditions [2].

In this chapter a novel approach to the design of exposure systems for bioexperiments is proposed; in particular the dosimetric parameters will be defined and the main methods which are at the base of both numerical and experimental dosimetry are presented.

3.1 Guidelines for development of in vitro exposure systems

Different reviews on exposure setups are present in literature [3,4,5], even if a more recent study of Kuster and schonborn [1] stressed the importance of the development of optimized setups for specific bio-experiments. They suggest guidelines and a procedure for design, optimization, construction, and verification of exposure setups in order to facilitate their development and utilization with respect to all the strict requirements for sound biological experiments.

In [1] the basic requirements that should be considered in the evaluation of a particular exposure system are listed; they are divided in: 1) "biological requirements", 2) "electromagnetic requirements" and 3) "other requirements".

The working hypothesis of the study should first be precisely formulated. The rationale upon which the hypothesis is based should be carefully examined and its significance with respect to the overall objective, e.g., health risk, therapeutic applications, etc., should be evaluated. This includes implications for the exposure, e.g., minimum number of samples required to achieve the needed statistical significance, induced field strengths, duration, modulation, etc.

The biological requirements involve the biological protocol, infact the most limiting requirements and constraints on the exposure setup are usually those imposed by the minimum requirements of the biological experiment itself. Requirements may dictate the equipment needed (e.g., access to devices for the control of biological properties of the exposed samples, restrictions to certain flasks), procedures (e.g., handling, fast access during the experiment, certain cell distributions within the experiments, etc.), and the environment (e.g., temperature, pressure, atmospheric control, etc.). The overall duration of the experiment influences the choice of design and materials for the setup. In addition the number of exposed samples is another constraint necessary for statistical significance. Finally it is to be considered the possibility of a single or double blind study design.

The electromagnetic requirements are an indispensable prerequisite for obtaining results that can be apptopriately interpreted and replicated. First of all the signal characteristics have to be established, hence frequency and type of applied modulation. The last infact is a crucial aspect above all if the exposure system id developed in order to evaluate possible health hazard induced by the utilization of wireless devices. The modulation must be relevant with regard to the overall objective of the study; further the duration of exposure should reasonably reflect the maximum daily exposure.

A main electromagnetic requirement is the field distribution into the sample. In particular, the induced field distribution of *in vitro* experiments should be as homogeneous as possible. Although the geometry of the cell culture may be simple (e.g., monolayer of cells in a Petri-dish), excellent homogeneity is quite diffcult to achieve. An

overall standard deviation from homogeneity of less than 30% is reasonable and should be aimed at. Since the distributions of the induced field strengths often considerably deviate from normal distributions, distribution charts should be provided as well as an adequate description of the polarization of the induced fields. Another important parameter cheracterizing the performance of a system is the efficiency of the field applicator. It is to be noted that different authors give different meanings to "uniformity" and "efficiency". In the next paragraph of this chapter a clear and unique definition of the dosimetric parameters is given [6].

Concerning other requirements of an exposure setup, the sensitivity of experimental variation on the induced field strength and distribution should be minimal.

All controlling and monitoring devices should be rigorously checked for electromagnetic interference (EMI) under worst-case considerations. Otherwise interference may cause failures or malfunctions of system components (e.g., of the temperature controlling circuit).

The fields radiated by the system beyond the confines of the laboratory should be electromagnetically compatible (EMC) with commercial wireless services. The exposure setup should not subject personnel to exposures exceeding the safety standards.

Fields RF exposure setups may also produce ELF fields. These unwanted fields must be characterized and kept as small as possible.

Other requirements deal with the control of the exposure system, the setup should enable monitoring of all relevant technical and biological parameters during the course of the experiment.

The setup should be sufficiently failure tolerant to be handled by non-engineering personnel. Finally the cost of the setup should be reasonable.

3.2 Numerical Dosimetry

It is well known that meaningful laboratory experiments on biological effects of electromagnetic fields must include a very accurate knowledge of the electromagnetic stimulus to which the biological sample is exposed; in particular a very careful dosimetry is always

necessary. As already said, however, different authors give different meanings to uniformity and efficiency and some difficulty arises in comparing different exposure set-ups. A clear and unique definition of the dosimetric parameters will be given in this section and a somehow new design approach is presented.

3.2.1 Dosimetric Parameters

   The power deposition pattern inside the samples is evaluated numerically by using commercial codes like CST-MWS and Ansoft HFSS, the first based on the Finite Integration Technique (FIT) [7] and the second on the Finite Element Methods (FEM) [8].

   The relative permittivity ε_r and effective conductivity σ_{eff} of the culture medium used for numerical dosimetry have to be previously well established.

   Given P_0, the incident power at the input port of the applicator device, some backward reflected power P_r was also present there, and accordingly P_0 - P_r was the input power. However taking as a reference the incident power alone ($P_0 = 1$ W), the following parameters should be calculated.

- $\left|E^1(x,y,z)\right|$: the local electric field amplitude per unit incident power [(V/m)/W]. This has to be evaluated at each node of the computing domain.

- $SAR^1(x,y,z) = \sigma \dfrac{\left|E^1\right|^2}{2\rho}$: the local absorbed power per unit mass and per unit incident power [(W/kg)/W]. This is also the local specific efficiency, and it is zero outside the sample ($\sigma = 0$). It is understood that, should the incident power be $P_0 \neq 1$ W, the local absorbed power per unit mass would be: $P_0 \times SAR^1(x,y,z) = SAR(x,y,z) =$ specific absorption rate [W/kg].

- AV^1: the average $SAR^1(x,y,z)$ over the sample [(W/kg)/W]. This is also the average specific efficiency. Given the sample mass m and the total power absorbed by the sample Pa, $m \times AV^1 = \dfrac{P_a}{P_0}$ is the overall efficiency.

Under high efficiency conditions the power lost on the walls of the

applicator is negligible in comparison with the power absorbed by the sample, P_a. This makes it simple to relate overall efficiency to the scattering parameters (s_{11}, s_{21}) [9] of the applicator:

$$\frac{P_a}{P_0} = 1 - |s_{11}|^2 - |s_{21}|^2 .$$

Numerical evaluations of P_a/P_0 (and AV^1) could thus be checked by measuring the amplitude of the reflection coefficient $|s_{11}|$.

The microwave power depositioning pattern (local SAR^1 values) is always non-uniform, and a given AV^1 (average SAR^1) may correspond either to a nearly uniform pattern, or to local SAR^1 maxima much larger than minima. The biological effects, observed on the whole sample, are likely to be different in the above two cases despite the same AV^1: thus a "nonuniformity degree" must be calculated for characterizing the exposure conditions.

- SD^1: the standard deviation of $SAR^1(x,y,z)$ values is a basic nonuniformity (dispersion) parameter [17], but
- $CV = SD^1/AV^1$: the coefficient of variation [10] is usually taken [1] as the "nonuniformity degree"of the SAR^1 ($P_0 = 1$ W) values. The SAR (any P_0) nonuniformity degree, SD/AV, is the same as $CV = SD^1/AV^1$. CV values of the order of 0.3 (or less) are considered acceptable [1].

Given that in some cases the biological target is limited to a cell monolayer, the average SAR^1 (AV^1) and the nonuniformity degree (CV) are calculated both for the whole sample (w.s.) and for the bottom layer (b.l.) alone.

For a more in-depth analysis of the power deposition pattern, the local SAR^1 values are normalized to the average value AV^1 (the same value is obtained by normalizing the local SAR to AV, the average SAR):

- $SAR_n(x,y,z) = \dfrac{SAR^1(x,y,z)}{AV^1} = \dfrac{SAR(x,y,z)}{AV}$: the local normalized SAR.

This dimensionless SAR_n describes the power deposition pattern regardless of the average SAR. A contour plot of SAR_n can be drawn for each plane in the sample, and in particular for the bottom layer.

By subdividing the SAR_n whole range into a number of small

intervals, the aliquots of calculated nodes, where the SAR_n value belongs to each given small interval (the normalized statistic frequencies [10] of the SAR_n values), give:

- SAR_n PDF: the probability density function (histogram) of the SAR_n.

The aliquots of calculated nodes, where the SAR_n value is less than or equal to a given value, give:

- SAR_n CDF: the (integral) cumulative distribution function of the SAR_n.

Dealing with high frequency fields and *in vitro* experiments on homogeneous samples, a uniform pattern of the absorbed power would allow a very simple characterization (local value = space average value) of the exposure condition (at least as long the field intensity level is concerned). Unfortunately the field intensity (and the absorbed power density, or specific absorption rate, SAR, W/kg) are never uiform, so that the SAR space average value (AV), although giving some information, is definitively inadequate for a quantitative description of the exposure condition (should the local biological effect be a linear function of the local SAR, in this case only the effect on the whole sample would depend on the average SAR, regardless of its space distribution [9]).

Numerical simulations (and to a certain extent local measurements) can give the space distribution of the SAR in each special case, allowing the evaluation of the statistical occurrence (PDF and CDF) of the SAR values. However for comparison purposes between different exposure conditions a concise "non-uniformity degree" (the coefficient of variation, CV) has been accepted as meaningful: in fact CV values of 0.3 or less are considered acceptable [1].

Other meaningful parameters, characterizing the exposure conditions, are the "specific efficiency", (W/kg)/W, and the overall efficiency of the applicator, i.e. the ratio P_a / P_0, between the power Pa, absorbed by the sample, and the power P_0, incident at the input port of the applicator; being understood that some power Pr is reflected back to the generator. It is worth noting that some authors refer the absorbed power Pa, to the input power $(P_0 - P_r)$, instead of the incident one Po; but in this case a lossless applicator $(P_a = P_0 - P_r)$ would exhibit always efficiency = 1, regardless of the reflected power.

Design criteria are usually based on the unperturbed field pattern [1, 11]: the unloaded applicator, in fact, is a much more simple structure than the loaded one, and in some cases even the exact analytical field solution is known. Sample positioning and orientation are thus established with reference to the unperturbed field and the evaluation of the "non-uniformity" (CV) and "efficiency" (AV[1]) is carried out as a final check of the successful design of the applicator.

A novel approach [6, 12] consists simply of taking into account CV and AV[1] from the beginning of the design, by calculating them on the loaded applicator under different working conditions and defining in this way the optimum configuration of the applicator.

According to this philosophy, numerical simulations are used for modelling the loaded applicator, by varying some basic parameters until the best trade-off between field uniformity and power efficiency was found. From the other side, that one of the experimental checks, besides the use of microwave network analyzer for efficiency measurements, an indirect approach was proposed for testing the calculated non-uniformity degree (CV).

3.3   Experimental dosimetry

Given that the performances of the field applicator device are expressed by: i) the non-uniformity degree CV (possibly low) and ii) the specific efficiency AV[1] (possibly high), the question is how to validate by measurements the calculated values of the above two parameters. About the CV parameter, some authors do perform the experimental mapping of the local SAR values by means of either field measurements [13, 14] or temperature measurements [15, 16], in order to check the attainment of the desired (possibly low) non-uniformity of the power deposition pattern; but special instrumentation and care are necessary for measuring small SAR differences under low CV conditions.

The proposed approach, instead, suggest to check the effectiveness of the numerical simulation tool (the computer code), by measuring local SAR values under high incident power, Po, conditions. This strongly reduces probe sensitivity and resolution problems.

3.3.1 Local SAR Measurements

The local calculated microwave power distribution is validated by means of calorimetric measurements performed under high incident power. Local SAR evaluations are carried out by analyzing heating and cooling curves [17] recorded at different points of a control sample by means of a fluoroptic thermometer with fiber optic temperature probes. In particular, the local SAR values are calculated from the slope of the heating curves, T(t), at t = 0, as: $SAR = c \dfrac{dT}{dt}\bigg|_{t=0}$,

c being the sample specific heat: c = 4186 J/kg °K. Because back extrapolation of T(t) at t = 0 is not feasible, and in order to neglect errors due to heat diffusion or convection, the approach of Moros and Pickard [15] is used. The time window over which temperature variation associated with SAR is measured, satisfies the inequality

$t_m \leq \dfrac{\alpha^2}{\pi^2 D}$ where α [m] is the half-width at half-maximum of the SAR

distribution and D is the thermal diffusivity, $D = k/(\rho c \ [m^2/s]$, k being the thermal conductivity [18].

An uncertainty for the SAR assessment of $\pm$ 20% was estimated, due to combined contributions of several parameters as calibration of the probe, determination of medium volume, probe positioning in the sample, assessment of the absorbed power.

3.3.2 Efficiency measurements

The calculated values of the overall efficiency Pa/P_0 (and of the average specific efficiency AV^1) are checked by measuring, over the band of interest the amplitude of the reflection and transmission coefficients (the scattering parameters s_{11} and s_{21}) of the applicator loaded by the samples. The measurements are performed by means of a microwave vector network analyzer. For this type of measurements an uncertainty of $\pm 5\%$ is estimated.

3.4   Conclusions

In this chapter an approach to the design of expoure setups for in vitro bioexperiments has been proposed. Firstly the working hypothesis of the study has to be precisely formulated, then the basic design requirements both biological and electromagnetic ones have to be individuated. Once these basic criteria are established, the electromagnetic dosimetry is carried out. In particular, the proposed approach consists simply of taking into account CV and AV^1 from the beginning of the design, by calculating them on the loaded applicator under different working conditions and defining in this way the optimum configuration of the applicator.

A careful numerical analysis is carried out in order to model the loaded applicator, by varying some basic parameters until the best trade-off between field uniformity and power efficiency was found.

In this chapter the dosimetric parameters which have to be investigated have been defined and the methodology of carrying out nemerical and experimental dosimetry is presented.

Successful outcomes of this design philosophy are given in ref. [19, 20]. In ref. [19] the working frequency was 900 MHz, and the cells are kept in 8 ml and 15 ml cell cultures, contained respectively in T25 or T75 rectangular flasks. The applicator was a rectangular waveguide (248mm x 124mm) and different configurations were considered in order to assess the optimum orientation and positioning of the cell cultures inside the waveguide chamber. The performance of the system was found to be optimal when the electric field is parallel to

the sample and the waveguide is terminated by a matched load. In this condition two 15 ml or four 8 ml cells cultures can be exposed. In the chosen exposure configuration, the efficiency was 0.40 and the nonuniformity degree was 0.39 for the 15 ml samples. For the 8 ml samples, the efficiency was 0.19 and a low nonuniformity degree (0.15) was found. Due to the chosen polarization of the unperturbed field, the results were almost identical for the bottom layer and the bulk of the culture medium.

In ref. [20] the working frequency was still 900 MHz, and the same rectangular waveguide was used, but in this case the biological samples were hosted in 96 well (0.1 ml each) plastic plates. According to the presented exposure optimization technique it was found that two half-loaded (48 wells) plates can give CV = 0.28, and a specific efficiency AV1 = 0.37 (W/kg)/W. But the overall efficiency of the device was rather low (0.01).

Following the guidelines and the numerical and experimental dosimetric methods previously described, some exposure systems have been designed, realized and characterized, in order to carry out *in vitro* experiments for different bioelectromagnetic research programs.

References

[1] Kuster, F. Schonbörn, "Recommended minimal requirements and development guidelines for exposure setups of bio-experiments addressing the health risk concern of wireless communications", Bioelectromagnetics, vol. 21, no. 7, pp. 508-514, Oct., 2000.

[2] Vijayalaxmi, Guenter Obe, "Controversial Cytogenetic Observations in Mammalian Somatic Cells Exposed to Radiofrequency Radiation", Radiation Research, vol. 162, pp. 481-496, 2004.

[3] Chou C.K., Chan K.W., McDougall J.A., Guy A.W., "Development of a rat head exposure system for simulating human exposure to RF Fields From Handheld wireless telephones", Bioelectromagnetics, vol. 20 (Suppl 4), pp. 75-92, 1999.

[4] Kuster N. "Dosimetric needs for laboratory and epidemiological research. In: Bernhardt et al., editors. Nonthermal effects of RF electromagnetic fields", München: ICNIRP, pp. 27-34, 1997.

[5] Guy A.W., Chou C.K., McDougall J.A., "A quarter centery of in vitro research: A new look on exposure methods", Bioelectromagnetics, vol. 20 (Suppl 4) , pp. 21-39, 1999.

[6] M.L. Calabrese, G. d'Ambrosio, R. Massa, G. Petraglia, "In vitro dosimetry: a novel approach in the design of applicators for bioelectromagnetic experiments", Proc. 3rd Int. Workshop on Biological Effects of Electromagnetic Fields, Kos, Greece, 4 – 8 Oct. 2004, ISBN 960-233-151-8, pp. 18-21.

[7] T. Weiland, "On numerical solution of Maxwell's equation and application in the field accelerator physics", Particle accelerators, vol. 15, no. 4, pp. 245-292, Jan., 1984.

[8] Jianming Jin, "RF Fields in Biological Objects", Electromagnetic Analysis and Design in Magnetic Resonance Imaging, CRC Press LLC, Florida, USA, 1999, Chapter 5, pp. 224-226.

[9] David M. Pozar, "Microwave network analysis", Microwave Engineering, 1st ed., New York, USA: Addison-Wesley Publising Co. Inc., 1993, Chapter 5, pp. 220-230.

[10] R. R. Sokal, F. J. Rohlf, "Biometry", 1st ed., San Francisco, California, USA: W. H. Freeman and Co., 1969, Chapter 4, pp. 50-63.

[11] F. Schönborn, K. Poković, A.M. Wobus, N. Kuster, "Design, optimization, realization and analysis of an in vitro setup for the exposure of embrional stem cells at 1.71 GHz", Bioelectromagnetics, vol. 21, issue 5, pp. 372-384, July, 2000.

[12] Calabrese M.L., d'Ambrosio G., Massa R., Petraglia G., "A High-Efficiency Waveguide Applicator for In Vitro Exposure of Mammalian Cells at 1.95 GHz", IEEE Trans. Microwave Theory and Tchniques 54 (5): 2256-2264, 2006.

[13] M. Burkhardt, K. Poković, M. Gnos, T. Schmid, N. Kuster, "Numerical and Experimental Dosimetry of Petri Dish Exposure Setups", Bioelectromagnetics, Vol. 17, pp. 483-493, 1996.

[14] F. Schönborn, K. Poković, A.M. Wobus, N. Kuster, "Design, optimization, realization and analysis of an in vitro setup for the exposure of embrional stem cells at 1.71 GHz", Bioelectromagnetics, vol. 21, issue 5, pp. 372-384, July, 2000.

[15] E.G. Moros and W.F. Pickard, "On the assumption of negligible heat diffusion during the thermal measurement of a nonuniform specific absorption rate", Radiation Research, vol. 152, issue 3, pages 312–20, Sep.,1999.

[16] W.F. Pickard, W.L. Straube, E.G. Moros, 'Experimental and numerical determination of SAR distributions within culture flasks in a dielectric loaded radial transmission line' , IEEE Trans. Biomedical Engineering, vol. 47, issue 2, pp. 202-208, Feb., 2000.

[17] J.W. Allis, C.F. Blackman, M.L. Fromme, S.G. Benane, "Measurement of microwave radiation absorbed by biological systems. Analysis of heating and cooling data", Radio Sci., vol. 12, issue 6(s), pp. 1-8, 1977.

[18] J. Schuderer, T. Samaras, W. Oesch, D. Spät, N. Kuster, "High Peak SAR Exposure Unit With Tight Exposure and Environmental Control for In Vitro Experiments at 1800 MHz", IEEE Trans. Microwave Theory and Tech., vol. 52, issue 8, pp. 2057-2066, Aug., 2004.

[19] G. De Prisco, G. d'Ambrosio, M. L. Calabrese, R. Massa, J. Juutilainen, "SAR and Efficiency evaluation of a 900 MHz Waveguide Chamber for Cell Exposure", accepted, Journal of Bioelectromagnetics, 2007.

[20] M. L. Calabrese, G. d'Ambrosio, R. Massa, G. Petraglia, "Numerical and Experimental Dosimetry for a Waveguide

Exposure Chamber Designed for Exposing Cell Culture   in
different containers to 900 MHz electromagnetic fields", EHE'06
– Int. Conf. on Electromagnetic Fields, Health and Environment,
Madera, Portugal, April 2006.

Chapter 4

Design and realization of exposure systems

In this chapter standardized exposure devices for different set of *in vitro* bioelecromagnetic experiments will be presented. The exposure systems are designed, realized and characterized on the basis of efficiency and field uniformity criteria. In particular, a WR-430 waveguide terminated with a short circuit plate was chosen in order to expose mammalian cells cultures at the UMTS signal (1.95 GHz) within a coordinated research program on "Wireless Technology Health Risks (WITHER)". In the ambit of another research program on the evaluations of genotoxic and non genotoxic effects induced by EMF at wireless frequencies, an exposure setup at 900 MHz was designed and characterized.

4.1 A high efficiency waveguide applicator at 1.95 GHz

In a coordinated research program on "Wireless Technology Health Risks (WITHER)", within the framework of the "Regional Centre of Competence on Information and Communication Technologies of Campania Region (CRdC ICT)", four research groups, one at the Department of Electronic and Telecommunication Engineering (DIET), one at the Department of Physical Sciences (DSF), both of "Università di Napoli Federico II" (UNINA), one at the Institute for Electromagnetic Sensing of the Environment (IREA), and one at the "Pascale" National Institute of Tumours, jointly focused on evaluating cancer related endpoints in mammalian cells following in vitro exposure to radiofrequency wireless signals [1, 2].

A key point of the project was to design and set up a standardized field applicator, which could be used for all the planned biological experiments carried out in the various laboratories. The working frequency chosen was 1.95 GHz (an uplink frequency of the Universal Mobile Telecommunications System, UMTS). The signal was generated by an Agilent E4432B, ESG-D series signal generator, and a WCDMA standard, according to the 3GPP 3.5 2001-03 specifications, was used.

The design of this applicator device was driven by efficiency and SAR uniformity criteria. Of course different possibilities have been considered: transverse electromagnetic cell TEM [3], radial transmission line RTL [4], wire patch cell WPC [5], and free-space operated systems [6]. But, in agreement with [7], a rectangular waveguide was preferred and chosen (WR 430: 109.2 mm × 54.6 mm, which is readily available) as the basic structure of our microwave applicator; resonant operation [8] was discarded because of limitations in the modulation bandwidth of the feeding signal (UMTS).

The primary goal of this work was to determine the optimum orientation of the Petri dish samples relative to the internal waveguide electric (E) and magnetic (H) fields. Six different cases were examined and the optimum was found to be the E parallel case (Fig. 4.1a).
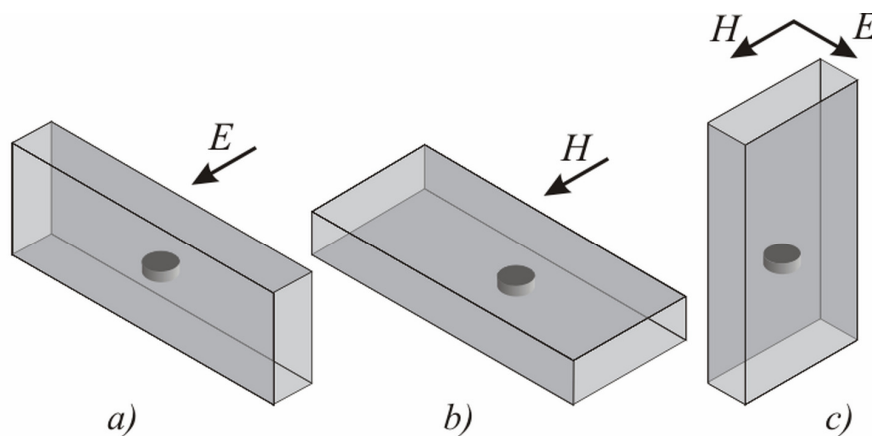
Fig. 4. 1. (a) E parallel: Ep case; (b) H parallel: Hp case; (c) E parallel, H parallel: EpHp case.

4.1.1 Numerical dosimetry

The applicator waveguide walls were assumed to be a perfect electric conductor (p.e.c.) and the magnetic properties of the materials were taken as those of the free space ($\mu = \mu_0$). Rectangular flasks were discarded because their shape favours the nonuniformity of the power depositioning pattern in the liquid sample [9], and circular Petri dishes (Falcon, 3001F), filled with 3 ml culture, were chosen. The sample was assumed to have a perfectly cylindrical shape (diameter: 34 mm; thickness: 3.3 mm): the meniscus at the top of the sample was not taken into account, but this could give a significant error in the "Hp case" only [10, 11]. The culture medium was Dulbecco's Modified Eagle Medium (DMEM), whose complex relative permittivity ($\varepsilon' - j\varepsilon''$) and density ρ at 37°C are [12]: $\varepsilon' = 75$, $\varepsilon'' = 20.3$, and $\rho = 1060\,kg/m^3$, being $\sigma = 2.2\,S/m$; $\omega = 2\pi \times 1.95 \times 10^9$; $\varepsilon_0 = 1/(36\pi \times 10^9)$ and $\varepsilon'' = \sigma/\omega\varepsilon_0$.

The study basically aims to find out how applicator performance (in terms of average specific efficiency AV^1 and nonuniformity degree CV) is affected by two factors: 1) the **sample aspect** with reference to the unperturbed field vectors (E, H) at the centre of the transverse section of the empty waveguide, and 2) the **waveguide termination** beyond the sample.

1) **Sample aspect**. Given that the sample layer is always horizontal, by keeping the longitudinal axis and the narrow side of the waveguide horizontal (Fig. 4.1a) the unperturbed E vector (empty waveguide) is parallel (E_p case) to the sample layer. By keeping the longitudinal axis and the wide side of the waveguide horizontal (Fig. 4.1b) the unperturbed H vector is parallel (H_p case) to the sample layer. By keeping the longitudinal axis of the waveguide vertical (Fig. 4.1c) the unperturbed E and H vectors on the axis of the waveguide are both parallel (E_pH_p case) to the sample.

2) **Waveguide termination**. The feeding end of the waveguide (left side in Fig. 4.2b) was assumed to be perfectly matched,

and a short circuit (SC) waveguide termination of variable length (right side in Fig. 4.2b) was analyzed first.
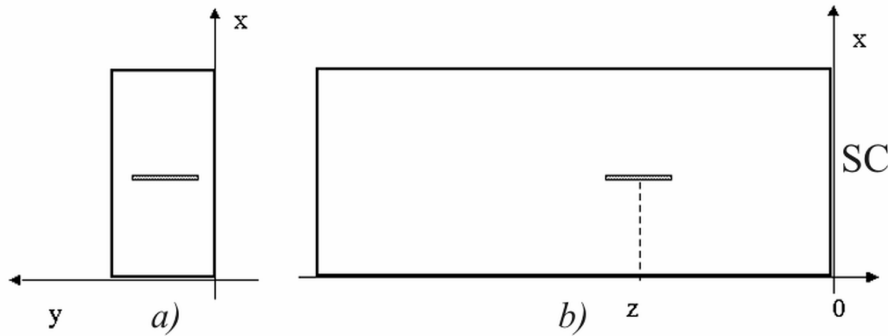
Fig. 4. 2. (a) Ep case (same as in Fig. 1a), waveguide transverse section. (b) Ep case, waveguide longitudinal section: sample positioning/ length of the short-circuited termination

One quarter waveguide wavelength $(0.25\lambda_z)$ gives infinite input impedance (open circuit, unperturbed E field maximum), one half wavelength $(0.5\lambda_z)$ gives zero impedance (short circuit, unperturbed H field maximum). A matched load termination (ML, not shown) was also considered.

By combining waveguide termination and sample aspect, six cases have been analyzed: 1) SC/E$_p$; 2) SC/H$_p$; 3) SC/ E$_p$H$_p$; 4) ML/E$_p$; 5) ML/H$_p$; 6) ML/E$_p$H$_p$. In the first evaluations one cylindrical liquid sample alone, was taken into consideration, and its centre was positioned on the longitudinal axis of the waveguide (Fig. 4.2). The mesh dimensions of the computing grid outside the sample were: $\Delta x = \Delta y = \Delta z = 10mm$, the wavelength in air being $\lambda_0 = 154mm$; while inside the sample, the mesh dimensions were $\Delta x = 0.1mm$ (vertical direction), and $\Delta z = \Delta y = 1mm$ (horizontal directions), the wavelength in the culture being $\lambda = 18mm$.

 Case 1: SC/E$_p$. In Figs. 4.1a) and 4.2b) the E$_p$ aspect and a short circuit (SC) termination of variable length |z| are shown (the short circuit is at z = 0, and the centre of the sample is at z < 0).

 In Fig. 4.3 the average specific efficiency AV[1], in the whole sample (w.s., solid line) and in the bottom layer (b.l., dashed line), is

plotted as a function of the position of the centre of the sample. The following remarks can be made: the bottom layer behaviour is quite similar to that of the whole sample but there is a small decrease in efficiency;   the maximum nearest to the short circuit occurs at $z = -0.56\lambda_z$, both for the whole sample (solid line, AV^{1}max = 274 (W/kg)/W), and for the bottom layer (dashed line, AV^{1}max = 234 (W/kg)/W); the above position is different from both the unperturbed E field maximum position (- 0.25 λ_z) and the unperturbed H field maximum position (- 0.5 λ_z);   other maxima positions are spaced 0.5 λ_z; maxima are narrow peaks, so a careful positioning of the sample is necessary in order to ensure optimum efficiency.
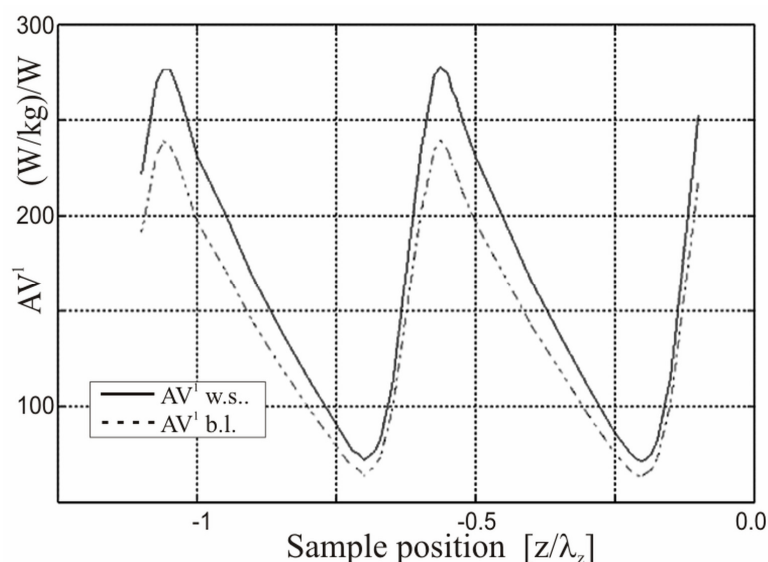
Fig. 4. 3. Average specific efficiency AV1, in the whole sample (w.s. – solid line) and in the bottom layer (b.l. – dashed line), as a function of the positioning of the centre of the sample. The positioning is given in terms of the abscissa, z, normalized to the waveguide wavelength: z / λz .
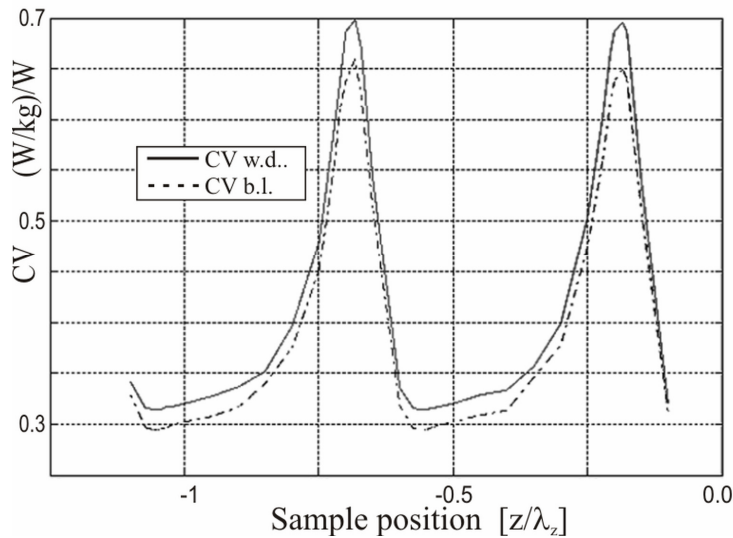
Fig. 4. 4. Nonuniformity degree CV, in the whole sample (w.s. – solid line) and in the bottom layer (b.l. – dashed line), as a function of the positioning of the centre of the sample. The positioning is given in terms of the abscissa, z, normalized to the waveguide wavelength, z / λz .

In Fig. 4.4 the nonuniformity degree CV, in the whole sample (w.s., solid line) and in the bottom layer (b.l., dashed line), is plotted as a function of the position of the centre of the sample. The following remarks can be made: in the bottom layer the CV behaviour is quite similar to that of the whole sample, but an even better uniformity (lower CV) can be obtained; the minimum of the nonuniformity degree CV (uniformity maximum) closest to the short circuit occurs again at $z = - 0.56 \ \lambda_z$, both for the whole sample (solid line, CVmin = 0.31), and for the bottom layer (dashed line, CVmin = 0.29); the above position is different from both the unperturbed E field maximum position (- 0.25 λ_z) and the unperturbed H field maximum position (- 0.5 λ_z); other minima positions are spaced 0.5 λ_z;minima are poorly peaked, so for optimum uniformity no critical positioning of the sample is necessary.

A further remark that can be inferred from Figs. 4.3 and 4.4 is that both maximum efficiency and maximum uniformity are found in the same position ($z = - 0.56 \ \lambda_z$); so no trade-off is necessary. Minimum

efficiency and maximum nonuniformity are again found in one position ($z = -0.20\ \lambda_z$) (worst case).

AV^1 and CV values at $z = -0.50\ \lambda_z$ and at $z = -0.56\ \lambda_z$ (minimum of unpertubed E field) are compared in Table 4.I. It is shown that the proper positioning of the (latter) sample increases the average specific efficiency AV^1 by nearly 20 %, and also reduces the nonuniformity degree CV, both in the whole sample and in the bottom layer alone. By taking into account the sample mass ($m = 3.18 \times 10^{-3}$ kg), at $z = -0.56\ \lambda_z$ a very high overall efficiency is also found: $m \times AV^1 max = Pa/Pi = 0.87$.

	$z = -0.50\lambda_z$	$z = -0.56\lambda_z$	$z = -0.50\lambda_z$	$z = -0.56\lambda_z$
	AV^1 (W/kg)/W	AV^1max (W/kg)/W	CV	CVmin
whole sample	230	274	0.32	0.31
bottom layer	196	234	0.30	0.29

TABLE 4. I. SHORT CIRCUIT TERMINATION, COMPARISON BETWEEN TWO SAMPLE POSITIONS

The SAR_n probability distribution function histograms (PDF) and the corresponding cumulative distribution function (CDF) diagrams were drawn for the whole sample (w.s., Fig. 4.5) and for the bottom layer alone (b.l., Fig. 4.6) under CVmin conditions. The more highly peaked PDF plot for the bottom layer corresponds to a greater uniformity. The CDF plots show that 62 % of the whole sample (Fig. 4.5, CV = 0.31), and 70 % of the bottom layer (Fig. 4.6, CV = 0.29) undergo a SAR level in the range (0.7 AV - 1.3 AV).
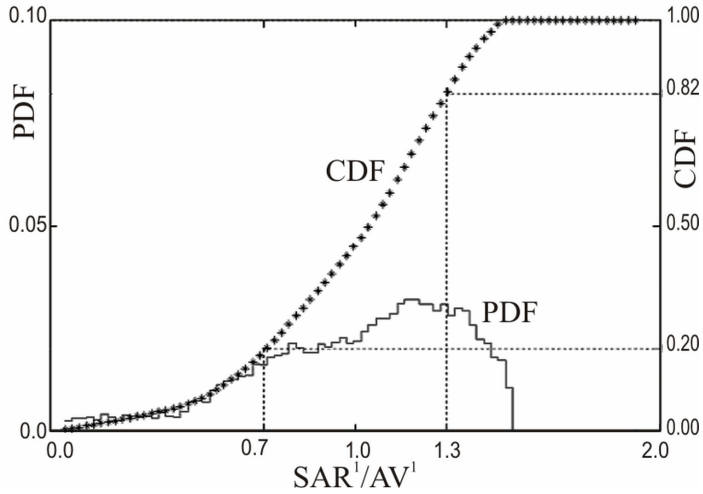
Fig. 4. 5. Case 1: Ep/SC. Whole sample SARn PDF and CDF.
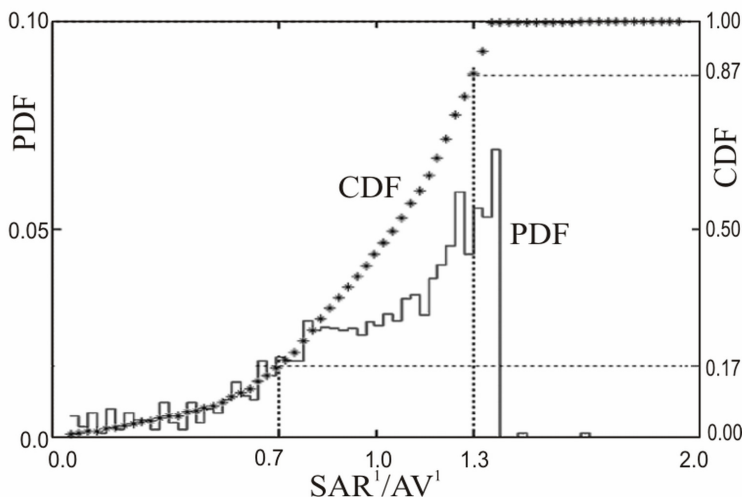
Fig. 4. 6. Case 1: Ep/SC. Bottom layer SARn PDF and CDF.

Cases 1 through 6 are summarized in Table 4.II. The average specific efficiency AV^1, and the nonuniformity degree CV, in the whole sample (w.s.) and in the bottom layer (b.l.) alone, are reported. Under conditions of short circuit (SC) termination (cases 1, 2, and 3), both AV^1max and CVmin were found at the same sample position. Under conditions of matched load (ML) termination (cases 4, 5, and 6), AV^1 and CV do not depend on the sample position along the longitudinal axis.

As already known [13], it is confirmed (case 2) that on the bottom layer a low nonuniformity degree (CV = 0.25, marked with a star) can be obtained with the H_p aspect. However, again in case 2, a high nonuniformity (CV = 0.82) occurs in the whole sample, together with a low average specific efficiency both in the whole sample (AV^1 = 1.13 (W/kg)/W) and in the bottom layer (AV^1 = 2.85 (W/kg)/W).

Whereas, in case 1, as already noted (Figs. 4.3 and 4.4), moderate CV values (marked with a star) can be obtained both in the bottom layer (CV = 0.29) and in the whole sample (CV = 0.31); and at the same time very high values of the average specific efficiency occur (b.l.: AV^1 = 234 (W/kg)/W; w.s.: AV^1 = 274 (W/kg)/W).

		1	2	3	4	5	6
		SC/Ep	SC/Hp	SC/EpHp	ML/Ep	ML/Hp	ML/EpHp
AV^1max	w.s.	274	1.13	2.7	108	0.44	18
(W/kg)/W	b.l.	234	2.85	0.9	97.2	1.00	17
CVmin	w.s.	0.31*	0.82	1.01	0.41	0.62	0.69
	b.l.	0.29*	0.25*	0.37	0.39	0.41	0.55

TABLE 4. II. COMPARISON OF SIX CASES

These results can be qualitatively described by considering the coupling mechanisms. As suggested in [14], the total electric field inside the sample can be separated into the capacitively coupled electric field $\vec{E}_{cap}$, proportional to the incident electric field ($\vec{E}_{inc}$), and the inductively coupled electric field ($\vec{E}_{ind}$), proportional to the incident magnetic field ($\vec{H}_{inc}$). $\left|\vec{E}_{cap}\right|$ is larger if the $\vec{E}_{inc}$ is tangential to the boundary of the medium and smaller if $\vec{E}_{inc}$ is normal to the boundary of the medium; while $\left|\vec{E}_{ind}\right|$ is larger if $\vec{H}_{inc}$ intercepts a larger cross section of the medium. Thus, referring to Table 4.II it is intuitively reasonable that AV^1 would be higher for the E_p case, lower for the H_p case and intermediate in the E_pH_p case, as the electric field is expected to couple strongly to the sample when it is parallel to the sample surface. This is clearly shown in cases 4, 5 and 6 with the

matched load termination; in cases 1, 2 and 3 $\left|\vec{E}_{ind}\right|$ gives the major contribution due to the chosen sample position. In particular, AV^1 is higher for the E_p case (where $\vec{H}_{inc}$ intercepts a larger cross section of the medium) and it is quite similar for the H_p and E_pH_p cases, intercepting $\vec{H}_{inc}$ the same smaller cross section of the medium. In addition, simulations show that the presence of a short circuit plate increases the efficiency, as observed in other apparatuses [7], [11], because of the interactions between the electric fields internal to the sample, due to the incident wave and that reflected by the short. For the same reason a higher uniformity is achieved. Even though a standing wave along the waveguide is also present in the matched load case, due to the high permittivity value of the sample, the comparison between the SC/Ep and ML/Ep field distributions (Fig. 4.7 and Fig. 4.8) suggests that, for the chosen position, a higher symmetry of the electric field distribution is achieved in the SC/Ep case and, consequently, a higher homogeneity. On the contrary, in the H_p case a non homogeneous spatial SAR distribution is expected along the vertical axis, as pointed out in other numerical [11] and experimental [14] studies (even though for different samples, frequencies and exposure systems). The obtained data confirm these results, observing, in the SC/Hp case, a large difference in CV_{min} between the whole sample and the bottom layer: this configuration is excellent for cell monolayer exposure but not suitable for cells in suspension.
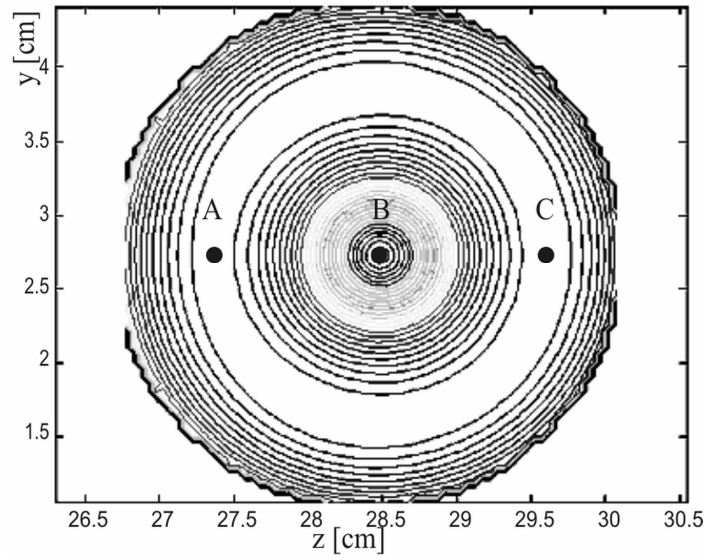
Fig. 4. 7. Contour plot of SAR$_n$ in the bottom layer - SC/Ep
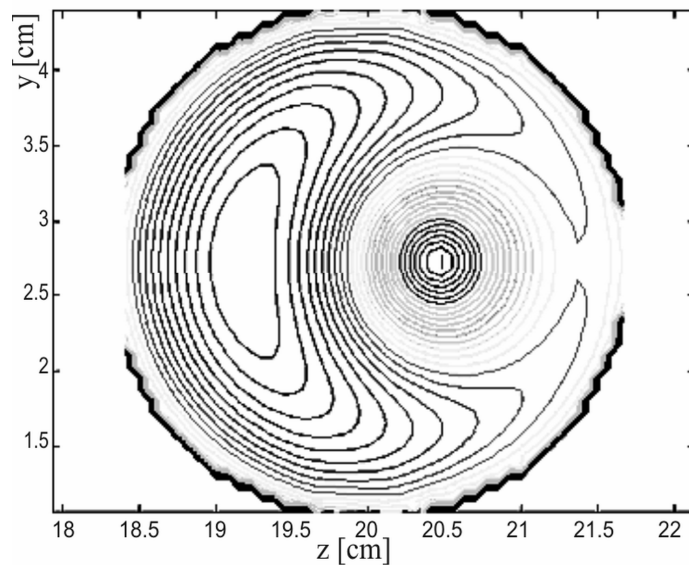
Fig. 4. 8. Contour plot of SAR$_n$ in the bottom layer - ML/Ep.

4.1.1.1   Numerical results: samples, dishes, and plastic stand

In a second step, numerical evaluations were carried out by taking into account the Petri dishes and the plastic stand. Only the case SC/E_p (short circuit termination and E field parallel) was analyzed.
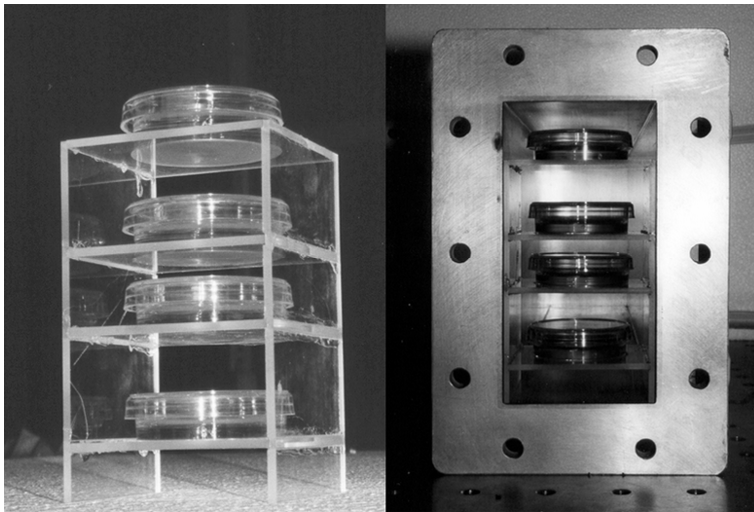
Fig. 4. 9. Four-dish plastic stand and waveguide

Petri dishes are made of polystyrene ($\varepsilon' = 2.4$, $\varepsilon'' \approx 0$) [15], the plastic stands (2 mm thick) (Fig. 4.9) are made of Plexiglas® ($\varepsilon' = 2.6$, $\varepsilon'' \approx 0$) [12]. The mesh dimensions in such structures were the same as in the culture medium. One dish or two or four stacked dishes were considered. The liquid samples, which were all at the same distance from the short circuit termination, were symmetrical to the middle horizontal plane (dashed in Fig. 4.10).
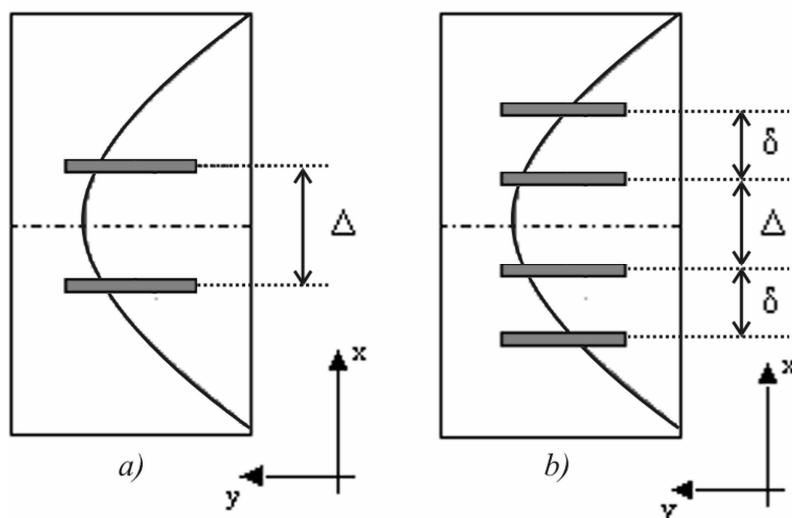
Fig. 4. 10

The results are summarized as follows:

• One dish: Table 4.III shows that, in the presence of Petri dish and plastic stand, a slightly lower average specific efficiency AV^1, and a slightly higher nonuniformity degree CV are found in comparison with the liquid sample alone.

• Two dishes (Fig. 4.10a): owing to the symmetry of the incident field and the sample positions, the two samples undergo basically the same exposure conditions (the plastic dishes and the stand introduce a weak asymmetry). AV^1 and CV were calculated as a function of both the distance |z| from the short circuit, and of the vertical distance Δ between the two samples. The distance from the short circuit |z| = 0.54 λ_z gave the best AV^1 and CV values (the highest AV^1 and the lowest CV). Large Δ values (samples near the bottom and top wall of the waveguide) were found to give a low average specific efficiency AV^1, while small Δ values (both samples near the middle of the waveguide) gave higher efficiency AV^1, but also increased the nonuniformity degree CV, a border effect arose due to the coupling between the samples. The best trade-off was found at $\Delta = 3.9$ cm, where $AV^1 = 144$ (W/kg)/W; the overall efficiency was: m × AV^1 = Pa/P$_0$ = 0.88; and CV = 0.32. These values refer to the two samples together (3 ml + 3 ml). On the bottom layer of both samples CV = 0.30.

• Four dishes (Fig. 4.10b): In this case the symmetries of the previous case remain unchanged; however a higher AV^1 value occurs in the inner pair of samples, in comparison with the outer pair. By properly setting the two spacing parameters, Δ and δ (Fig. 4.10b), a ratio of 2 or 4 can be obtained between the inner and outer AV^1 values. In this way a simultaneous exposure at two given SAR levels can be carried out. Starting with the short circuit distance, which was found for the two-dish case ($|z| = 0.54 \lambda_z$), and following a rather large amount of numerical simulations, suitable spacings (Δ, δ) between the four samples were found as those giving the same, possibly low, nonuniformity degree CV for both pairs of samples (inner and outer), together with the given ratio (e.g. 2, or 4) between the AV^1 values (inner pair and outer pair). A final refinement of the distance $|z|$ from the short circuit termination was then accomplished by minimizing the overall CV. In particular, at a distance from the short circuit $|z| \approx 0.5$ λ_z ,for $\Delta = 1.9$ cm and $\delta = 2.3$ cm we obtained CV = 0.33 for both pairs, $AV^1 = 88$ (W/kg)/W in the inner pair, and $AV^1 = 22$ (W/kg)/W in the outer pair (ratio = 4); for $\Delta = 1.5$ cm and $\delta = 1.7$ cm we obtained CV = 0.33 for both pairs, $AV^1 = 65$ (W/kg)/W in the inner pair, and $AV^1 = 32$ (W/kg)/W in the outer pair (ratio = 2). Given the mass "m" of a single sample, the overall efficiency was: $2m \times$ inner$AV^1 + 2m \times$ outer$AV^1 = P_a/P_0$ (P_a/P_0=0.70 for a ratio of 4, P_a/P_0=0.60 for a ratio of 2).

	Sample alone	Sample + Dish+stand	Sample alone	Sample +Dish+stand
	AV^1 (W/kg)/W	AV^1 (W/kg)/W	CV	CV
Whole sample	274	260	0.31	0.32
bottom layer	234	222	0.29	0.30

TABLE 4. III. SHORT CIRCUIT TERMINATION, COMPARISON BETWEEN ONE SAMPLE ALONE AND SAMPLE +DISH+STAND

4.1.2 Experimental Dosimetry
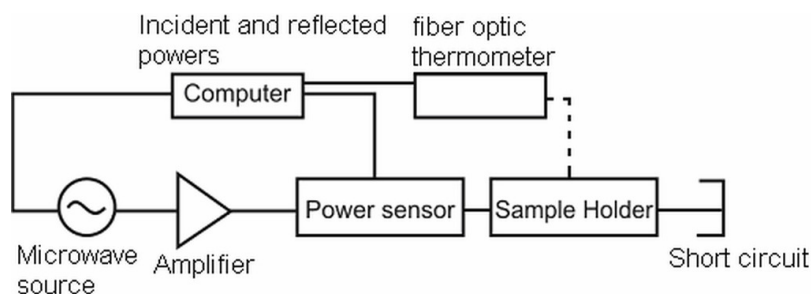
Fig. 4. 11. Diagram of exposure setup

In order to check the reliability of the calculated power deposition patterns (SAR_n) and nonuniformity degrees CV, local temperature measurements were carried out [16] by exposing one Petri dish under the SC/E_p exposure conditions. In Fig. 4.7 the contour plot of the SAR_n in the bottom layer of the sample is reported, but nearly the same pattern occurs in all sample layers, thus Fig. 4.7 served to ensure proper positioning of the temperature probes. Thermocouple probes (Physitemp Instruments, PT-6) kept perpendicular to the E field at all times, and fiber-optic temperature probes (FISO Technologies, FOT-M/2m), were inserted vertically at the maximum local SAR region (points A and C), and at the minimum local SAR site (point B). The diagram of the experimental setup is shown in Fig. 4.11: the microwave signal was amplified (Microwave Amplifiers LtdAM38A-092S-40-43) and was fed through a bidirectional power sensor (Rohde & Schwarz, NRT-Z43) into the exposure chamber. The power sensor and the thermometer were connected to a dedicated computer for measurements recording. In addition, a specific software was developed (using LabVIEW 7, National Instruments), to have both a user friendly system interface and a continuous monitoring of the power level which was adjusted according to the required SAR.
Simultaneous SAR evaluations at points A and C were carried out at average SAR levels of 5 and 10 W/kg, while simultaneous SAR

evaluations at points B and C were carried out at 150 W/kg average SAR. Temperature readings (taken every 4 s) were recorded and interpolated (Origin PRO 7.5). The local SAR values were calculated from the slope of the heating curves, T(t), at t = 0, as: $SAR = c\left.\dfrac{dT}{dt}\right|_{t=0}$

(c being the sample specific heat: c = 4186 J/kg °K). As already mentioned, an uncertainty for the SAR assessment of ± 20% was estimated, due to combined contributions of several parameters as calibration of the probe, determination of medium volume, probe positioning in Petri dish, assessment of the absorbed power. The results are summarized in Table 4.IV.

Average SAR (W/kg)	Local SAR at point A (W/kg)		Local SAR at point B (W/kg)		Local SAR at point C (W/kg)	
	calculated	measured	calculated	measured	calculated	measured
5	7.2	7.8			7.4	9.4
10	14.4	13.6			14.8	16.9
150			18.2	34.5	214	183

Table 4. IV. LOCAL SAR EVALUATIONS: MAXIMA (POINTS A AND C), MINIMUM (POINT B)

A very good agreement between calculated and measured local SAR values was found at point A (belonging to the annular maximum region) both at 5 and 10 W/kg average SAR. A fairly good agreement was also found at point C (again in the maximum region) even under 150 W/kg average SAR exposure conditions. At point B (minimum local SAR) temperature measurements gave a SAR value larger than the calculated minimum, but this result is not unexpected because of the highly peaked local SAR pattern [17]. In addition this deviation as well as that between point A and point B could be due to the difficulty of positioning the probe.

The calculated values of the overall efficiency Pa/P_0 (and of the average specific efficiency AV^1) were checked by measuring, over the band 1.5 GHz - 2.5 GHz, the amplitude of the reflection coefficient (the scattering parameter $|s_{11}|$) of the waveguide applicator loaded by

one, two, or four dishes, and the corresponding plastic stand. The measurements were performed by means of a microwave vector network analyzer (Anritsu 37247C). An uncertainty of ± 5% was estimated. As an example the case of two dishes is reported in Fig. 4.12, and a very good agreement is shown (the spikes in the experimental diagram are due to well known calibration artifacts [18]). Quite similar data were obtained in the case of one dish and four dishes. These results fully confirmed the adequacy of our calculation tool for overall efficiency evaluations.
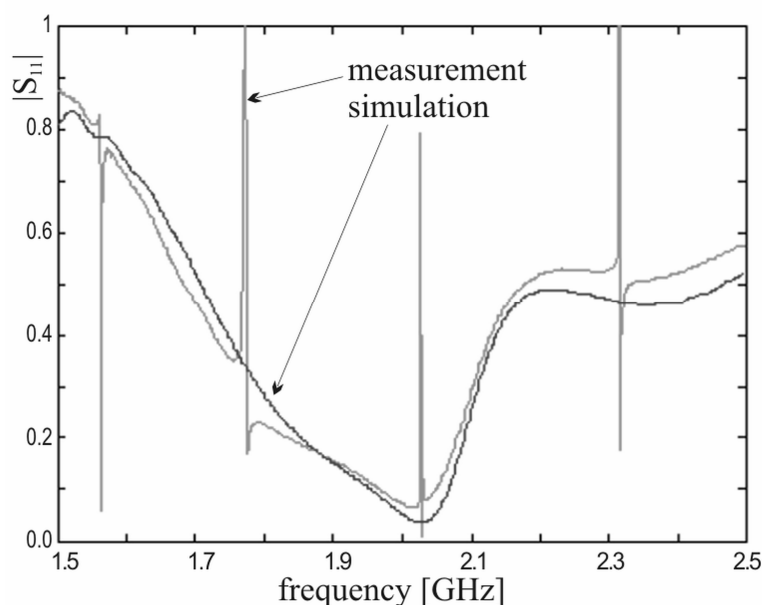
Fig. 4. 12. Measured and simulated s$_{11}$

4.2   Exposure results

In this paragraph the results of a coordinated bioelectromagnetic research project (WITHER: Wireless Technology Health Risks), funded by the Regione Campania, Italy, are reported. By means of the exposure system previously detailed described, the biological in vitro samples have been exposed and the biological endpoints have been analyzed by two different laboratories: the Bioelectromagnetism

Laboratory at IREA and the Biophysics Laboratory at DSF-UNINA. The main result expected is to obtain information on the possible role of UMTS exposure in carcinogenic processes.

4.2.1 Evaluation of cytotoxic and genotoxic effects in human peripheral blood leukocytes [19]

Venous blood samples were obtained from six healthy non smoker males aged between 27 and 32 years. They were included in the study on the bases of the answers of a questionnaire concerning alcohol consumption, present work, chemical and physical exposure at work place and during leisure time, medication, recent history of virus infection, vaccination, diagnostic X rays. All donors gave their informed consent.

$2x10^6$ leukocytes cells were seeded in 3 ml of RPMI 1640 medium, supplemented with 15 % heat-inactivated Foetal Calf Serum and 2 mM L-glutamine and transferred into 35 mm coded Petri dishes (Corning, cat. N. 430165). For each donor 5 conditions in duplicate were tested: RF exposure at SAR value of 0.5 and 2.0 W/kg, the corresponding sham-exposure and positive controls (cultures treated for 30 min with 50 µM hydrogen peroxide).

Radiofrequency exposure/sham exposure was carried out in waveguides hosted in a commercial incubator at 37°C in an atmosphere of 95% air and 5% CO_2; positive controls were left in an identical CO_2 incubator.

The experiments were carried out in blind: the operators involved in the culture, harvesting, preparation and examination of the microscope slides did not know the treatment conditions (RF-exposure/sham-exposure) of the cells. Data were decoded after all slides had been scored.

At the end of treatments cytotoxicity was estimated by trypan blue exclusion method and cell viability was calculated as a fraction of viable cells of the total cells, expressed as percentage.

After 24 h RF exposure, sham exposed and exposed cells showed similar percentage of viable cells. Neither 0.5 W/kg nor 2.0 W/kg SAR values affected viability of human leukocytes from six healthy

donors. Treatments with 50 µM hydrogen peroxide for 30 min, used as positive control for the evaluation of DNA damage, also did not affect cell viability. The percentage of viable cells never resulted lower than 95% for all the experimental conditions tested (P>0.05 in all cases).

To evaluate the induction of DNA damage in human leukocytes, the alkaline comet assay was applied and three parameters were considered: the percentage of DNA in the tail, the tail moment and the comet moment.

   After 24 h RF exposure no statistically significant differences were detected for both SARs tested in any of the parameters investigated, when sham-exposed samples were compared to exposed ones (P>0.05 in all cases). In contrast, when sham exposed cultures were compared to their positive controls (50 µM H_2O_2), a statistically significant increase in all the parameters investigated was detected, as expected.

4.2.2 Cooperative effects between X-rays and UMTS signal [20]

Peripheral blood lymphocytes were collected using buffy coats from four of the six volunteers previously described, in order to evaluate the cooperative effect of X-rays and microwaves.

Four different experiments were performed, one for each donor, according to the following scheme: eight dishes were inoculated with lymphocytes in each experiment; two dishes were given 4 Gy of X-rays and then immediately exposed to the RF signal (one dish for each SAR level); two dishes were also irradiated with 4 Gy of X-rays but then subjected to sham exposure. In addition, two sets of dishes, consisting of one dish per SAR value and respective sham exposure, were used to evaluate the genotoxicity exerted by the UMTS signal itself. Each of the eight 35-mm Petri dishes was seeded with $2x10^6$ cells, which were allowed to settle for 2 h before the experiment. The X-rays were produced by a Thomson tube (TR 300F; 250 kV$_p$, 0.8 Gy min^{-1}, STABILIPLAN machine, Siemens) and filtered by 1 mm-thick Cu foil. The irradiation room was adjacent to that hosting the RF generator and the thermostated incubator (37 °C, 5% CO_2). The dishes

were carefully placed inside the two waveguides and kept for 24 h in the presence or absence of the RF signal.

For each exposure condition, the weighted mean values with their relative standard errors were obtained. X-ray irradiated samples yielded a high incidence of aberrant cells (pooled mean values ≥ 70 %), and between 0.96 and 1.04 exchanges per cell were found from averaged measurements. This was expected having delivered a highly effective dose in order to assess significant variation in residual damage yields following RF treatment.

The fraction of aberrant cells yielded by exposure to RF signal alone was much lower than that found after X-rays. Analysis of pooled data showed no statistically relevant difference in the fraction of aberrant cells following either SAR value compared to the background incidence of cytogenetic damage in 0 SAR controls (z-test, $P > 0.20$), nor was a significant variation revealed by multiple comparison of all three exposure conditions together (ANOVA, $P = 0,967$). Similarly, RF signal did not significantly influence the frequency of aberration exchanges: exposure to 0.5 W/kg resulted in a practically identical incidence of aberrations per cell compared to 0 W/Kg SAR, while a lower but statistically irrelevant (t-test, $P = 0.394$; χ^2 test, $P = 0.466$) frequency was found following 2.0 W/kg compared to control. In all cases, the mean frequencies were below 0.006 exchanges per cell and did not show significant variations as assessed by multiple comparison (ANOVA, $P = 0.678$), confirming the results obtained by IREA group.

Comparison of the fraction of aberrant cells between irradiated samples (both X-rays and microwaves) and those exposed to X-rays alone indicated no variation as assessed by t-test ($P = 0.769$ for 0.5 W/kg and $P=0.817$, for 2.0 W/kg).

4.3   Design and characterization of an exposure system at 900 MHz

In the framework of a project on the evaluation of genotoxic and non genotoxic effects in mammalian cell cultures exposed to EMF at wireless frequencies, an exposure system has been designed and characterized. The followed approach in the development of this

system is the same described with full particulars in the above sections.

Even in this case it has been chosen a rectangular waveguide (SAIREM, 248 mm x 124 mm x 500 mm) in order to expose sample groups at the GSM signal (900MHz) at SAR levels of 1 W/kg and 0.2 W/kg (1h on - 1h off). In this case the biological requirement imposed a severe constraint about the volume of samples to be exposed. For biological reasons infact a large number of samples have to be exposed with a total volume multiple of 6 ml.

4.3.1 Numerical Dosimetry

As for the previous system, circular Petri dishes with 3 ml culture have been chosen, the sample is assumed to have perfectly cylindrical shape and the meniscus at the top of the sample has been not considered. The culture medium was RPMI with HEPES 25mM, L-Glutamin 1%, Penicillin-streptomycin 1%, Serum10% ($\rho = 1060 Kg / m^3$), whose complex relative permittivity ($\varepsilon' - j\varepsilon''$) was measured by wide-band measurements using a microwave vector network analyzer (Wiltron-Anritsu 37269B, Japan) and open ended coaxial probe technique [21, 22]. The measured values at 37°C were: $\varepsilon' = 70$ and $\varepsilon'' = 34$; being $\varepsilon'' = \sigma_{eq} / \omega \cdot \varepsilon_0$ the effective conductivity was $\sigma_{eq} = 1.7 S / m$.

Different configurations were tested in order to analyze all the possible cases; the best performance in terms of efficiency and nonuniformity degree resulted to be that with the waveguide terminated with a short-circuit plate and with the unperturbed E vector parallel to the sample layer (Ep case).

The case of waveguide loaded with six samples, each one of 3 ml cell culture (Figg. 4.13, 4.14), was first analyzed.

   The mesh dimensions of the computing grid outside the sample were: $\Delta x = \Delta y = \Delta z = 9.5 mm$, the wavelength in air being $\lambda_0 = 333 mm$; while inside the sample, the mesh dimensions were $\Delta x = \Delta z = \Delta y = 1 mm$, the wavelength in the culture being $\lambda = 38.7 mm$.
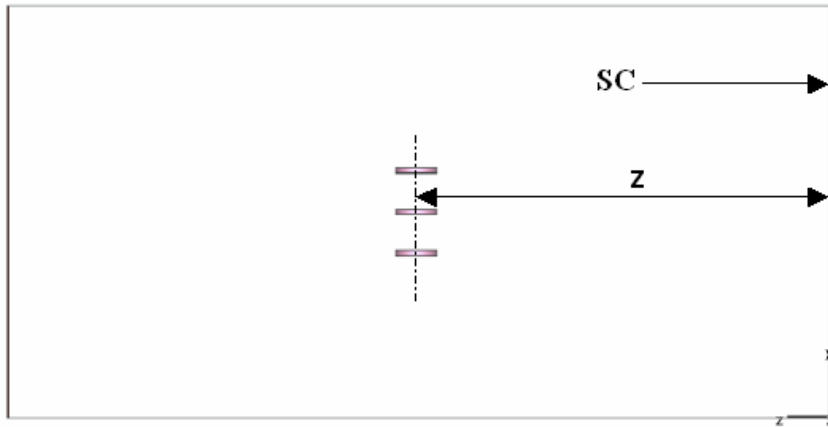
Fig. 4. 13. Waveguide longitudinal section.
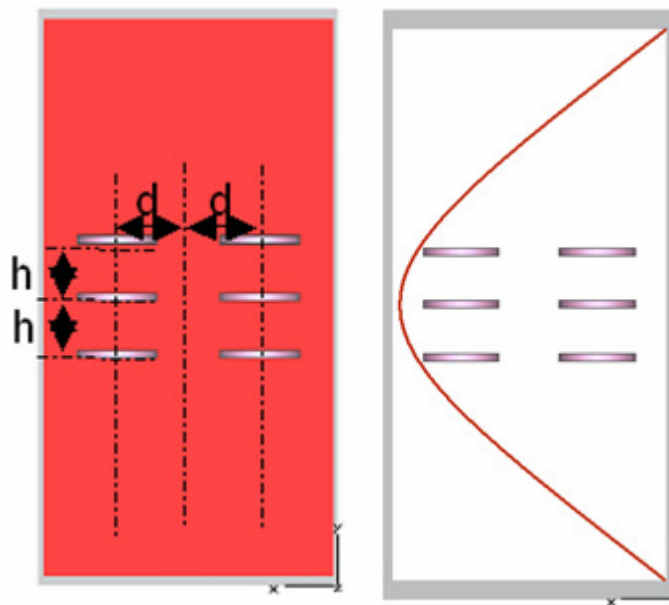
Fig. 4. 14. Six dish arrangements with respect to the unperturbed E field.

The six samples were positioned symmetrically with respect of the center of the transverse section of the WG ($x = \dfrac{b}{2} = 62mm$ e $y = \dfrac{a}{2} = 124mm$) and at a distance $z = 0.25\lambda_z$ from the SC

termination, corresponding in a point of maximum of the unperturbed E field. The choice of this first configuration is justified by the fact that with the sample perpendicular to the *xy* plane and with E vector parallel to the sample layer the specific efficiency increases because of the coupling mechanism between the field and the sample. In terms of nonuniformity this choice is confirmed by a layer by layer analysis (*xz* plane) carried out in order to obtain the distribution of the field inside the exposed sample; for the chosen polarization infact the field should present little variations passing from a layer to another, being quite tangential to them.

The distance along the x axis between the samples is denoted by **d** ($28mm \leq d \leq 32mm$) while **h** marks the distance along the y axis between the samples ($20.8mm \leq h \leq 25mm$) (Fig. 4.13b).

A reference value for **h** was first fixed and **d** was varied in order to obtain the best results, then, with the obtained value for **d, h** was varied. In this way it is found the condition for which there is the best trade-off between the efficiency and CV.

The best results are obtained for **d**=30 mm and **h**= 23 mm: CV=0.31 and η=0.08.

The dosimetric parameters were analyzed in each one of the six samples (Fig. 4.15) both for the bottom layer (b.l.) and the whole sample (w.s.); the results are summerized in Table 4.V.
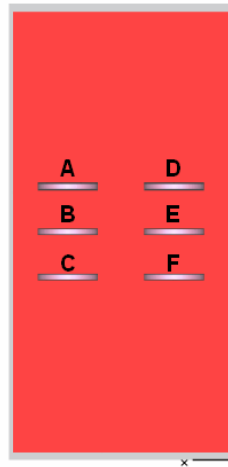
Fig. 4. 15

SAMPLE		CV	AV^1	η
A	b.l.	0.28	4.48	0.014
	w.s.	0.31	4.13	0.013
B	b.l.	0.29	4.33	0.014
	w.s.	0.31	4.27	0.014
C	b.l.	0.29	3.90	0.012
	w.s.	0.31	4.13	0.013
D	b.l.	0.28	4.48	0.014
	w.s.	0.31	4.131	0.013
E	b.l.	0.29	4.33	0.014
	w.s.	0.31	4.27	0.014
F	b.l.	0.29	3.90	0.012
	w.s.	0.31	4.13	0.013

Table 4. V. CV and AV^1 in the six Petri dishes.
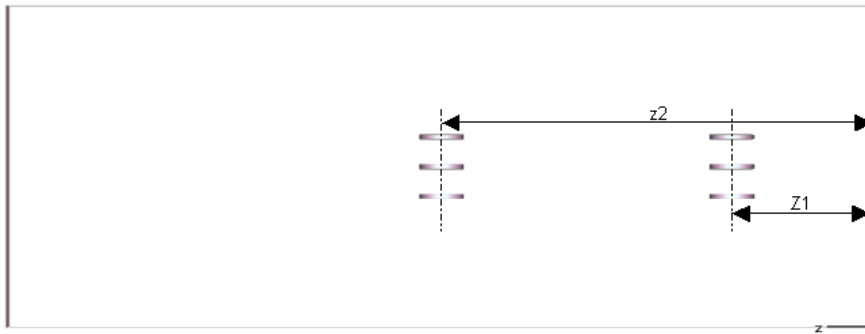
Fig. 4. 16. Sample positions along longitudinal section of the waveguide.

In order to increase the number of the samples, other six samples have been positioned at a distance $z_2 = \frac{3}{4}\lambda_z$ (Fig. 4.16), corresponding to the second maximum along the z axis of the unperturbed E field. In this way a configuration with 12 samples equivalent to 36 ml of exposed cell culture volume is obtained. Cause the sample could

perturb the field distribution in the WG, varying the E maxima points of the standing wave diagram, different positions, obtained moving around the two E field maxima the relative distance $|z_2-z_1|$ between the two pairs each one of six samples, were analyzed.

The best configuration was achieved with $z_1 = 110mm$ and $z_2 = 290mm$; in this way we obtain CV = 0.30 and η=0.19. The results for each sample (Fig. 4.17 - a, b) are summarized in table 4.VI.

a) Transverse section of the loaded WG for z= z_1	b) Transverse section of the loaded WG for z= z_2
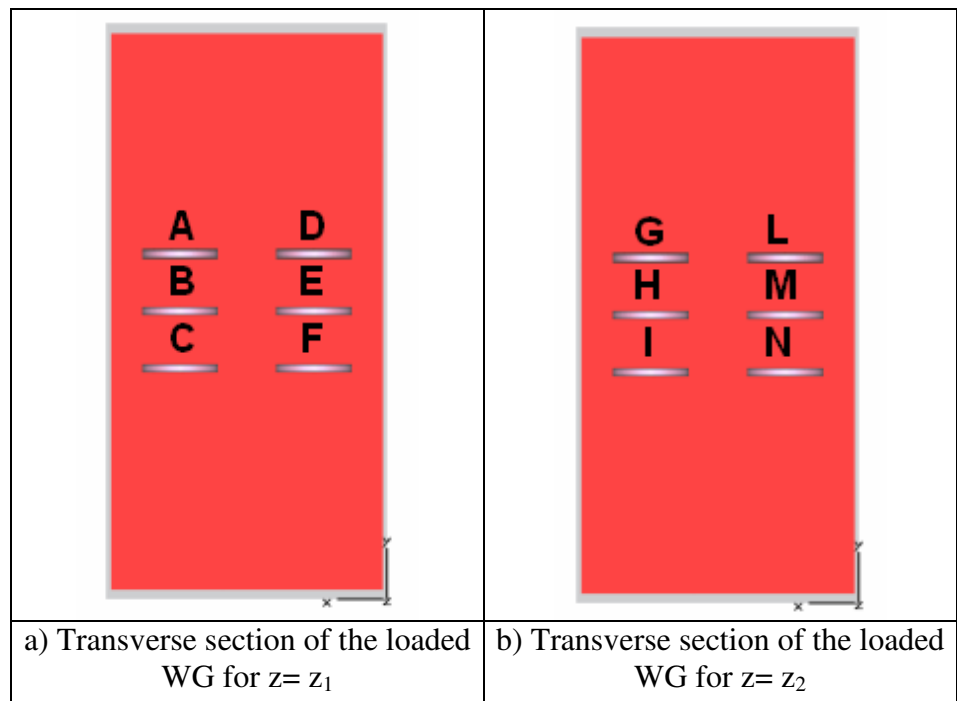
Fig. 4. 17

SAMPLE		CV	AV[1]	η
A	b.l.	0.28	5.45	0.017
	w.s.	0.29	4.98	0.016
B	b.l.	0.30	5.31	0.017
	w.s.	0.30	5.17	0.016
C	b.l.	0.29	4.76	0.015
	w.s.	0.29	4.98	0.016
D	b.l.	0.28	5.44	0.017
	w.s.	0.29	4.98	0.016
E	b.l.	0.30	5.31	0.017
	w.s.	0.29	5.17	0.016
F	b.l.	0.29	4.76	0.015
	w.s.	0.29	4.98	0.016
G	b.l.	0.28	5.44	0.017
	w.s.	0.30	4.98	0.016
H	b.l.	0.31	5.30	0.017
	w.s.	0.31	5.16	0.016
I	b.l.	0.31	4.76	0.015
	w.s.	0.31	4.97	0.016
L	b.l.	0.28	5.44	0.017
	w.s.	0.30	4.97	0.016
M	b.l.	0.31	5.30	0.017
	w.s.	0.31	5.16	0.016
N	b.l.	0.30	4.76	0.015
	w.s.	0.30	4.97	0.016

Table 4. VI. CV and AV[1] in the twelve Petri dishes.

The reported results refer to the WG loaded with sample alone. In the found better configuration a numerical dosimetry was carried out adding both the Petri dishes, which are made of polystyrene (ε' = 2.4, ε'' $\approx$ 0), and the plasting stands (3 mm thick), which are made of plexiglass ($\varepsilon_r = 2.6$, ε'' $\approx$ 0) (see Fig. 4.18).
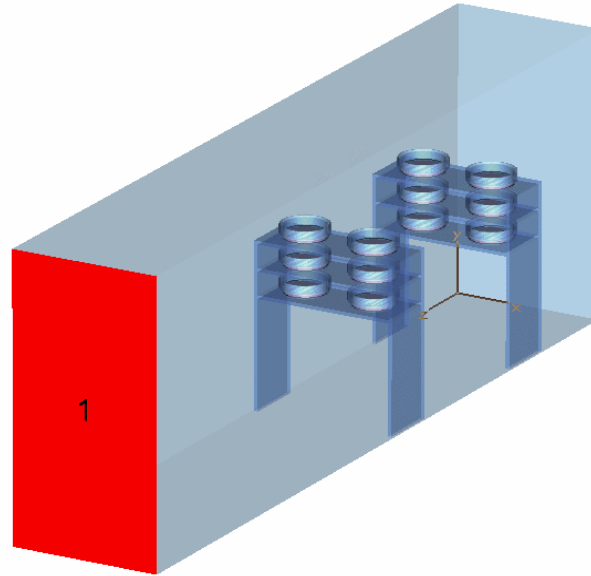
Fig. 4. 18. Twelve dish plastic stand.

In this case the computing grid was refined, adopting the Perfect Boundary Approssimation (PBA) mesh technique [23] and the Multilevel Subgridding Scheme (MSS) [24]. The mesh dimensions of the computing grid inside the sample were: $\Delta x = \Delta y = \Delta z = 0.25 mm$, thus, mesh dimensions were less than λ (or λ_0)/10. The final results are reported in table 4.VII.

SAMPLE		CV	AV[1]	η
A	b.l.	0.32	4.44	0.014
	w.s.	0.34	4.12	0.013
B	b.l.	0.31	4.75	0.015
	w.s.	0.34	4.59	0.015
C	b.l.	0.31	4.20	0.013
	w.s.	0.34	4.42	0.014
D	b.l.	0.30	4.63	0.015
	w.s.	0.34	4.13	0.013
E	b.l.	0.31	4.75	0.015
	w.s.	0.34	4.60	0.015

F	b.l.	0.31	4.21	0.013
	w.s.	0.34	4.43	0.014
G	b.l.	0.28	5.87	0.018
	w.s.	0.32	5.22	0.016
H	b.l.	0.29	6.00	0.019
	w.s.	0.32	5.82	0.018
I	b.l.	0.28	5.33	0.017
	w.s.	0.32	5.67	0.018
L	b.l.	0.28	5.88	0.018
	w.s.	0.32	5.23	0.017
M	b.l.	0.29	6.03	0.019
	w.s.	0.32	5.82	0.018
N	b.l.	0.28	5.34	0.017
	w.s.	0.32	5.62	0.018

Table 4. VII. CV and AV[1] in the twelve Petri dishes.

Fig. 4. 19. Contour plot of SARn in the bottom layer.
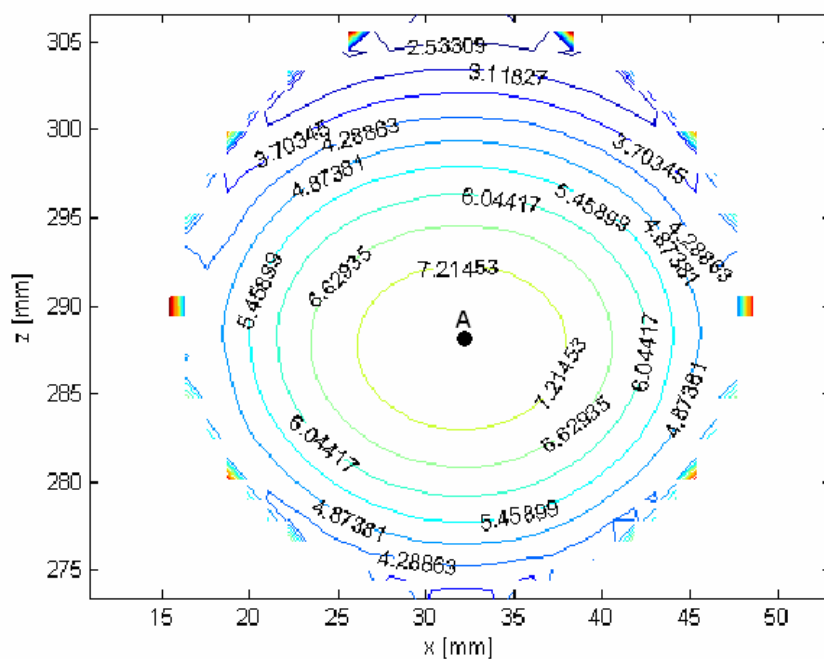
The obtained results are quite satisfactory. With this configuration infact it is possible to expose 12 Petri dishes filled each one of 3 ml sample with the same uniformity of the SAR distribution (Fig. 4.19) The total CV resulted to be 0.33 and the total efficiency η =0.20.

4.3.2 Experimental Dosimetry

In order to validate the numerical analysis local SAR measurements and efficiency measurements were carried out.
Fluoroptic probes (LUXTRON FOT LAB KIT) (Fig.4.20) were inserted vertically at the maximum local SAR region (point A of Fig. 4.19). SAR evaluations were carried out at average SAR levels of 11.0, 16.5 and 22.0 W/kg in the Petri dishes A, D, E and F (Fig. 4.17a), being the closest to the SC plate in which a little hole was performed in order to insert the probes. Temperature readings were recording with a sampling frequency of 4Hz and interpolated with Origin Pro 7.5. Even in this case, the local SAR values were calculated from the slope of the heating curves, T(t), at t = 0, as:

$$SAR = c \left. \frac{dT}{dt} \right|_{t=0}$$, c being the sample specific heat (c = 4186 J/kg °K).

Because back extrapolation of T(t) at t = 0 is not feasible, and in order to neglect errors due to heat diffusion or convection, the approach of Moros and Pickard [17] was used. The time window (t_m=30 s), over which temperature variation associated with SAR was measured,

satisfied the inequality $t_m \leq \dfrac{\alpha^2}{\pi^2 D}$ where α [m] is the half-width at half-

maximum of the SAR distribution ($\alpha = 0.007$ m) and D is the thermal diffusivity, $D=k/(\rho c)=1.4x10^{-7}$ $[m^2/s]$, k being the thermal conductivity.
A satisfactory agreement between calculated and measured local SAR values was found. As an example in table 4.VIII the results for the sample A are reported. Quite similar results have been obtained for samples D, E and F. An uncertainty for the SAR assessment of ±20% was estimated.
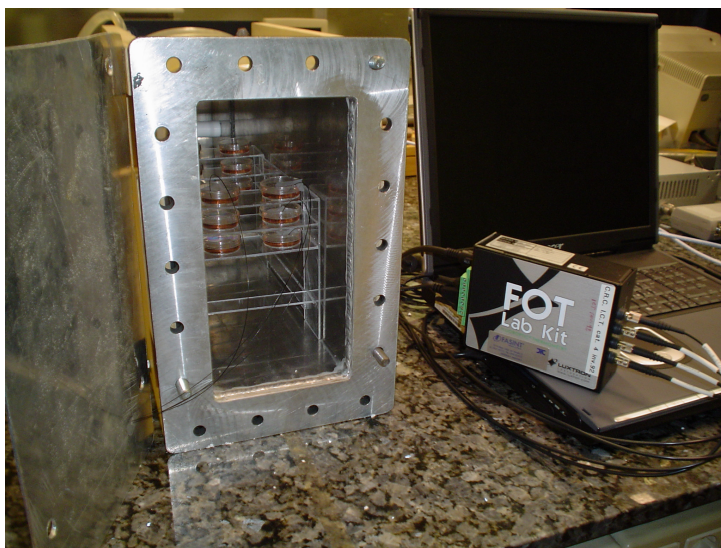
Fig. 4. 20

Average SAR (W/Kg)	Local SAR (W/Kg) calculated	Local SAR (W/kg) measured
11.0	17.3	16.6
16.5	25.7	22.7
22.0	34.0	36.7

Table 4. VIII. Comparison between calculated and measured Local SAR.

The calculated values of overall efficiency were checked by measuring, over the 700-1100 MHz band, the amplitude of the s_{11} parameter of the waveguide applicator loaded with the 12 samples. The results are shown in Fig. 4.21; a very good agreement between the calculated and measured data is obtained.

This system is actually at the Immunology Laboratory (University of Bologna) where biological evaluations are under test.
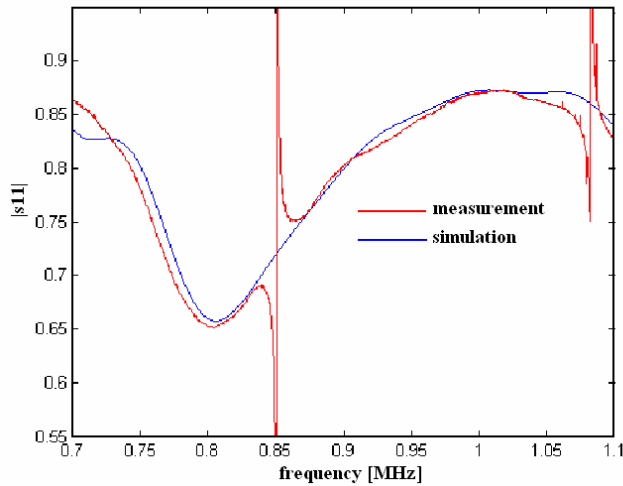
Fig. 4. 21. Measured and simulated |s11|.

4.4   Conclusions

In this chapter two exposure systems, opportunely designed for bioexperiments on the evaluation of possible genotoxic and non genotoxic effects induced by EMF at wireless frequencies (GSM and UMTS), are presented.

The applicator devices design is carried out by following the guidelines presented in chapter 3.

In the adopted approach [25, 26], AV^1 and CV were taken into account from the beginning of the design, by calculating them on the loaded applicator under different working conditions, and then defining the optimum configuration. Under these working conditions the exposed samples are strongly coupled to the incident field (high efficiency) while good uniformity is obtained by means of a careful "tuning" of the sample positioning. Temperature measurements in maximum SAR regions validated the calculated local SAR values, whose distribution gave the nonuniformity degree CV. Broad-band

measurements of the scattering parameters (the reflection coefficient s_{11}) demonstrated the full reliability of the numerical calculations of average SAR and overall efficiency.

A key feature of this two exposure devices is the strict unification of exposure conditions and dosimetry: in the planned experiments on different cancer-related endpoints, the biological samples are being exposed to the same modulated signal (GSM or UMTS) with the same average SAR and the same nonuniformity degree.

References

[1] M.L. Calabrese, G. Castello, G. d'Ambrosio, F. Izzo, G.F. Grossi, R. Massa, M. Napolitano, G. Petraglia, A. Sannino, M. Sarti, P. Scampoli, M.R. Scarfì, O. Zeni, "A project in the framework of the Campania EU-Region Center of Competence on Information and Communication Technologies, related to the evaluation of cancer related endpoints in mammalian cells following in vitro exposures to UMTS radiofrequency signal", 26th Annual Meeting of The Bioelectromagnetics Society, Washington, USA, June 2004, pp. 224.

[2] M.L. Calabrese, G. Castello, G. d'Ambrosio, F. .Izzo, G.F. Grossi, R. Massa, M. Napolitano, G. Petraglia, A. Sannino, M. Sarti, P. Scampoli, M.R. Scarfì, O. Zeni, "WITHER: Wireless Technology Health Risks, a Coordinated Bioelectromagnetic Research Project", IFMBE Proc. MEDICON and HEALTH TELEMATICS 2004, Island of Ischia, Naples, Italy, July 2004, ISSN 1680-0737, vol. 6, no. 56, pp. 221-224.

[3] M. Popovic, S.C. Hagness, A. Taflove, "Finite-difference time-domain analysis of a complete transverse electromagnetic cell loaded with liquid biological media in culture dishes", IEEE Trans. Biomedical Engineering, vol. 45, issue 8, pp. 1067-1076, Aug., 1998.

[4] W.F. Pickard, W.L. Straube, E.G. Moros, 'Experimental and numerical determination of SAR distributions within culture flasks in a dielectric loaded radial transmission line' , IEEE Trans. Biomedical Engineering, vol. 47, issue 2, pp. 202-208, Feb., 2000.

[5] L. Laval, Ph. Leveque, B. Jecko, "A new in vitro exposure device for the mobile frequency of 900 MHz", Bioelectromagnetics, vol. 21, issue 4, pp. 255-263, May, 2000.

[6] T. Iyama, H. Ebara, Y. Tarusawa, S. Uebayashi, M. Sekkijima, T. Nojima, J. Miyakoshi, "Large scale in vitro experiment system for 2 GHz exposure", Bioelectromagnetics, vol. 25, issue 8, pp. 599-606, Dec., 2004.

[7] F. Schönborn, K. Poković, A.M. Wobus, N. Kuster, "Design, optimization, realization and analysis of an in vitro setup for the exposure of embrional stem cells at 1.71 GHz", Bioelectromagnetics, vol. 21, issue 5, pp. 372-384, July, 2000.

[8] J. Schuderer, T. Samaras, W. Oesch, D. Spät, N. Kuster, "High Peak SAR Exposure Unit With Tight Exposure and Environmental Control for In Vitro Experiments at 1800 MHz", IEEE Trans. Microwave Theory and Tech., vol. 52, issue 8, pp. 2057-2066, Aug., 2004.

[9] F. Cocco , G. d'Ambrosio, G. De Prisco, R. Massa, "In vitro exposure systems at 900 MHz and 1.95 GHz. Numerical and experimental dosimetry, Proc. of "Biological Effects of EMFs, 2nd International Workshop", ISBN 960-86733-3-X, pp. 760-768, Rhodes, Greece, Oct., 2002.

[10] J. Shuderer, N. Kuster, "Effect of the meniscus at the solid/liquid interface on the SAR distribution in Petri dishes and flasks", Bioelectromagnetics, vol. 24, issue 2, pp. 103-108, Feb., 2003.

[11] F. Schönborn, K. Poković, M. Burkhardt, N. Kuster, "Basis for optimization of in vitro exposure apparatus for health hazard evaluations of mobile communications", Bioelectromagnetics, vol. 22, issue 8, pp. 547-559, Dec., 2001.

[12] A.M. Wobus, K. Guan, "Embrionic stem cell-derived cardiac differentiation: modulation of differentiation and 'loss-of-function' analysis in vitro", Trends in Cardiovascular Medicine, vol. 8, issue 2, pp. 64-74, Feb., 1998.

[13] T. Iyama, H. Ebara, Y. Tarusawa, S. Uebayashi, M. Sekkijima, T. Nojima, J. Miyakoshi, "Large scale in vitro experiment system for 2 GHz exposure", Bioelectromagnetics, vol. 25, issue 8, pp. 599-606, Dec., 2004.

[14] M. Burkhardt, K. Poković, M. Gnos, T. Schmid, N. Kuster, "Numerical and Experimental Dosimetry of Petri Dish Exposure Setups", Bioelectromagnetics, Vol. 17, pp. 483-493, 1996.

[15] David M. Pozar, "Microwave network analysis", Microwave Engineering, 1st ed., New York, USA: Addison-Wesley Publising Co. Inc., 1993, Chapter 5, pp. 220-230.

[16] J.W. Allis, C.F. Blackman, M.L. Fromme, S.G. Benane, "Measurement of microwave radiation absorbed by biological systems. Analysis of heating and cooling data", Radio Sci., vol. 12, issue 6(s), pp. 1-8, 1977.

[17] E.G. Moros and W.F. Pickard, "On the assumption of negligible heat diffusion during the thermal measurement of a nonuniform specific absorption rate", Radiation Research, vol. 152, issue 3, pages 312–20, Sep., 1999.

[18] Jyoti P. Mondal, Tzu-Hung Chen, "Propagation Constant Determination in Microwave Fixture De-embedding Procedure", IEEE Trans. Microwave Theory and Tech., vol. 36, issue 4, pp. 706-714, Apr., 1988.

[19] A. Sannino, M.L. Calabrese, G. d'Ambrosio, R. Massa, G. Petraglia, P. Mita, M. Sarti, M.R. Scarfì, "Evaluation of cytotoxic and genotoxic effects in human peripheral blood leukocytes following exposure to 1950 MHz modulated signal", IEEE Transactions on Plasma Science, vol. 34, no. 4, 1441-1448, 2006.

[20] L. Manti, M. L. Calabrese, R. Massa, M. Pugliese, P. Scampoli, G. Sicignano, G. Grossi, "Modulated microwave radiation at cellular–telephone frequency (1.95 GHz) does not enhance the yield of X ray-induced chromosome aberrations in human lymphocytes in vitro", submitted to Radiation Research.

[21] Anderson J.M., Sibbald C.L., Stuchly S.S., "Dielectric measurement using a rational function model", IEEE Trans. Microwave Theory Tech., vol. 42, no. 2, pp. 199-204, 1994.

[22] Bèrubè D., Ghannouchi F.M., Savard P., "A Comparative study of four ended coaxial probe models for permittivity measurement of lossy dielectric/biological materials at microwave frequencies", IEEE Trans Instrumentation and Measurement, vol. 44, no. 10, pp. 1928-1934, 1996.

[23] T. Weiland, "On numerical solution of Maxwell's equation and application in the field accelerator physics", Particle accelerators, vol. 15, issue 4, pp. 245-292, Jan., 1984.

[24] CST Microwave Studio 4, Reference Manual.

[25] M.L. Calabrese, G. d'Ambrosio, R. Massa, G. Petraglia, "In vitro dosimetry: a novel approach in the design of applicators for bioelectromagnetic experiments", Proc. 3rd Int. Workshop on Biological Effects of Electromagnetic Fields, Kos, Greece, 4 – 8 Oct. 2004, ISBN 960-233-151-8, pp. 18-21.

[26] M.L. Calabrese, G. d'Ambrosio, R. Massa, G. Petraglia, "A High-Efficiency Waveguide Applicator for In Vitro Exposure of Mammalian Cells at 1.95 GHz", IEEE Trans. Microwave Theory and Tchniques 54 (5): 2256-2264, 2006.

PART III

REMOTE CONTROL OF BIOLOGICAL NANOMACHINES

Chapter 5

Remote control of DNA hybridization through inductive coupling to an attached metal nanocrystal antenna

Major advances in molecular diagnostics, therapeutics, molecular biology, and bioengineering are expected to come from the integration of nanotechnology with biology and medicine. Significant progress was recently made in the development of functional nanoparticles, i.e. small atom clusters able to react to an applied external stimulus. These nanoparticles may be covalently linked to biological molecules such as peptides, proteins, and nucleic acids. Due to their size-dependent properties and dimensional similarities to biomacromolecules, nanoparticles offer exciting new opportunities for many biotechnological applications.

In this frame, the possibility of remotely inducing a defined effect on a nanoparticle by means of non-optical electromagnetic radiations appears particularly attractive, since the low transparency of most biological media (i.e. tissues, cell suspensions, whole body etc.) precludes the use of optical control.

The possibility that the electromagnetic (EM) field, in the microwave frequency range, can remotely control the biomolecular "machinery" in a specific and, in some cases, reversible manner has been recently reported [1].

In this chapter the experiment carried out by Hamad-Schifferli [1] will be presented and a critical study is carried out by analyzing the propagation of electromagnetic field into the helical coil applicator used in [1], both theoretically and numerically, in order to better understand the possible basic interaction mechanisms involved in this type of biological processes.

5.1 The Hamad-Schifferli experiment

In order to demonstrate reversible electronic control, the Hamad-Schifferli group has constructed a DNA hairpin-loop oligonucleotide covalently linked to a nanometre scale antenna. 38-nucleotide hairpin-loop DNA which is self-complementary at each end for 7 bases (Fig. 5.1) was covalently linked to a 1.4 nm gold nanocrystal by a primary amine appended to a single base. Because of the loop constraint, the DNA rehybridizes on a timescale comparable to dehybridization. A solution of the nanocrystal-linked oligonucleotides was exposed to a radio-frequency magnetic field (f = 1 GHz) pulsed at 15-s intervals and the possible dehybridization was monitored by the hyperchromicity of DNA, measured by optical absorbance at 260nm (A260).
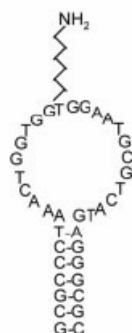
Fig. 5. 1

The exposures were carried out into an ultraviolet-visible spectrophotometer where A260 was monitored contemporary to the exposures. They used as exposure apparatus a coil with 35 turns and a cross section of about 1 cm^2. The turns were wrapped around a plastic cuvette/tube holder with open structures to maximize light passage. Currents with f = 1 GHz were obtained using an RF signal generator with an output of 1mW in conjunction with a linear amplifier. The

ultimate output power range used was 0.4-4W, though they estimated 10% input power to be transferred to coil due to losses from set-up architecture. DNA hairpin samples (volume 200μl) were in a 3 mm x 3 mm quartz cuvette inside the coil. The power used for the experiment results shown in Fig. 5.2 was 4W. As the RFMF was switched on, A260 increased from 0.22 to 0.25, indicating that DNA dehybridized with the RFMF (squares in Fig. 5.2). When the RFMF was switched off, A260 returned to its original value. Cycling through the on and off states was repeatable. The on/off ratio of A260 is 1.09, consistent with calculated absorption coefficients for this sequence hybridizing and dehybridizing 7 bases. Control solutions with DNA only (that is, not linked to gold nanocrystals) resulted in no change in the absorbance with RFMF (circles in Fig. 5.2). The authors assert that this effect shows that inductive coupling to a covalently bound metal nanocrystal can reversibly dehybridize DNA on a timescale of at most several seconds (Fig. 5.3).
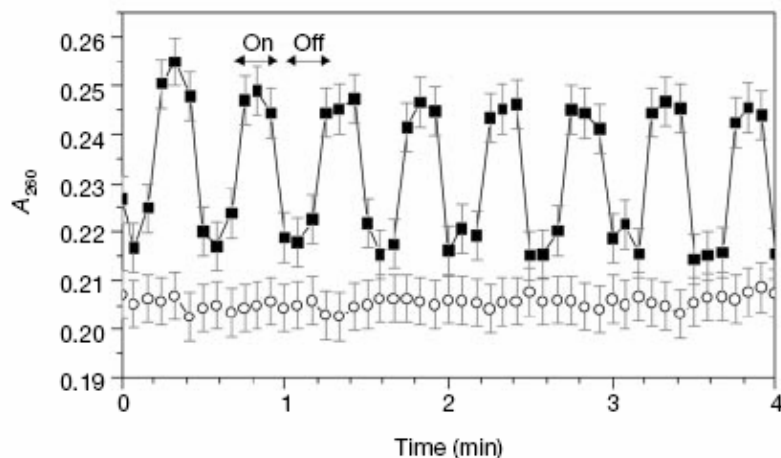
Fig. 5. 2
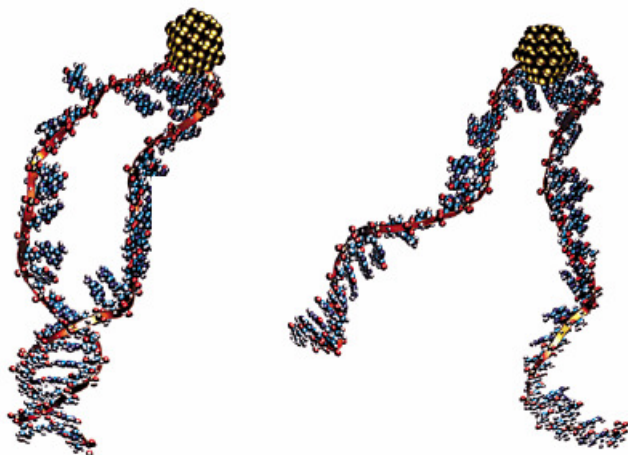
Fig. 5. 3. Hybridization and dehybridization of DNA.

5.2   Critical analysis of the Hamad-Schifferli study

The authors of the paper give an explanation of the observed phenomenon in terms of the inductive coupling to the nanocrystal covalently linked to the DNA, according to it heating the nanometal in an alternating magnetic field the eddy currents are produced and converted to heat by the Joule effect. In recent studies [2,3] this hypothesis has been confuted. The DNA molecules investigated by Hamad-Schifferli et al. are too large to exhibit selective intramolecular energy distribution through the particle-DNA bond, and the phosphine shell surrounding each particle would inhibit confounding chemical interactions between the DNA and the particle surface. In any case, the local induction heating of small Au nanoparticles is negligible for any physically reasonable values of applied field strength.

In addition, the description of the exposure apparatus reported in the paper is quite poor. The lack of an accurate description of the exposure set-up and, overall, of the electric and magnetic field distribution into the sample does not allow a deep understandament of the role played by electric and/or magnetic fields and, eventually, to replicate the described experiments.

A strong objection that it could be raised to Hamad-Schifferli et al. is the following: they have not taken in account the presence of the electric field inside the coil. By simply appliyng the Faraday's and Ampere's laws the dominant field component are achieved; in particular it is shown that both magnetic and electric fields are predominantly axial. The behaviour of induction coils is widely investigated for different purposes and a lot of studies are presented in literature [4, 5, 6]; in particular F. S. Chute and F. E. Vermeulen [7] stressed that the axial electric field component E_Z can be orders of magnitude larger than the electric field component E_Φ, further they pointed out that, in the frequency range under test, the axial electric field is radially, axially and circumferentially uniform throughout the interior of the coil.

By analyzing the simplest model of a helical structure, the field expressions are obtained and considering the geometrical characteristics of the coil used in [1] it turns out that along the z axis a strong electric field is present.

5.2.1 Theoretical analysis of the helical coil [5]

The so-called sheath helix is the simplest model of a helical coil applicator.

A uniform helix is described by its radius a and its pitch angle ψ ($\psi = \cot^{-1}(2\pi a / p)$), where p is turn-to-turn wire spacing). The wave equation is not separable in helical coordinates and there exists no rigorous solution of Maxwell's equations for the solenoidal helix. At radiofrequency a wire wound helix with many turns per free-space wavelength may be modelled as an idealized anisotropically conducting cylindrical surface that conducts only in the helical direction. The conductivity normal to the helical path is taken to be zero.
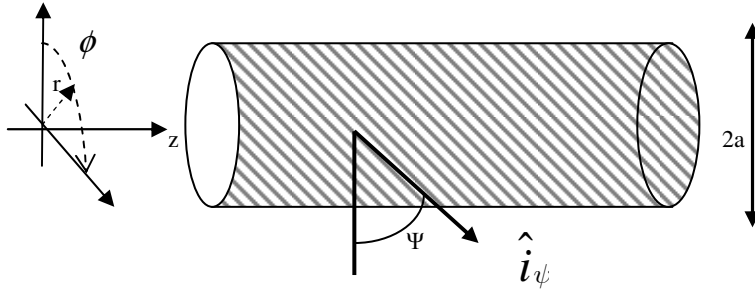
Fig. 5. 4

In this way the boundary conditions are not periodic and consist in imposing that the electric field component along the winding direction $\hat{i}_\psi$ is zero and that the electric and magnetic field components in the

direction orthogonal ($\hat{i}_\psi \ x \ \hat{i}_r$) to the winding are continuous for r=a.
In the following the two subscripts 1 and 2 refer to the field components in the two regions $r \leq a$ and $r \geq a$.
The fields solution for the helix consists of both E and H modes since these are coupled by the boundary conditions at r=a. In particular, it turns out:

$$E_{\phi 1}\cos(\psi) + E_{z1}\sin(\psi) = 0$$
$$E_{\phi 2}\cos(\psi) + E_{z2}\sin(\psi) = 0$$
$$E_{z1}\cos(\psi) - E_{\phi 1}\sin(\psi) = E_{z2}\cos(\psi) - E_{\phi 2}\sin(\psi)$$
$$H_{z1}\sin(\psi) + H_{\phi 1}\cos(\psi) = H_{z2}\sin(\psi) + H_{\phi 2}\sin(\psi) \ \text{ for } \ r = a$$

Expansions for the E and H modes in the two regions may be obtained in terms of the axial field components Ez and Hz.

$$\mathbf{E}_z = e_z(r,\phi)e^{-j\beta_z z}$$
$$\mathbf{H}_z = h_z(r,\phi)e^{-j\beta_z z}$$

The latter must be solutions of the following equation:

$$\nabla^2 f(r,\phi) + \left(k^2 - \beta_z^2\right) f(r,\phi) = 0 \; ;$$

applying the separation of variables procedure, given $h^2 = k^2 - \beta_z^2$, a generic solution has the form:

$$f(r,\varphi) = \left[A \cdot J_n(hr) + B \cdot Y_n(hr)\right]\left[C \cdot e^{-n\phi} + D \cdot e^{n\phi}\right]$$

where A, B, C, D, are unknown constants and $J_n(x)$ e $Y_n(x)$ are the Bessel functions of first and second type of order n with $n \in N$.
Let make some considerations on the Bessel functions. The equation
$$y'' + \frac{1}{r}y' + \left(k^2 - \frac{n^2}{r^2}\right)y = 0 \quad \text{admits two independent solutions } (J_n(x)$$
and $Y_n(x)$). For $kr>>1$ the following approximations are valid:

$$J_n(kr) \approx \sqrt{\frac{2}{\pi kr}} \cos\left(kr - \frac{\pi}{4} - \frac{n\pi}{2}\right)$$

$$Y_n(kr) \approx \sqrt{\frac{2}{\pi kr}} \sin\left(kr - \frac{\pi}{4} - \frac{n\pi}{2}\right)$$

When k^2 is negative the argument of the Bessel functions becomes imaginary. In this case, for convenience, the modified Bessel functions of first and second type are introduced, which are defined as follows:

$$I_n(hr) = j^{-n} J_n(jhr)$$

$$K_n(hr) = \frac{\pi}{2} j^{n+1}\left[J_n(jhr) + jY_n(jhr)\right]$$

For kr>>1 the following approximations are assumed:

$$I_n(hr) \approx \frac{e^{hr}}{\sqrt{2\pi hr}}$$

$$K_n(hr) \approx \sqrt{\frac{\pi}{2hr}} e^{-hr}$$

Since it is required a field that decays for large r, only the functions K_n are employed in the region r>a, while for r<a region only the I_n functions are used, approaching the K_n functions infinity in a logarithmic fashion for small values of the argument.

Thus, the longitudinal field components have the following form:

$$E_z = \begin{cases} e^{-j\beta z} \sum_n a_n I_n(hr) e^{-jn\phi} & \text{for } r \le a \\ e^{-j\beta z} \sum_n b_n K_n(hr) e^{-jn\phi} & \text{for } r \ge a \end{cases}$$

$$H_z = \begin{cases} e^{-j\beta z} \sum_n c_n I_n(hr) e^{-jn\phi} & \text{for } r \le a \\ e^{-j\beta z} \sum_n d_n K_n(hr) e^{-jn\phi} & \text{for } r \ge a \end{cases}$$

where $h = (\beta^2 - k^2)^{1/2}$ and a_n, b_n, c_n and d_n are unknown amplitude constants.

For this sheath-helix model it is possible to find a solution for a field that satisfies the boundary conditions for each integer n. The main interest here is for the solution $n=0$, which has circular symmetry.

In order to find the other field components inside and outside of the helix, one employs Ampere's law and Faraday's low to solve for E_r, E_ϕ, H_r, H_ϕ in terms of derivatives of E_z and H_z. Using the modified Bessel function derivative relations:

$$\frac{dI_0(hr)}{dr} = hI_1(hr) \quad \text{and} \quad \frac{dK_0(hr)}{dr} = -hK_1(hr)$$

The following expressions for the fields are found:

for $r < a$

$$E_z = a_0 I_0(hr)e^{-j\beta_z z}$$

$$E_r = a_0 \frac{j\beta}{h} I_0(hr)e^{-j\beta_z z}$$

$$E_\varphi = -\frac{j\omega\mu_0}{h} c_0 I_1(hr)e^{-j\beta_z z}$$

$$H_z = c_0 I_0(hr)e^{-j\beta_z z}$$

$$H_r = c_0 \frac{j\beta}{h} I_1(hr)e^{-j\beta_z z}$$

$$H_\varphi = -\frac{j\omega\mu_0}{h} a_0 I_1(hr)e^{-j\beta_z z}$$

for $r > a$

$$E_r = b_0 \frac{j\beta}{h} K_1(hr)e^{-j\beta_z z}$$

$$E_\varphi = -d_0 \frac{j\omega\mu_0}{h} K_1(hr)e^{-j\beta_z z}$$

$$E_z = b_0 K_0(hr)e^{-j\beta_z z}$$

$$H_r = -d_0 \frac{j\beta}{h} K_1(hr)e^{-j\beta_z z}$$

$$H_\varphi = -\frac{j\omega\varepsilon_0}{h} b_0 K_1(hr)e^{-j\beta_z z}$$

$$H_z = d_0 K_0(hr)e^{-j\beta_z z}$$

where a_0, b_0, c_0, d_0, are unknown constant to be determined by imposing the boundary conditions. The result is four homogeneous equations for the a_0, b_0, c_0, d_0 constants. A non trivial solution exists only if the determinant vanishes. Equating the determinant to zero results, after some algebra, in the eigenvalue equation for β, which is

$$\frac{K_1(ha)I_1(ha)}{K_0(ha)I_0(ha)} = (ha)^2 \frac{tg^2\psi}{(ka)^2}$$

This is a transcendental equation, from which it is possible to determine the h value. A solution for this equation is possible to find by a graphic way. In Fig. 5.5 both the right and the left members are plotted as a function of *ha* for different values of $G = \left(\frac{tg(\psi)}{ka}\right)^2 = \left(\frac{c}{2\pi fa} tg(\psi)\right)^2$ where *c* is the light velocity.
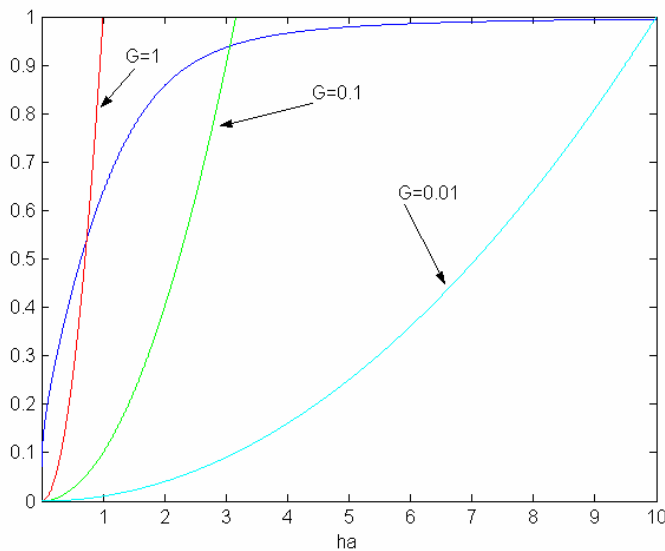
Fig. 5. 5

Once *ha* is calculated, it is possible to obtain from the boundary conditions three of the four unknown constants. The unknown constant is related to the source driving.
Using the geometric characteristics of the helical coil described in [1] it is found in this way a wavelength inside the coil of about 30 mm.

The sheath helix model resulted to be in a good agreement with the results obtained by the numerical analysis as described in the following paragraph.

5.2.2 Numerical analysis of the helical coil

The numerical analysis has been carried by superNEC 2.9, which is based on the moment methods. This numerical tool was previously successfully tested on a single turn, comparing the results with analytical ones and those of CST Microwave Studio 4.

A helical coil with 35 turns of copper wire (1 mm thickness), radius of 5.64mm (cross section of about 1 cm^2) and a pitch of 3 mm has been analyzed. The analysis is carried out in the frequency range 100 - 1500 MHz. The frequency 1040 MHz has been chosen in order to evaluate the electric and magnetic field, being the closer to a resonance in the neighborhood of 1 GHz.
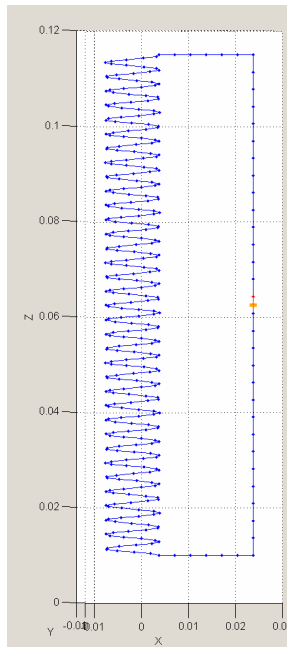
Fig. 5. 6

In the following figures the electric and magnetic field amplitude, being as usually the input power $P_0=1W$, on the plane passing in the centre of the turn are reported. It is evident a strong electric field along the z axis and a wavelength λ_z of about 30 mm, in agreement with the sheath helix model.
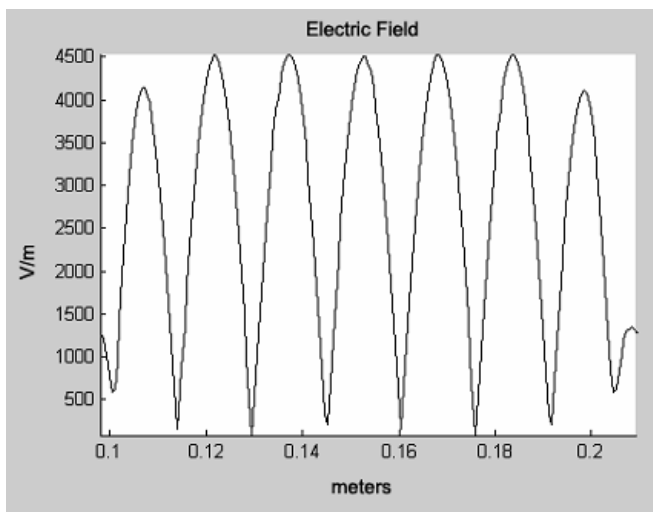
Fig. 5. 7. Electric field amplitute along z axis.
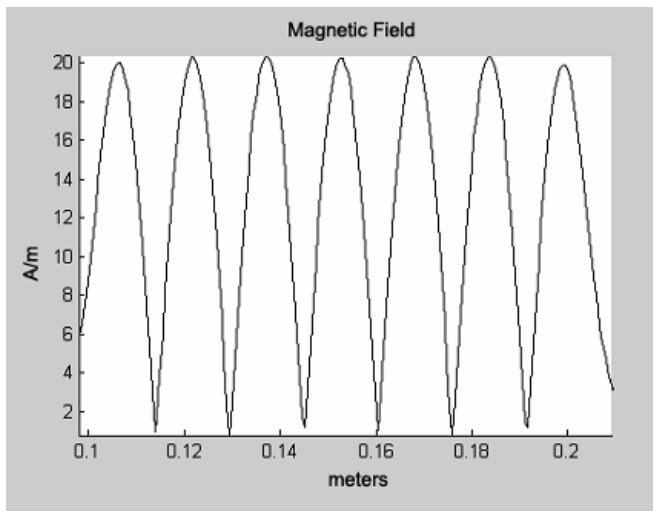
Fig. 5. 8. Magnetic field amplitute along z axis.

5.3   Conclusions

In this chapter a study on the remote control of DNA hybridization at 1 GHz is presented. The author observed the reversible hybridization of a DNA covalently linked to a gold nanocrystal of size 1.4 nm. According to their interpretation the observed effect is due to a local inductive heating of the nanocrystal, heating the nanometal in an alternating magnetic field the eddy currents are produced and converted to heat by the Joule effect.

The possibility of remotely control biological nanomachines by electromagnetic field seems to be very attractive and the experiment reported in [1] is very interesting. However the interpretation of the induced effect is not too much satisfactory. For this reason, in order to better understand the role of electric and magnetic field, a helical coil is analyzed both theoretically by the sheath helix model and numerically by Supernec 2.9.

The numerical analysis is carried out by performing helical structures similar to that reported in [1], as in the paper the description of the RF apparatus is quite lacking in details. The results confirmed the presence of a strong electric field inside the coil, in addition to the magnetic field.

References

[1] K. Hamad-Schifferli, J.J. Schwartz, A.T. Santos., S. Zhang, and J.M. Jacobson: "Remote electronic control of DNA hybridization through inductive coupling to an attached metal nanocrystal antenna". *Nature*, 415, 152-155, 2002.

[2] P. Keblinski, D.G. Cahill, A. Bodapati, C.R. Sullivan, T. A. Taton, "Limits of localized heating by electromagnetically excited nanoparticles", Journal of Applied Physics, vol. 100, 2006.

[3] Bellizzi G., Bucci O., Capozzoli A., "On the Energy Transfer between the Electromagnetic Field and Nanomachines for Biological Applications", Bioelectromagnetics. ISSN: 0197-8462. 2007, in press.

[4] S. Sensiper, " Electromagnetic Wave Propagation on Helical Structures (A Review and Survey of Recent Progress)", General Assembly Meeting of the International Scientific Radio Union (USRI), Aug. 23–Sept. 2, Tha Hague, Netherlands, 1954.

[5] K.L. Corum, J.F. Corum, RF Coils, Helical Resonators and Voltage Magnification by Coherent Spatial Modes", 5th International Conference on Telecommunications in Modern Satellite, Cable and Broadcasting Service, TELSIKS 2001, Vol. 1, 19-21, pp. 339-348.

[6] K.R. Minard, R.A.Wind, "Solenoidal Microcoil design. Part I: Optimizing RF homogeneity and coil dimensions", Concepts in Magnetic Resonance, 13, pp.128-142, 2001.

[7] F.S. Chute, F.E. Vermeulen, "A Visual Demonstration of the Electric Field of a Coil Carrying a Time-Varying Current", IEEE Trans. Education, vol. E-24, no. 4, pp. 278-283, 1981.

Chapter 6

Radiofrequency exposures of Nanoparticle/Biomolecule Conjugates

In this chapter an experimental study on the remote control of biological nanomachines by EMFs will be presented.

In order to better understand the interaction mechanisms between the exposed biological structures and EMF, two exposure systems has been designed and characterized:

1. a rectangular waveguide cavity, where the sample is positioned in contact with the walls, in order to minimize the influence of the electric field;
2. a helical coil applicator, similar to that used in [1]. In addition, the results of the radiofrequency exposures of nanoparticle/biomolecule conjugates will be presented.

The bio-sensor is made by a DNA duplex, complementary to a defined DNA target, which brings a metallic nanocrystal attached to one of the component strands. Following the hypothesis of Hamad-Schifferli [1], due to the magnetic field, upon radiofrequency excitation, the biosensor should be switched to its active state; when the radiofrequency excitation is stopped, the biosensor goes back to its original state.

6.1 Preliminary study on a radiofrequency controlled biosensor [2]

A first preliminary study was carried out in a rectangular waveguide cavity (72 mm x 33.8 mm x 340 mm), excited by a pulsed 2.45 GHz radiation (15s on – 15s off). The rectangular cavity was coupled to the coax-adapter waveguide by means of an inductive diaphragm and ended with a sliding short circuit (Fig. 6.1).

In order to expose samples with a minimum interaction with the electric field different configurations were numerically tested by using the commercial code CST-Microwave Studio 4. Following the approach widely described in the previous chapters, the best configuration resulted to be that with the sample (35 mm x 10 mm x 1 mm) in contact with the short circuit as reported in figg. 1, 2.


```
Layer type = Normal
Epsilon    = 76.783
Mue        = 1
El. cond.  = 1.278 [S/m]
```
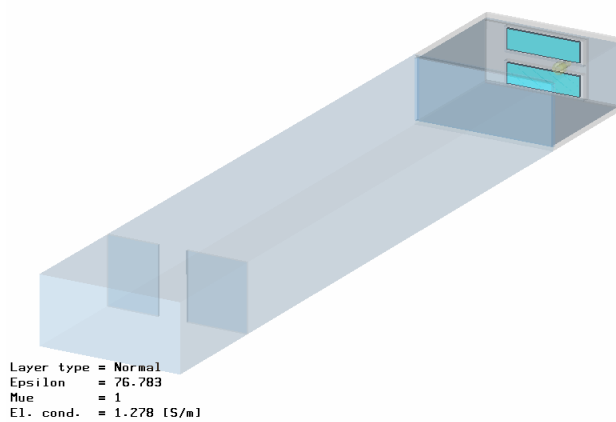
Fig. 6. 1
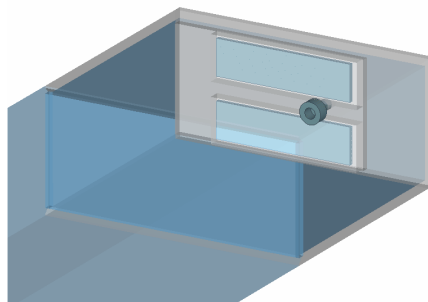
Fig. 6. 2

In the chosen configuration and with an input power $P_0=1W$ the average electric field amplitude inside the samples resulted to be 957

V/m, while the average magnetic field amplitude resulted to be 62.4 A/m (Fig. 6.3).
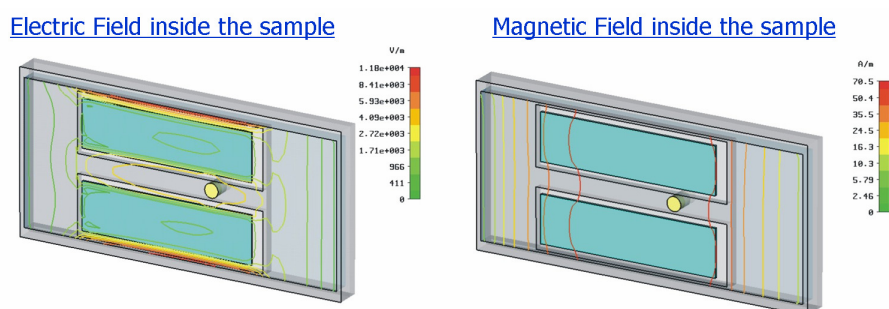
Fig. 6. 3

In these first experiments an irreversible effect, induced by the field on a DNA opportunely conjugate to a nanogold, was expected. In particular, the biosensor, consisting in two DNA strands of sequence T12 (strand A) and AT*A12 (strand B*, nanogold conjugated) respectively, was formed in solution as a duplex DNA (A/B*).

A sample of A/B* dissolved in bidistilled water was prepared in a quartz cuvette (HellMa, 0.1 cm) and supplemented with the strand B (without the nanogold), while the other optically coupled cuvette was filled of bidistilled water.

The experiments were carried out at three different incident powers: 0.5 W, 1 W, 2 W and the time exposure was 15 minutes, pulsed 15s on – 15s off. The temperature of the sample was measured during the exposures by means of a fiber optic thermometer.

The effect on of the DNA duplex (A/B*) induced by the magnetic field, should favourite the formation of a duplex A/B (without nanogold) which has an optical behaviour different from that of the A/B* complex.

The DNA sample was examined by Circular Dichroism (CD) before and after the RF exposure, to detect conformational changes induced on the DNA by the RF.
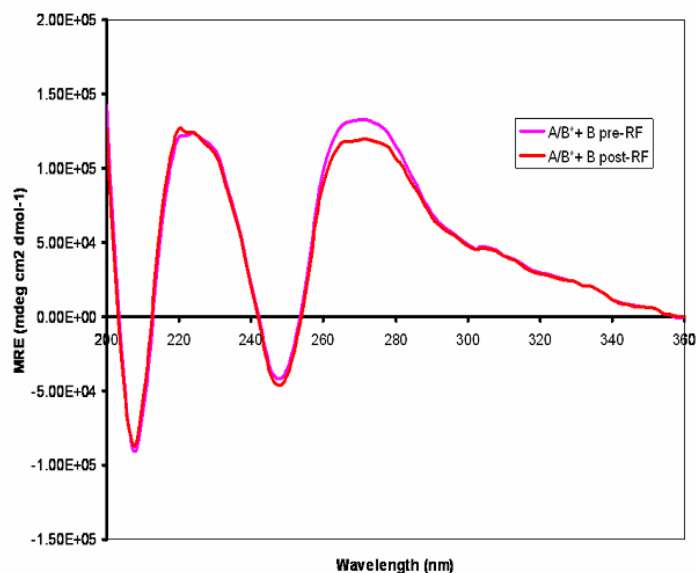
Fig. 6. 4

The results show a small but significant difference between the two spectra (Fig. 6.4) indicating a slight binding to the target DNA B by the sensor, which would be only possible if the RF are able to switch the sensor in its active state. The experiment reported here is only a first evidence that the designed biosensor might work. However, several aspects have to be improved; among them the most important one is, without doubt, the need of integrating directly into the exposure apparatus an optical detector and a thermal control.

6.2   Design of an helical coil applicator

The applicator proposed in [1] has been reconsidered and, following the "poor" description contained in the paper, it is tried to realize a similar applicator, adding a more accurate dosimetry in order to better understand the role of the EM parameters involved (frequency, intensity of the electric and magnetic field as well as their uniformity).

The device is integrated with an optical system, based on two fiber optics connected to a spectrophotometer, in order to measure the absorbance of the exposed solution during the RF irradiation. This measurement allowed following the conformational changes of solute molecules, induced by the EM field, during the exposure. A similar approach was followed in [1] too. However, the possibility of measuring the sample absorbance outside the spectrophotometer allowed a very careful control of the temperature of the sample that, as it is well known, it is a very critical point in order to assess "macroscopic" thermal effects of the EM field.

One of the goals of this research activity was to determine the field distribution into the sample in order to better understand the influence of electric and/or magnetic fields on the structure of an exposed molecule. To this end the numerical analysis and the experimental dosimetry validation were carried out.

A DNA hairpin, of the type used in [1], with or without a covalently-linked gold nanocrystal was used to study the effects of the RF exposure on the DNA structure. The bulk temperature effects on the optical properties of the hairpin alone or with the attached nanocrystal was fully evaluated by the CNR-IBB Laboratory (Naples), in parallel to RF measurements. This study allowed the prediction of the optical effects to be expected under RF exposition, if there were no other effects beside the heating of the solvent, and the comparison of the prediction with the experimentally measured effects.

6.2.1 The exposure setup

Helical coils have long been used in various ways as electromagnetic devices such as travelling-wave tubes, hyperthermia applicators, receivers in Nuclear Magnetic Resonance. Thus the analysis of the EM fields of a helically wound coil carrying a time-varying current is proposed in many studies [3, 4, 5, 6] where is pointed out that such coil produces time-varying axial and transverse electric fields. Numerical solutions [7], empirical relations and experimental characterizations [8] are reported to optimize these applicators in order to either maximize the ratio of axial to surface heating or to produce a transversely uniform electric field within cylindrical phantoms.

   The used approach was to replicate the coil described in [1], to numerically evaluate the electric and magnetic field into the same sample (same geometry and electromagnetic parameters) and to validate experimentally the numerical results.

   The coil used in [1] consisted of 35 turns with a cross section of ~1 cm^2 and with an open structure in the middle to maximize light passage. No pitch angle was reported.   The helical coil used for this study (Figg. 5, 6, 7) was constructed by 35 turns of copper wire (1 mm thick), the lengths of the helix and of the conductor were 111 mm and 1240 mm respectively, while the radius coil and the pitch angle were 5.64 mm and 4.8 degree respectively. The windings of the coil were fastened to a rigid Teflon cylinder in order to keep the geometric characteristics constant throughout the series of experiments. In particular, a central gap (5 mm) allowed to insert, perpendicularly to the axis coil, other two Teflon cylinders (Fig. 6.8) that facilitate accurate placement of the fiber optics connected to a spectrophotometer Lambda 25 (Perkin Helmer, Wellesley, USA) for absorbance measurements. As in [1] the coil was not provided of a balun and the sample, 200 μL of DNA solution, was contained in a 3 mm x 3 mm x 22 mm quartz cuvette (Hellma) axially inserted into the coil. The cuvette was placed on polystyrene foam (transparent to RF) and the center of the sample was coincident with that of the gap.

Fig. 6. 5. The helical coil applicator.

Fig. 6. 6. Side view of the applicator	**Fig. 6. 7. Top view of the applicator**
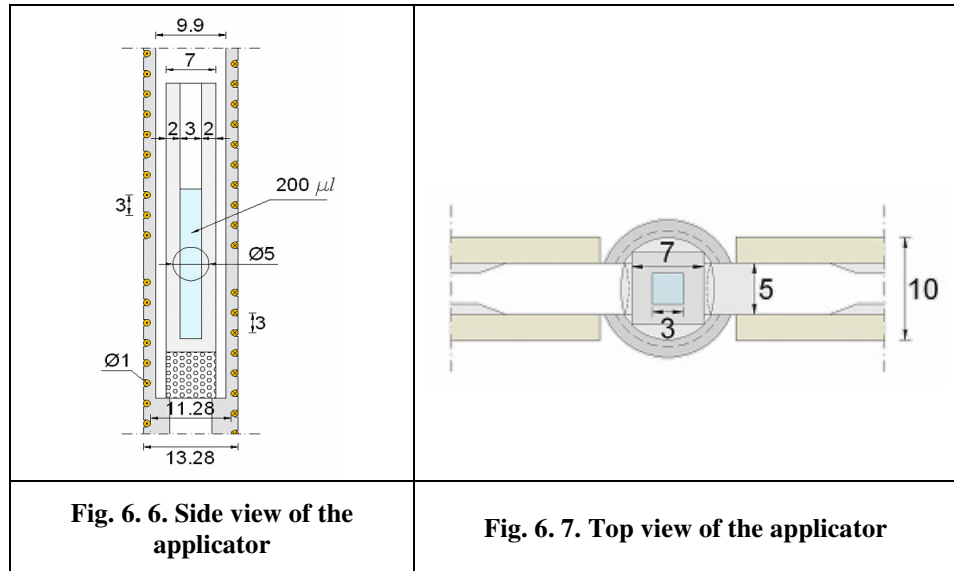
Fig. 6. 8. Fiber optic system.

The diagram of the experimental setup adopted for sample exposures

is shown in Fig. 6.9. The signal source was generated by an Agilent E4432B, ESG-D series signal generator (Palo Alto, USA). The microwave signal was amplified (Microwave Amplifiers LtdAM38A-092S-40-43, Nailsea, North Somerset, UK) and fed, through a bi-directional power sensor (Rohde & Schwarz, NRT-Z43, Munich, Germany) and a coaxial cable, into the the helical coil applicator. The power sensor was connected to a dedicated personal computer (PC), thus the incident power on the exposure coil (P_0) and the reflected power (P_r) were monitored and stored during the experiments.
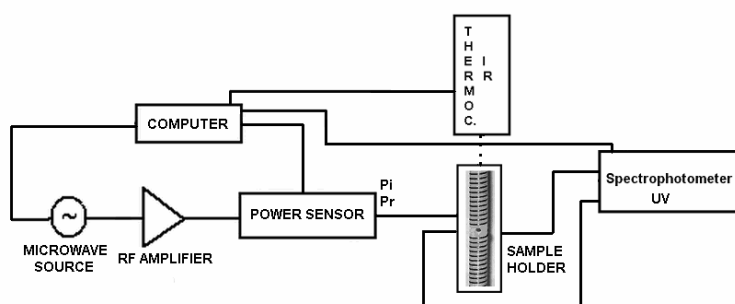
Fig. 6. 9. Exposure setup.

The system was also equipped with an UV spectrophotometer and a thermocamera, as described below.

6.2.1.1   Optical System

In order to evaluate conformational changes induced by the electromagnetic field on the DNA, a non perturbative fiber optic system, expressely made without any metallic connector, was realized (Fig. 6.8). In particular, terminal ends of the fiber optics were fastened in two Teflon cilinders which, in turn, were fixed in the two central holes of the coil support. In this way the focused optics were in contact with the sample, into the applicator, while the other ends were connected to a Lambda 25 spectrophotometer (Perkin Helmer, Wellesley, USA) so to perform absorbance measurements during the

exposure.

6.2.1.2   Thermal Control

In order to avoid sample contamination during thermal measurements, remote thermal device was used. A thermocamera (ThermoVision A40M, Flir System, North Billerica, Boston, USA) was placed 30 cm far away from the sample (Fig. 6.10) and temperature measurements were taken every 0.16 s, allowing to follow both the increase of temperature and the temperature distribution on the sample surface with an uncertainty of 2%. The thermocamera was connected to the PC, thus the temperature was continuously monitored and the data were stored during the exposures of DNA.
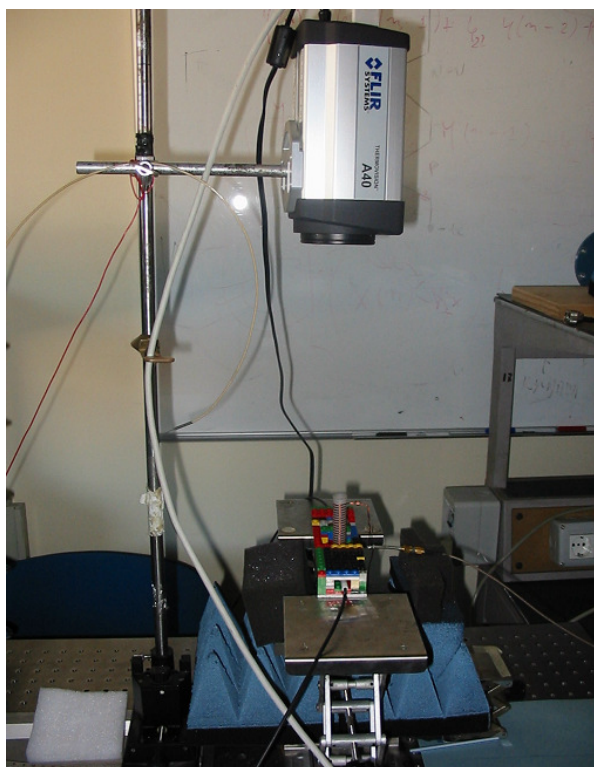
Fig. 6. 10. Thermal control setup.

6.3   Electromagnetic Dosimetry

The power deposition pattern inside the samples has been evaluated numerically by using a commercial code (Ansoft® HFSS v10, Pittsburgh, USA) based on the finite element method (FEM) [9]. Relative permittivity ε_r and effective conductivity σ_{eff} at 25°C of the samples were measured using a microwave vector network analyzer (Wiltron-Anritsu 37269B) and the open ended coaxial probe technique [10], [11], the density of the medium (ρ) was kept to 1000 kg/m^3. The helical coil is an open structure, thus the power absorbed by the sample (Pa) can not be derived by the simple knowledge (and measurement) of the input and reflected powers.

As operating experimental frequency was chosen 0.950 GHz, the nearest frequency to 1 GHz for which a local minimum of the reflection coefficient was found. In this way a maximum power transferred to the helical applicator, and as a consequence to the sample, occurs at a frequency very near to that used in [1].

In the numerical analysis the wire was considered to be a perfect electric conductor (p.e.c.) and the magnetic properties of the materials were taken as those of the free space ($\mu = \mu_0$).

The medium was either bidistilled water or 1 x PBS (1 x PBS = 1 mM KH_2PO_4, 10 mM Na_2HPO_4, 137 mM NaCl, 2.7 mM KCl) whose complex relative permittivity ($\varepsilon_r' - j\,\varepsilon_r''$) resulted to be, at room temperature, $\varepsilon_r' = 78$, $\varepsilon_r'' = 4$ and $\varepsilon_r' = 70$, $\varepsilon_r'' = 43$ ($\pm 5\%$) respectively, while the density was $\rho = 1000$ kg/m^3. Being $\omega = 2\pi \times 0.966 \times 10^9$ Hz; $\varepsilon_0 = 1 / (36\pi \times 10^9)$ F/m and $\varepsilon'' = \sigma_{eq}/\omega\varepsilon_0$, σ_{eq} resulted to be 0.2 S/m for water and 2.3 S/m for PBS. According to the FEM method, the region of interest was divided in tetrahedral elements (237740); the mesh generation (Fig. 6.11) was based both on the material wavelength ($\lambda_m = 35$ mm) refinement and on the length based mesh refinement; thus the length of the tetrahedral elements were refined until they were below a specified value. In this case we adopted as the maximum length of a tetrahedron (i.e. the length of its longest edge) $l = 2$mm, which is a value below $\lambda_m/10$.
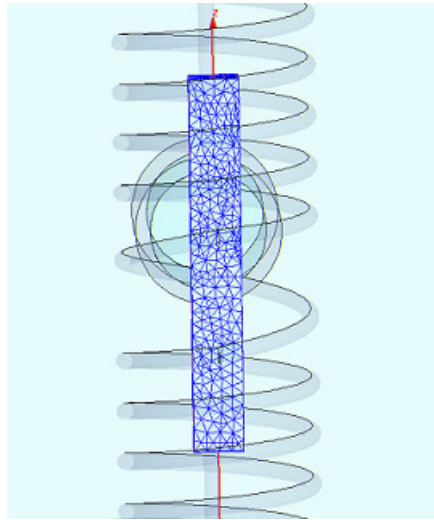
Fig. 6. 11. Mesh of the exposed sample.

In this configuration an average SAR (AV[1]) of 31.7 W/kg/W and a great non uniformity degree (Fig. 6.12) were obtained.
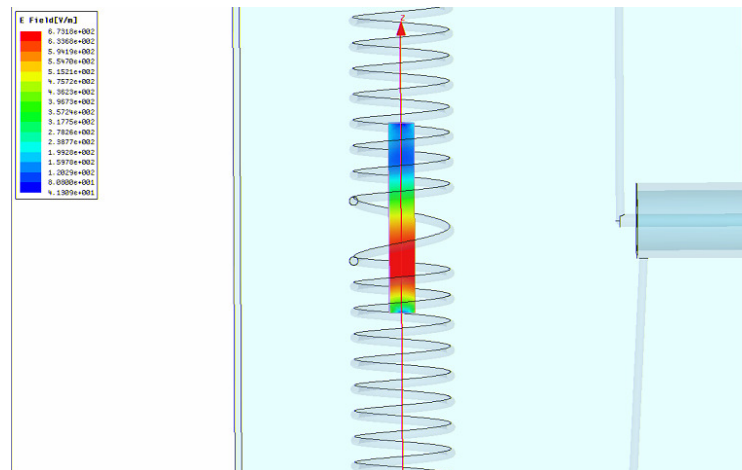

Fig. 6. 12. Electric field distribution into the sample.

In order to check the reliability of the calculated power deposition patterns (SARn) and nonuniformity degrees CV, local temperature

measurements were carried out [12] by means of a fluoroptic thermometer (Luxtron, FOT-M/2m, Santa Clara. California). A fiber-optic temperature probe was inserted vertically at the center of the sample and local SAR evaluations inside the sample (e.g. in the middle) were achieved. Temperature readings (taken every 0.25 s) were recorded and interpolated (Origin PRO 7.5). The local SAR values were calculated from the slope of the heating curves, as already described. For local SAR validation, measurements were carried out at 5 W incident power. An uncertainty for the SAR assessment of $\pm 20\%$ was estimated, due to combined contributions of several parameters as calibration of the probe, determination of medium volume, probe positioning, and assessment of the absorbed power.

The calculated SAR resulted to be for 1W input power SARc = 31.7 W/kg in good agreement with that measured SARm = 36.4W/kg, well in the uncertainty level.

The calculated values of the reflection coefficient amplitude (the scattering parameter s_{11}) and the resonance frequencies of the helical coil applicator, unloaded and loaded by the sample, were checked by measuring $|s_{11}|$ over the band (0.04 – 1.2) GHz by means of a microwave vector network analyzer (Anritsu 37247C), after a open-short-load (OSL) calibration [13]. An uncertainty of $\pm 5\%$ was estimated. Minima in reflection (resonances) are seen at several frequencies. In particular at 0.950 GHz the $|s_{11}|^2$ is 0.1, while at 1 GHz is 0.4 (Fig. 6.13). No influence of the external ambient was observed thus it was not necessary to shield the applicator. Resonance is not very sharp, thus the operating frequency is easily found if any mismatch, due to changes in position and/or dielectric properties of the sample, occurs.
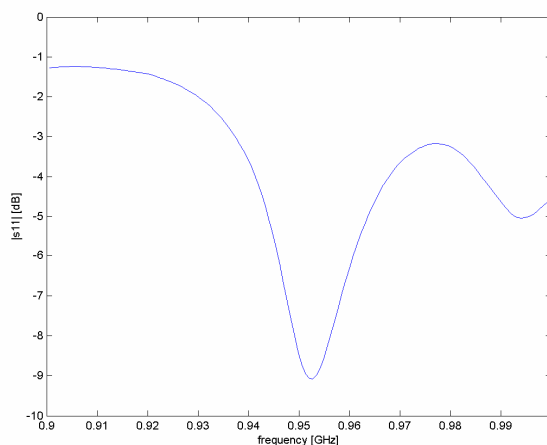
Fig. 6. 13. Measured |s11| values in frequency range 0.9 – 1 GHz.

6.4 Results of the RF exposures for the control of nanoparticle/biomolecule conjungates

All UV melting experiments were performed in the same buffer conditions used in [1] on a UV-Vis Jasco model V-550 spectrophotometer equipped with a Peltier ETC-505T temperature controller. Briefly, the absorbance of the unconjugated hairpin or of the nanogold-DNA conjugate was followed increasing the temperature from 20 to 80 C°, using a 1 mm quartz cuvette (Hellma) and a temperature ramp of 0.5 °C/min.
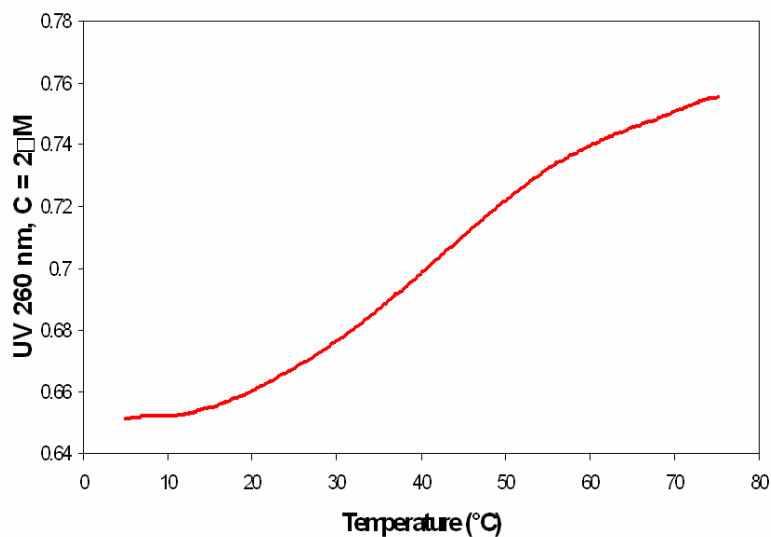
Fig. 6. 14. DNA melting curve.

In figure 14, the molar absorbance versus temperature of the hairpin DNA is reported. Interestingly, the nanogold conjugate has a molar absorbance which is not matched by the sum of the molar absorbance of the hairpin and of the nanogold. This means that the optical properties of the DNA change when the DNA is linked to the nanogold, as shown in Fig. 6.15.
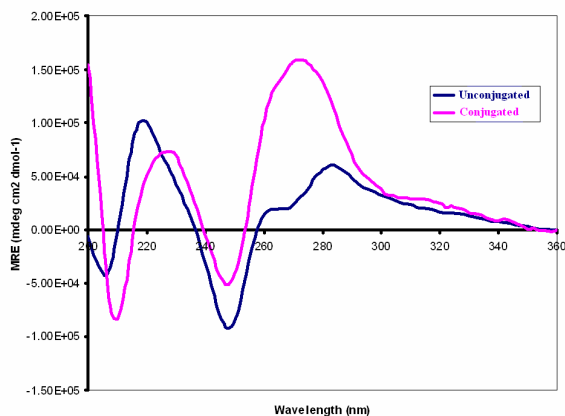
Fig. 6. 15. CD spectra of conjugated and unconjugated DNA

All together, these results indicate that it is not possible to predict the changes in the absorbance of the hairpin-nanogold conjugate on the basis of the melting behaviour of the hairpin alone, so that changes in the bulk temperature of the solvent may have different optical consequences on the hairpin alone in comparison to the conjugate.

With this fact in mind, it is not surprisingly that the solution heating, measured during the RF exposure as reported in Fig. 6.14 (2W, 15s ON, 15s OFF) produces different optical effects on the hairpin and on the nanogold-hairpin conjugate. The observed absorbance variation may be fully explained in terms of thermal effects on the hairpin or on the conjugate, providing that the molar absorbance at any temperature is known for the two forms.
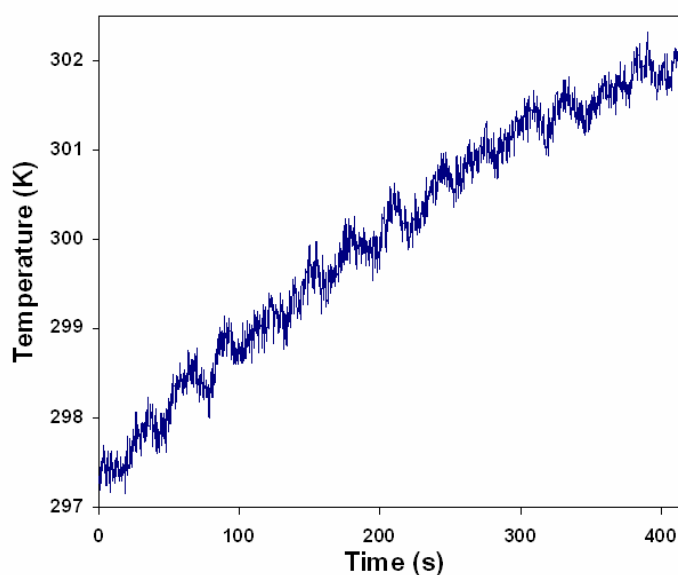
Fig. 6. 16. Temperature increase during the exposures.
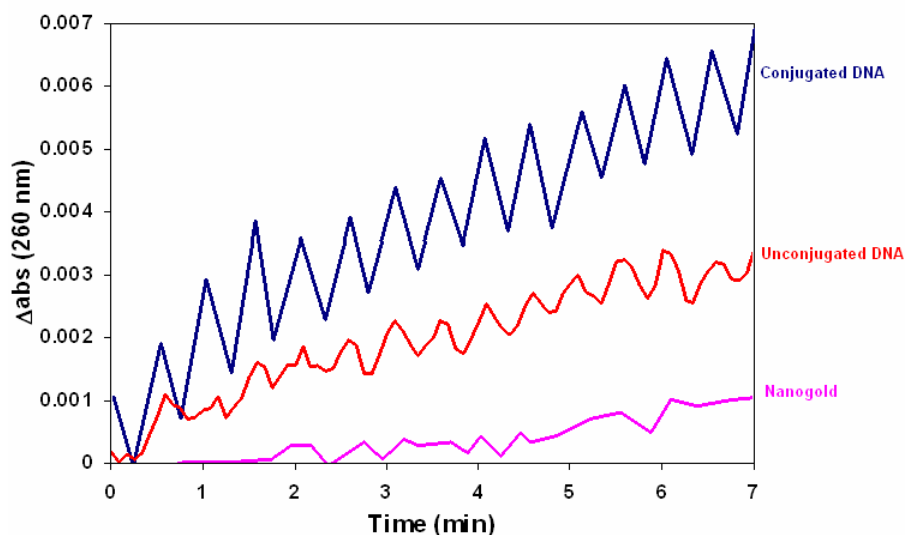
Fig. 6. 17. Time behavior of the conjugated and unconjugated DNA, and of nanogold solutions during the exposures.

A DNA double helix is an ideal candidate for discriminating bulk thermal effects from other effects upon RF exposure. This is mainly due to the very accurate description of the thermal effects on the double-helical status of DNA, which can be both theoretically predicted with a good approximation and experimentally measured with excellent accuracy (Fig. 6.18). In facts, the DNA double helix is an excellent reporter of the bulk heating of a solution, because, especially around the melting temperature of the DNA, even very tiny changes in the average temperature of the solvent cause large changes in the amount of double helix present in solution, which are in turn very easily observable thanks to the big changes they cause in U.V. absorbance of the solution at 260 nm.
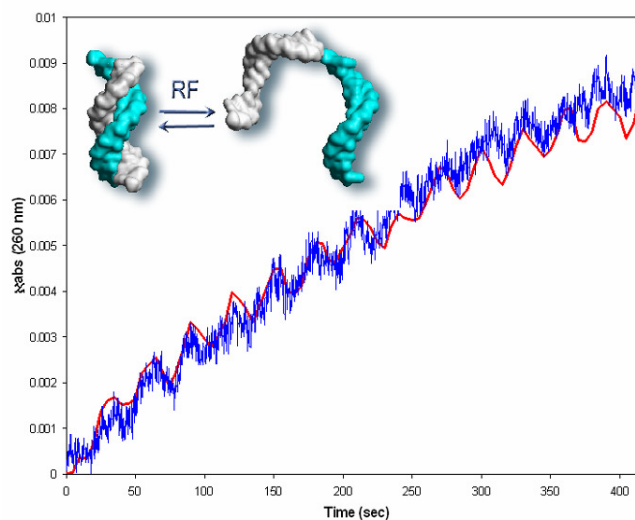
Fig. 6. 18

6.5   Conclusions

   In order to better understand the interactions mechanisms between
the EM fields and the structure of the biomolecules, an RF coil
applicator similar to that reported in [1] has been designed and
realized. Numerical and experimental dosimetry was carried out in
order to define the field distribution into the exposed sample. The
experimental analysis fully confirmed the adequacy of our calculation
tool for overall efficiency evaluations. Local SAR measurements
validated the calculated local SAR values, whose distribution gave the
nonuniformity degree CV. In addition the thermal control during the
RF exposures enabled to reconstruct the experiment.
Using this apparatus, the nanogold-DNA hairpin described by H.S. in
[1] was studied. After a proper optical characterization of the system,
it turns that the DNA denaturation under RF exposure is probably
caused by bulk heating of the solution, and the differences between
the conjugated and unconjugated U.V. behaviour are reduced to the
intrinsic different molar absorbance of the conjugated form with
respect to the hairpin alone.

References

[1] K. Hamad-Schifferli, J.J. Schwartz, A.T. Santos., S. Zhang, and J.M. Jacobson: "Remote electronic control of DNA hybridization through inductive coupling to an attached metal nanocrystal antenna". *Nature*, 415, 152-155, 2002.

[2] Bucci E.M., Bucci O.M., Calabrese M.L., d'Ambrosio G., Massa R., Messere A., Milano G., Musumeci D., Petraglia G., Roviello G., "Preliminary Report on a Radiofrequency Controlled Biosensor", BEMS 28th Annual Meeting, June 19-24, 2005, Dublin, Ireland.

[3] S. Sensiper, " Electromagnetic Wave Propagation on Helical Structures (A Review and Survey of Recent Progress)", General Assembly Meeting of the International Scientific Radio Union (USRI), Aug. 23–Sept. 2, Tha Hague, Netherlands, 1954.

[4] K.L. Corum, J.F. Corum, RF Coils, Helical Resonators and Voltage Magnification by Coherent Spatial Modes", 5th International Conference on Telecommunications in Modern Satellite, Cable and Broadcasting Service, TELSIKS 2001, Vol. 1, 19-21, pp. 339-348.

[5] K.R. Minard, R.A.Wind, "Solenoidal Microcoil design. Part I: Optimizing RF homogeneity and coil dimensions", Concepts in Magnetic Resonance, 13, pp.128-142, 2001.

[6] F.S. Chute, F.E. Vermeulen, "A Visual Demonstration of the Electric Field of a Coil Carrying a Time-Varying Current", IEEE Trans. Education, vol. E-24, no. 4, pp. 278-283, 1981.

[7] P.S. Ruggera, G. Kantor, "Development of a Family of RF Helical Coil Applicators which produce Transversely Uniform Axially Distributed Heating in Cylindrical Fat-Muscle Phantoms", IEEE Trans. Biomedical Engineering, vol. BME-31, no. 1, pp. 98-106, Jan. 1984.

[8] J. Guerquin-Kern, M.J: Hagmann, R.L. Levin, "Experimental Characterization of Helical Coils as Hyperthermia Applicators", IEEE Trans. Biomedical Engineering, vol. 35, no. 1, pp. 46-52, Jan. 1988.

[9] Jianming Jin, "RF Fields in Biological Objects", Electromagnetic Analysis and Design in Magnetic Resonance

Imaging, CRC Press LLC, Florida, USA, 1999, Chapter 5, pp. 224-226.

[10] J.M. Anderson, C.L. Sibbald, S.S. Stuchly, "Dielectric measurement using a rational function model", IEEE Trans Microwave Theory and Techniques, vol. 42,no. 2, pp. 199-204, 1994.

[11] D. Bèrubè, F.M. Ghannouchi, P. Savard, "A Comparative study of four ended coaxial probe models for permittivity measurement of lossy dielectric/biological materials at microwave frequencies", IEEE Trans Instrumentation and Measurement vol. 44, no. 10, pp. 1928-1934, 1996.

[12] J.W. Allis, C.F. Blackman, M.L. Fromme, S.G. Benane, "Measurement of microwave radiation absorbed by biological systems. Analysis of heating and cooling data", Radio Sci., vol. 12, issue 6(s), pp. 1-8, 1977.

[13] R.L. Vaitkus, "Wide-band de-embedding with a short, an open, and a through line", Proceedings of IEEE, vol. 74, no. 1, pp. 71-74, Jan. 1986.

PART IV

DESIGN AND CHARACTERIZATION OF A MAGNETIC FIELD EXPOSURE SYSTEM

Chapter 7

Design and characterization of a magnetic field exposure system

One of the main crucial aspects emerging from the preliminary studies on the remote control of biological machine by EMFs is the need of realizing exposure systems opportunely designed.

In this chapter the design of a magnetic field applicator will be described. The design is subdivided in three main steps: 1) development of a theoretical model; 2) numerical analysis of the proposed model; 3) realization and characterization of the apparatus.

The followed approach in the development of the theoretical model of the magnetic field applicator is based on the study of Chodorow and Chu [1], applied for a different application. The starting point is based on the following concept. The structure under test consists of two tape helices wound in opposite directions. This structure has two modes (the symmetric and anti symmetric modes), which can be considered as arising from the combining of the single helix modes of the two helices with different phases. In one case the two modes are superimposed in phase and in the other out of phase. In [1] the symmetric mode superposition case is investigated, since they are interested in a strong axial electric field. In the present work the opposite case is examined, since the interest is for the minimization of the electric field with respect to the magnetic field.

7.1   A theoretical model for the applicator

The helix electrical performance can be analyzed using two different approximations: the sheath model and the tape model. In the sheath model the helix is approximated by a helically conducting cylindrical surface of negligible thickness. In the tape model the helix is represented by a tape wound over a cylinder whose radius is made equal to the actual helix mean radius. The tape model gives a more accurate evaluation of helix electrical parameters because it accounts for space harmonics, while they are not considered in the simpler sheath helix model.

The case of a single tape model was investigated for the first time with full details by Sensiper [2], in the following years other researchers [1, 3, 4] studied the tape helix model for high-performance helix traveling wave tube. In particular Chodorow [1] studied the cross wound twin helices, which are characterized by the so-called symmetric and antisymmetric modes: for their purposes they analyzed the symmetric mode. In this context, instead, since the objective is to achieve a strong axial magnetic field with respect to the electric one, the antisymmetric mode is analyzed.

Let start to consider the case of the simple superposition of the fields of the two separate helices. If one superimpose the fields in such phase that the axial magnetic fields of the fundamental component add, one finds that E_z of the fundamental component is identically zero. For the single helix using the sheath model, it turns out that roughly half of the energy storage is associated with H_z (the longitudinal component of magnetic field, and with the TE portion of the EMF. However for the sheath model, one must necessarily have both the TM portion and the TE portion present in order to satisfy the boundary conditions. For a single tape helix for which space–harmonic components are not negligible, it still turns out that in the fundamental component one has a roughly equal amount of TM and TE energy storage. For the twin tape, from superposition, it becomes necessary for the space harmonics to carry principally electric energy, since there is no TM portion in the fundamental component. This is a symmetry property which is considered in the following more exact

analysis in which the interactions between the two helices is taken into account.
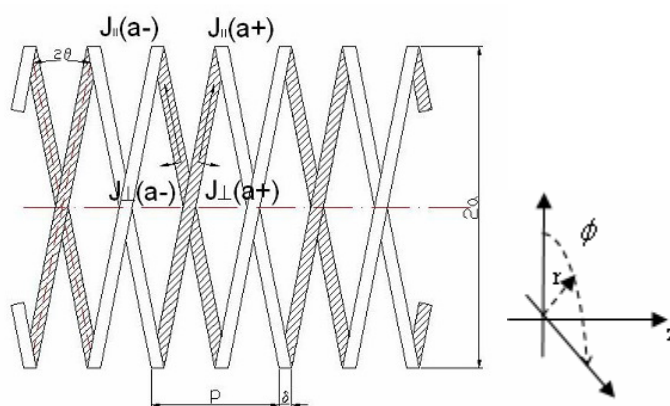

Fig. 7. 1

Nomenclature
a   helix radius;
p   pitch (distance between two turns of a single winding);
δ   width of the helix tape in the axial direction;

$$\cot \theta = \frac{2\pi a}{p};$$

$$\eta = \frac{2\pi \delta}{p};$$

$J_{\parallel}(a^{-})$, $J_{\parallel}(a^{+})$ are the parallel components of current densities on helix tapes;

$J_{\perp}(a^{-})$, $J_{\perp}(a^{+})$ are the perpendicular components of current densities on helix tapes.

The mathematical problem
The twin helix structure is shown in Fig. 7.1.
Assumptions:
1) the helices are assumed to be infinitely long;
2) the helices have equal radii;
3) the helices are wound with an infinitely thin tape;
4) the tape is a perfect electric conductor.

The mathematical problem is to solve Maxwell's equations under appropriate boundary conditions. It is considered a source-free problem.
Boundary conditions:
1) $\underline{n} \times \underline{E}$ continuous everywhere on the cylindrical surface $r = a$;
2) $\underline{n} \times \underline{E} = 0$ on helices;
3) $\underline{n} \times \nabla \times \underline{E}$ continuous on $r = a$ except on helices.

Simmetry properties of the structure
The domain of the helix tape is defined as

$$-\frac{\eta}{2} \leq \left(\phi \mp \frac{2\pi z}{p} \right) \leq \frac{\eta}{2} \text{ with } \eta = \frac{\delta}{a} \tan \theta.$$

The minus sign is used for the right –handed helix, the plus sign for the left-handed helix.
The structure has several degrees of symmetry.
The structure remains unchanged under any one or any combination of the following transformations:
a) $(r, \phi, z) \rightarrow (r, \phi, -z)$
b) $(r, \phi, z) \rightarrow (r, \phi, z \pm p)$
c) $(r, \phi, z) \rightarrow (r, -\phi, z)$
d) $(r, \phi, z) \rightarrow \left(r, \phi \pm \pi, z + \frac{p}{2} \right)$

Both the transformations a) e c) change the right-handed helix into a left-handed one and vice versa, but do not change the whole structure. The relation a) represents the reflection symmetry about the *x-y* plane; the c) represents the reflection symmetry about the plane $\phi = 0$ (*z-x* plane).

It is interesting to note that double helices of different radii do not have reflection symmetries. The relation b) is true for all periodic structures with periodicity *p*. The relation d) represents a unique property of double helices having the same pitch p regardless of radii being equal or different. This is in contrast with a single helix which is invariant under the following transformation:

$$(r,\phi,z) \rightarrow \left(r,\phi \pm \frac{2\pi}{p}\delta z, z + \delta z \right)$$

where the choice of sign depends on the versus of the winding.

The double helices enjoy this property only for $\delta z = \dfrac{p}{2}$.

When the reflection symmetries a) and c) are considered together to those of Maxwell's equations any solution must to be either even or odd in ϕ and z except when there is degeneracy.

In Table 7.I the four possible combinations of even and odd solutions which are compatible with the Maxwell's equations solutions and the symmetries properties are reported.

In this project the interest is that of obtaining H_z along the helices axis, for this reason the solutions we shall look at are those of type 3 and 4. Each one of these solutions would give a standing wave, since the z dependence is either odd or even.

Type	Even in ϕ		Odd in ϕ	
	Even in z	Odd in z	Even in z	Odd in z
1	$Ez, H\phi$	Er	Hr	$Hz, E\phi$
2	Er	$Ez, H\phi$	$Hz, E\phi$	Er
3	Hr	$Hz, E\phi$	$Ez, H\phi$	Er
4	$Hz, E\phi$	Hr	Er	$Ez, H\phi$

Table 7. I

7.1.1 Method of solution

General approach to the problem
Let consider firstly a single tape helix. As an approach to the problem, the Floquet's theorem for periodic structures will be used. This theorem implies for the case here that the fields are multiplied only by some complex constant, if one moves down the helix a distance p. This is clear since, if the helix is displaced along the z axis by a distance p, it coincides with itself, and new fields can differ from the previous ones by only a phase factor. Another additional characteristic of symmetry is that if the helix is translated along its axis some distance less than p, it may then be rotated so that it coincides with itself.
Solutions to the Maxwell equations:

$$\nabla \times \bar{E} = -j\omega\mu\bar{H} \qquad (1)$$

$$\nabla \times \bar{H} = j\omega\varepsilon\bar{E} \qquad (2)$$

can be obtained for example in terms of electric and magnetic Hertzian vector potentials, $\bar{\Pi}$ and $\bar{\Pi}^*$, respectively by:

$$\bar{E} = \nabla \times \nabla \times \bar{\Pi} - j\omega\mu\nabla \times \bar{\Pi}^* \quad (3)$$
$$\bar{H} = j\omega\varepsilon\nabla \times \bar{\Pi} + \nabla \times \nabla \times \bar{\Pi}^* \quad (4)$$

where $\bar{\Pi}$ and $\bar{\Pi}^*$ both satisfy an identical wave equation

$$\nabla \times \nabla \times \bar{\Pi} - \nabla\nabla \cdot \bar{\Pi} - k^2\bar{\Pi} = 0 \qquad (5)$$
$$\text{and} \quad \nabla \times \nabla \times \bar{\Pi}^* - \nabla\nabla \cdot \bar{\Pi}^* - k^2\bar{\Pi}^* = 0 \quad (6)$$

If $\bar{\Pi}$ and $\bar{\Pi}^*$ are taken to have only the z components, Π_z and Π_z^*, respectively, then the electric and magnetic field components in cylindrical coordinates can be obtained as follows:

$$E_r = \frac{\partial^2 \Pi_z}{\partial z \partial r} - j\frac{\omega\mu}{r}\frac{\partial \Pi_z^*}{\partial \phi} \qquad (7)$$

$$E_\phi = \frac{1}{r}\frac{\partial^2 \Pi_z}{\partial z \partial \phi} + j\omega\mu\frac{\partial \Pi_z^*}{\partial r} \qquad (8)$$

$$E_z = \frac{\partial^2 \Pi_z}{\partial z^2} + k^2 \Pi_z \qquad (9)$$

$$H_r = j\frac{\omega\mu\varepsilon}{r}\frac{\partial \Pi_z}{\partial \phi} + \frac{\partial^2 \Pi_z^*}{\partial z \partial r} \qquad (10)$$

$$H_\phi = -j\omega\mu\varepsilon\frac{\partial \Pi_z}{\partial r} + \frac{1}{r}\frac{\partial^2 \Pi_z^*}{\partial z \partial \phi} \qquad (11)$$

$$H_z = \frac{\partial^2 \Pi_z^*}{\partial z^2} + k^2 \Pi_z^* \qquad (12)$$

Π_z and Π_z^*, being rectangular components, satisfy the same scalar wave equation:

$$\nabla^2 \Pi_z + k^2 \Pi_z = \frac{1}{r}\frac{\partial}{\partial r}(r\frac{\partial \Pi_z}{\partial r}) + \frac{1}{r^2}\frac{\partial^2 \Pi_z}{\partial \phi^2} + \frac{\partial^2 \Pi_z}{\partial z^2} + k^2 \Pi_z = 0 \qquad (13)$$

$$\nabla^2 \Pi_z^* + k^2 \Pi_z^* = \frac{1}{r}\frac{\partial}{\partial r}(r\frac{\partial \Pi_z^*}{\partial r}) + \frac{1}{r^2}\frac{\partial^2 \Pi_z^*}{\partial \phi^2} + \frac{\partial^2 \Pi_z^*}{\partial z^2} + k^2 \Pi_z^* = 0 \qquad (14)$$

Applying the separation of variables procedure in the above two equations, it is found that the z and ϕ solutions are expressible in exponential form; thus by using in (13) and (14) the form:

$$\begin{cases} \Pi_z \\ \Pi_z^* \end{cases} = f(r)e^{-j\beta_m z}e^{jn\phi} \quad \text{where } \beta_m = \beta_0 + m\frac{2\pi}{p}$$

the function $f(r)$, which contains the r dependence of the elementary solutions, must then be a solution of the differential equation

$$r\frac{dr}{dr}(r\frac{df}{dr}) - [(\beta_m^2 - k^2)r^2 + n^2]f = 0 . \qquad (15)$$

The solutions to equation (15) are the modified Bessel functions of order n and argument $\eta_m(r/a)$ where η_m is given by:

$$\eta_m = \left[\left(\beta^2{}_m - k^2 \right) a^2 \right]^{\frac{1}{2}} = [m^2 \cot^2 \theta + 2m\beta a \cot \theta + \beta^2 a^2 - k^2 a^2]^{\frac{1}{2}}.$$

Since the fields must be finite, the I_n function is chosen for the solution for $0 \le r \le a$ and the K_n function for $a \le r \le \infty$.

In addition, since the complete set of functions must be used to satisfy the boundary conditions at $r=a$, and since the field equations are linear so that the elementary solutions can be added, $\prod_z$ has an expression as follows:

$$\prod_z^i = e^{-jhz} \sum_{m,n} A_{m,n}^i I_n(\eta_m \frac{r}{a}) e^{jn\phi} e^{-jm\frac{2\pi}{p}z} \qquad \text{for } 0 \le r \le a \quad (16)$$

$$\prod_z^e = e^{-jhz} \sum_{m,n} A_{m,n}^e K_n(\eta_m \frac{r}{a}) e^{jn\phi} e^{-jm\frac{2\pi}{p}z} \qquad \text{for } a \le r \le \infty \quad (17)$$

By applying the Floquet's theorem both to the axial and angular coordinate, the relations (16) and (17) become:

$$\prod_z^i = e^{-j\beta_0 z} \sum_m A_m{}^i I_m \left(\eta_m \frac{r}{a} \right) e^{-jm\left(\frac{2\pi}{p}z - \phi \right)} \qquad \text{for } 0 \le r \le a \quad (18)$$

$$\prod_z^e = e^{-j\beta_0 z} \sum_m A_m{}^e K_m \left(\eta_m \frac{r}{a} \right) e^{-jm\left(\frac{2\pi}{p}z - \phi \right)} \qquad \text{for } a \le r \le \infty \quad (19)$$

An identical form occurs for the magnetic hertzian potential $\prod_z^{*i,e}$:

$$\prod_z^{*i} = e^{-j\beta_0 z} \sum_m B_m{}^i K_m \left(\eta_m \frac{r}{a} \right) e^{-jm\left(\frac{2\pi}{p}z - \phi \right)} \qquad \text{for } 0 \le r \le a \quad (20)$$

$$\prod_z^{*e} = e^{-j\beta_0 z} \sum_m B_m{}^e K_m \left(\eta_m \frac{r}{a} \right) e^{-jm\left(\frac{2\pi}{p}z - \phi \right)} \qquad \text{for } a \le r \le \infty \quad (21)$$

where the apices *i, e* denote the internal and external fields respectively, $A_m{}^{i,e}$ and $B_m{}^{i,e}$ are the unknown fields constants. Using the relations (18), (19), (20), (21), one can readily find the field components in terms of the $A_m{}^{i,e}$ and $B_m{}^{i,e}$ coefficients, which are related by the continuity requirements of the field boundary conditions at *r=a*:

$$\left.\begin{array}{l} E^{i}_{z,\phi} = E^{e}_{z,\phi} \\ J_{\phi} = H^{i}_{z} - H^{e}_{z} \\ J_{z} = H^{e}_{\phi} - H^{i}_{\phi} \end{array}\right\} \text{ for } r = a \qquad (22)$$

The expressions of the surface current density components must have the same form as the field's components; in particular:

$$J_{\phi} = e^{-j\beta_0 z} \sum_{m} j_{\phi m} e^{-jm(\frac{2\pi}{p}z-\phi)} \qquad (23)$$

$$J_{z} = e^{-j\beta_0 z} \sum_{m} j_{zm} e^{-jm(\frac{2\pi}{p}z-\phi)} \qquad (24)$$

where $j_{\phi m}$ and j_{zm} are the Fourier coefficients of the current density expansion. It is to be noticed that equations (23) and (24) represent the components of the total surface current density that is the sum of the current density of both sides of the infinitesimally thick perfectly conducting tape. Using equations (22), (23) and (24) one can find the values $A_m^{i,e}$ and $B_m^{i,e}$ in terms of $j_{\phi m}$ and j_{zm}, where use is made of the orthogonality of the Fourier space harmonics for $0 \le \phi \le 2\pi$ and $0 \le z \le p$. After some algebra the expressions of the field's components are found [2]:

$$E^{e}_{z} = j\frac{e^{j\beta_0 z}}{\omega \varepsilon a} \sum_{m} \left\{ \eta^{2}_{m} I_{m}(\eta_{m}) K_m\left(\eta_{m}\frac{r}{a}\right) j_{zm} - m\beta_{m} a I_{m}(\eta_{m}) K_m\left(\eta_{m}\frac{r}{a}\right) j_{\phi m} \right\} e^{jm\left(\frac{2\pi}{p}z-\phi\right)}$$

$$E^{e}_{r} = j\frac{e^{j\beta_0 z}}{\omega \varepsilon a} \sum_{m} \left\{ -\beta_{m} a \eta_{m} I_{m}(\eta_{m}) K'_{m}\left(\eta_{m}\frac{r}{a}\right) j_{zm} + \right.$$

$$\left. + \frac{m}{\eta_{m}}[\beta^{2}_{m} a^{2} I_{m}(\eta_{m}) K'_{m}\left(\eta_{m}\frac{r}{a}\right) + \frac{a}{r} k^{2} a^{2} I'_{m}(\eta_{m}) K_{m}\left(\eta_{m}\frac{r}{a}\right)] j_{\phi m} \right\} e^{jm\left(\frac{2\pi}{p}z-\phi\right)}$$

$$E^{e}_{\phi} = j\frac{e^{j\beta_0 z}}{\omega \varepsilon a} \sum_{m} \left\{ -\frac{a}{r} m\beta_{m} a I_{m}(\eta_{m}) K_{m}\left(\eta_{m}\frac{r}{a}\right) j_{zm} + \right.$$

$$\left. + \frac{1}{\eta^{2}_{m}}[\frac{a}{r} m^{2} \beta^{2}_{m} a^{2} I_{m}(\eta_{m}) K_{m}\left(\eta_{m}\frac{r}{a}\right) + \eta^{2}_{m}\frac{a}{r} k^{2} a^{2} I'_{m}(\eta_{m}) K'_{m}\left(\eta_{m}\frac{r}{a}\right)] j_{\phi m} \right\} e^{jm\left(\frac{2\pi}{p}z-\phi\right)}$$

$$H^e_z = e^{j\beta_0 z} \sum_m \left\{ \eta_m I'_m(\eta_m) K_m\left(\eta_m \frac{r}{a}\right) J_{\phi m} \right\} e^{jm\left(\frac{2\pi}{p}z - \phi\right)}$$

$$H^e_r = je^{j\beta_0 z} \sum_m \left\{ m\frac{a}{r} I_m(\eta_m) K_m\left(\eta_m \frac{r}{a}\right) j_{zm} + \right.$$

$$\left. -\frac{\beta_m a}{\eta_m^2}[m^2 \frac{a}{r} I_m(\eta_m) K_m\left(\eta_m \frac{r}{a}\right) + \eta_m^2 I'_m(\eta_m) K'_m\left(\eta_m \frac{r}{a}\right)] j_{\phi m} \right\} e^{jm\left(\frac{2\pi}{p}z - \phi\right)}$$

$$H^e_\phi = e^{j\beta_0 z} \sum_m \left\{ -\eta_m I_m(\eta_m) K'_m\left(\eta_m \frac{r}{a}\right) j_{zm} + \right.$$

$$\left. +\frac{m\beta_m a}{\eta_m}[I_m(\eta_m) K_m\left(\eta_m \frac{r}{a}\right) + \frac{a}{r} I'_m(\eta_m) K_m\left(\eta_m \frac{r}{a}\right)] j_{\phi m} \right\} e^{jm\left(\frac{2\pi}{p}z - \phi\right)}$$

The prime on the I_m and K_m functions means differentiation with respect to the argument.
For the internal fields the expressions are the same but the modified Bessel functions are everywhere interchanged.
The complete treatment of the single tape model is in [2]
Case of the twin tape helices
In the case of a double tape helix a suitable solution for, say E_z and H_z, would be a doubly infinite series of the form:

$$\sum_{m=-\infty}^{+\infty} \sum_{l=-\infty}^{+\infty} A_{l,m} R_{l,m}(r) e^{j\left\{ \left[\beta_{0,0} + \frac{2\pi}{p}(l+2m) \right] z - l\phi \right\}} \qquad (31)$$

where the functions $R_{l,m}(r)$ are the modified Bessel functions of the first and second order or a particular combination of them.
For a single tape, as already said, the l index is not required, therefore in the field expressions there is a single sum.
If one considers the general case of two different radii a and b, one has different series of the type (31) for the regions:
1) r<a; 2) a<r<b; 3) r>b.
For region 1) (r<a) one finds:

$$R_{l,m}(r) = I_{l,m}(\gamma_{l,m} r) \qquad \text{where} \qquad \gamma_{l,m}^2 = \beta_{l,m}^2 - k^2 \text{ and}$$

$$\beta_{l,m} = \beta_{0,0} + \frac{2\pi}{p}(l+2m).$$

For region 3) (r>b) one has the corresponding function:

$$R_{l,m}(r) = K_{l,m}(\gamma_{l,m}r).$$

Region 2) (a<r<b) $R_{l,m}(r)$ is a combination of the $I_{l,m}$ e $K_{l,m}$ functions. The series for any quantity in two neighbouring regions should match each other on the common boundaries, except on the helices where E_r, H_ϕ and H_z have discontinuities depending on the current or charge density.

Introducing surface current densities $\underline{J}(a)$ and $\underline{J}(b)$ and their components $J_\phi(a), J_z(a)$, $J_\phi(b)$ e $J_z(b)$, as for the case of a single tape, one can find the $A_{l,m}$ coefficients in terms of the components of the surface current densities. In particular, if these current densities are expanded in a Fourier series of the form:

$$\underline{J}(a,\phi,z) = \sum_{l,m} \underline{J}(a)_{l,m} e^{j(\beta_{l,m}z - l\phi)} \qquad (32\text{ a})$$

$$\underline{J}(b,\phi,z) = \sum_{l,m} \underline{J}(b)_{l,m} e^{j(\beta_{l,m}z - l\phi)} \qquad (32\text{ b})$$

Then all the field quantities can be expressed in terms of the coefficient $\underline{J}(a)_{l,m}$ and $\underline{J}(b)_{l,m}$.

For the case $a = b$, which is the case of interest here, one gets the following general expressions for E_z and H_z:

$$E_z = \sum_{l=-\infty}^{+\infty} \sum_{m=-\infty}^{+\infty} (E_z)_{l.m} e^{j(\beta_{l,m}z - l\phi)} \qquad (33)$$

where   for   r>a

$$(E_z)_{l,m} = \frac{(\gamma_{l,m}a)^2}{jka} \Big[I_m(\gamma_{l,m}a) K_m(\gamma_{l,m}r) \Big] \cdot$$

$$\cdot \left\{ \Big[J_z(a^-)_{l,m} + J_z(a^+)_{l,m} \Big] - \frac{l\beta_{l,m}a}{(\gamma_{l,m}a)^2} \Big[J_\phi(a^-)_{l,m} + J_\phi(a^+)_{l,m} \Big] \right\}$$

and for r<a

$$(E_z)_{l,m} = \frac{(\gamma_{l,m}a)^2}{jka} \Big[K_m(\gamma_{l,m}a) I_m(\gamma_{l,m}r) \Big] \cdot$$

$$\cdot \left\{ \Big[J_z(a^-)_{l,m} + J_z(a^+)_{l,m} \Big] - \frac{l\beta_{l,m}a}{(\gamma_{l,m}a)^2} \Big[J_\phi(a^-)_{l,m} + J_\phi(a^+)_{l,m} \Big] \right\}$$

$$H_z = \sum_{l=-\infty}^{+\infty} \sum_{m=-\infty}^{+\infty} (H_z)_{l,m} \, e^{j(\beta_{l,m}z - l\phi)} \qquad (34)$$

where for r>a

$$(H_z)_{l,m} = -(\gamma_{l,m}a) \Big[I'_m(\gamma_{l,m}a) K_m(\gamma_{l,m}r) \Big] \Big[J_\phi(a^-)_{l,m} + J_\phi(a^+)_{l,m} \Big]$$

for r<a

$$(H_z)_{l,m} = -(\gamma_{l,m}a) \Big[K'_m(\gamma_{l,m}a) I_m(\gamma_{l,m}r) \Big] \Big[J_\phi(a^-)_{l,m} + J_\phi(a^+)_{l,m} \Big].$$

In these expressions a^- and a^+ denote the right-handed and left-handed helices, respectively. From E_z and H_z all other field components can be derived.

A first important consideration that can be done observing the above expressions is that tangential E will be continuous in crossing the tape, independent the choice of the coefficients or the current amplitudes, so the first boundary condition is satisfied. In addition the third boundary condition is also satisfied provided that the coefficients in (32 a) and (32 b) are so chosen that the current amplitudes are zero off the helices. For this reason one must requires that the total tangential electric field, which will be denoted $\bar{E}_t$, at the tapes vanishes. Since the linear current density $\bar{J}$ vanishes everywhere off the tape, this boundary condition is conveniently stated by saying that the scalar product $\bar{E}_t \cdot \bar{J}^*$ is identically zero on the surface $r=a$. Resolving the $\bar{E}_t$ and $\bar{J}^*$ vectors into components parallel (∥) and perpendicular (⊥) to the tape winding direction, this conditions becomes:

$$E_\parallel J_\parallel^* + E_\perp J_\perp^* = 0 \text{ at } r=a \qquad (35)$$

For an approximate solution, the component of current density perpendicular to the tape direction, which is small for narrow tapes, can be neglected; in this way the second term in the (35) is ignored and $E_\perp$ results to be zero everywhere.

Finally, it is relaxed the requirement to the extent that only the integral of equation (35) over the surface $r=a$ must vanish. Physically this means that no net real or reactive power flows out of the tape surface. Approximate solutions for the antisymmetrical mode

From the relations between the components of $\bar{H}$ and $\bar{J}$ it follows (see Fig. 7.1) that:

$$\begin{cases} J_\phi\left(a^+,\phi,z\right) = J_\phi\left(a^-,\phi,z\right) \\ J_z\left(a^+,\phi,z\right) = -J_z\left(a^-,\phi,-z\right) \end{cases} \qquad (36)$$

Let $J_\parallel\left(a^-\right), J_\perp\left(a^-\right), J_\parallel\left(a^+\right), J_\perp\left(a^+\right)$ be the current densities parallel and orthogonal to the tape for the twin helices, then J_z and J_ϕ can be expressed in terms of $J_\parallel$ e $J_\perp$ and of the θ angle (Fig. 7.1):

$$\begin{cases} J_z\left(a^-\right) = J_\parallel\left(a^-\right)\sin\theta + J_\perp\left(a^-\right)\cos\theta \\ J_\phi\left(a^-\right) = J_\parallel\left(a^-\right)\cos\theta - J_\perp\left(a^-\right)\sin\theta \\ -J_z\left(a^+\right) = J_\parallel\left(a^+\right)\sin\theta + J_\perp\left(a^+\right)\cos\theta \\ J_\phi\left(a^+\right) = J_\parallel\left(a^+\right)\cos\theta - J_\perp\left(a^+\right)\sin\theta \end{cases} \qquad (37)$$

hence the (36) becomes:

$$\begin{cases} J_\parallel\left(a^+,\phi,z\right) = J_\parallel\left(a^-,\phi,-z\right) \\ J_\perp\left(a^+,\phi,z\right) = J_\perp\left(a^-,\phi,-z\right) \end{cases} \qquad (38)$$

The Fourier coefficients $J_\parallel$ e $J_\perp$ can be defined as follows:

$$
\begin{cases}
J_{\parallel}\left(a^{-},\phi,z\right) = \sum_{l=-\infty}^{+\infty}\sum_{m=-\infty}^{+\infty} J_{\parallel}\left(a^{-}\right)_{l,m} e^{j\left(\beta_{l,m}z-l\phi\right)} \\[2mm]
J_{\perp}\left(a^{-},\phi,z\right) = \sum_{l=-\infty}^{+\infty}\sum_{m=-\infty}^{+\infty} J_{\perp}\left(a^{-}\right)_{l,m} e^{j\left(\beta_{l,m}z-l\phi\right)} \\[2mm]
J_{\parallel}\left(a^{+},\phi,z\right) = \sum_{l=-\infty}^{+\infty}\sum_{m=-\infty}^{+\infty} J_{\parallel}\left(a^{+}\right)_{l,m} e^{j\left(\beta_{l,m}z-l\phi\right)} \\[2mm]
J_{\perp}\left(a^{+},\phi,z\right) = \sum_{l=-\infty}^{+\infty}\sum_{m=-\infty}^{+\infty} J_{\perp}\left(a^{+}\right)_{l,m} e^{j\left(\beta_{l,m}z-l\phi\right)}
\end{cases}
\tag{39}
$$

As already said, the current density component orthogonal to the tape is neglecting, being the thickness tape small compared with the tape width, the helices radius and the wavelength.

Since $\beta_{l,m} = \beta_{-l,m+l}$, as results by the following relation:

$$
\beta_{l,m} = \beta_{0,0} + \frac{2\pi}{p}(m+2l)
$$

$$
\beta_{-l,m+l} = \beta_{0,0} + \frac{2\pi}{p}\left[-l+2(l+m)\right] = \beta_{0,0} + \frac{2\pi}{p}(l+2m)
$$

and for the relations (38) and (39), one can find:

$$
J_{\parallel}\left(a^{+}\right)_{l,m} = J_{\parallel}\left(a^{-}\right)_{-l,m+l}
\tag{40}
$$

By substituting in the field expressions (33) and (34), it will be resulted that, for $l=0$, $(E_z)_{l,m}=0$ and thus $E_z=0$.

In more details:

$$
E_z = \sum_{l=-\infty}^{+\infty}\sum_{m=-\infty}^{+\infty} \left(E_z\right)_{l,m} e^{j\left(\beta_{l,m}z-l\phi\right)}
$$

where   for   r>a

$$
\left(E_z\right)_{l,m} = \frac{\left(\gamma_{l,m}a\right)^2}{jka}\left[I_m\left(\gamma_{l,m}a\right)K_m\left(\gamma_{l,m}r\right)\right]\cdot
$$

$$
\cdot\left\{\left[J_z\left(a^{-}\right)_{l,m} + J_z\left(a^{+}\right)_{l,m}\right] - \frac{l\beta_{l,m}a}{\left(\gamma_{l,m}a\right)^2}\left[J_{\phi}\left(a^{-}\right)_{l,m} + J_{\phi}\left(a^{+}\right)_{l,m}\right]\right\}
$$

and for r<a

$$(E_z)_{l,m} = \frac{(\gamma_{l,m}a)^2}{jka}\left[K_m(\gamma_{l,m}a)I_m(\gamma_{l,m}r)\right].$$

$$\cdot\left\{\left[J_z(a^-)_{l,m} + J_z(a^+)_{l,m}\right] - \frac{l\beta_{l,m}a}{(\gamma_{l,m}a)^2}\left[J_\phi(a^-)_{l,m} + J_\phi(a^+)_{l,m}\right]\right\}$$

for *m=0* , taking into account that the following relations are true

$$J_z(a^-)_{l,m} = J_\parallel(a^-)_{l,m}\sin\theta$$

$$J_z(a^+)_{l,m} = -J_\parallel(a^+)_{l,m}\sin\theta$$

and that, for the equation (40), $J_\parallel(a^-)_{0,m} = J_\parallel(a^+)_{0,m}$,

it results that $J_z(a^-)_{0,m} + J_z(a^+)_{0,m} = 0$.

Finally, this means to say that for l=0 the terms into brackets in the expression of *(E_z)_{l,m}* becomes zero, and so E_z=0.

Thus the antisymmetrical solution has no E_z component with l=0; in other words the fundamental component of the wave field is a pure TE field, since the TM parts of the fundamental component arising from the two helices cancel each other.

7.2 Numerical characterization of the applicator

The objectives of this study are to design and realize a magnetic field applicator in order to carry out bioexperiments for the remote control of biological nanomachines. The experimental study presented in the previous chapter evidentiated that the interesting effect observed by HS et al. is probably due to bulk heating of solution, being present inside the applicator a strong electric field. In order to verify the possibility that a biological nanomachine might work, the following steps have to be considered:

1) realization of an applicator which ensures a minimization of the electric field with respect to the magnetic one;
2) thermostating system of the exposed sample and of the field applicator;
3) performing of spectrophotometer analysis contemporary to the EMF exposures.

Concerning the first point the double tape helix model, previously described, ensuring a minimum interaction with the electric field with respect to the magnetic field, matches very well the EM constraint; therefore, a double tape applicator has been numerically evaluated. Different configurations have been tested in order to obtain the best results in terms of the ratio between the average electric field amplitude and the average magnetic field amplitude. The results are reported in the following sections.

7.2.1 EM applicator

The numerical analysis is carried out by using the commercial code Ansoft® HFSS v10 based on the finite element method (FEM). The applicator is constructed by two tape helices each one of 35 turns, as reported in [5]. The tape of the helices is 1 mm width and 100 µm thick; the helices radii are quite similar (R1=20mm, R2=20.5mm), the distance between the helices is 0.5 mm and the pitch p is 9 mm (Fig. 7.2). All these geometric parameters have been chosen in order to better approximate the theoretical model, according to it, helices radii have to be equal and the thickness tape has to be small compared with the tape width, the helices radius and the wavelength. The chosen working frequency was 2 MHz. Inside the applicator a sample of distilled water ($\varepsilon_r = 80$ and $\sigma_{eff} = 0.0002 S/m$) was inserted; the sample has been assumed to have perfectly cylindrical shape (r =11.3 mm, h= 40 mm) and the meniscus at the top of the sample has been not considered. In the numerical analysis the wire was considered to be a perfect electric conductor (p.e.c.) and the magnetic properties of the materials were taken as those of the free space ($\mu = \mu_0$).

According to the FEM method, the region of interest was divided in tetrahedral elements (150617); the mesh generation was based both on the material wavelength (λ_m=6.7 m) refinement and on the length based mesh refinement; thus the length of the tetrahedral elements were refined until they were below a specified value. In this case we

adopted as the maximum length of a tetrahedron (i.e. the length of its longest edge) $l = 8$mm.
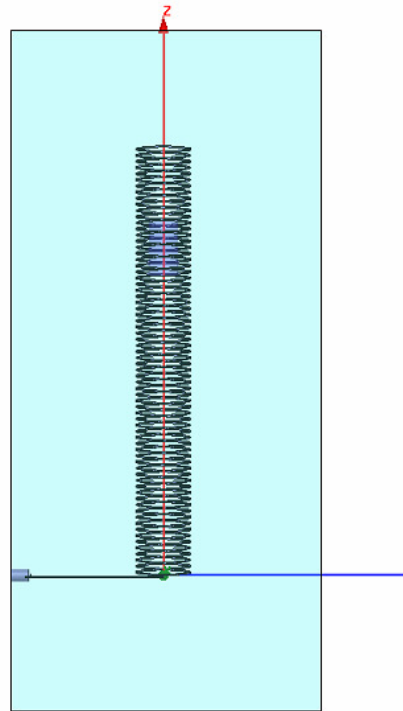
Fig. 7. 2. Structure of the simulated applicator.

In Figg. 7.3, 7.4, 7.5 and 7.6 the distributions of electric and magnetic field in the *xz* and *yz* planes are shown respectively. From these figures results that a minimum of electric field is present along the z axis as predicted by the theoretical model, while a uniform distribution of magnetic field is present inside the applicator.
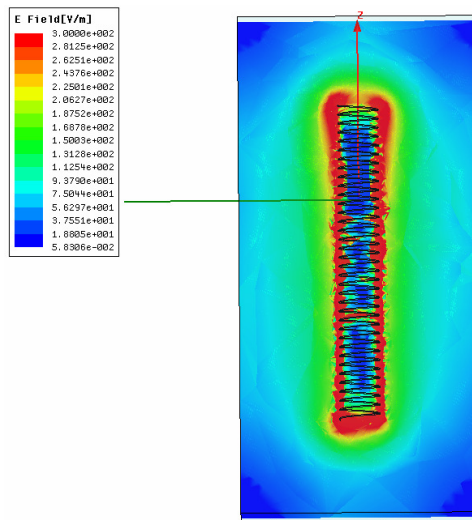
Fig. 7. 3. Electric field amplitude in the xz plane passing through the center of the helices.
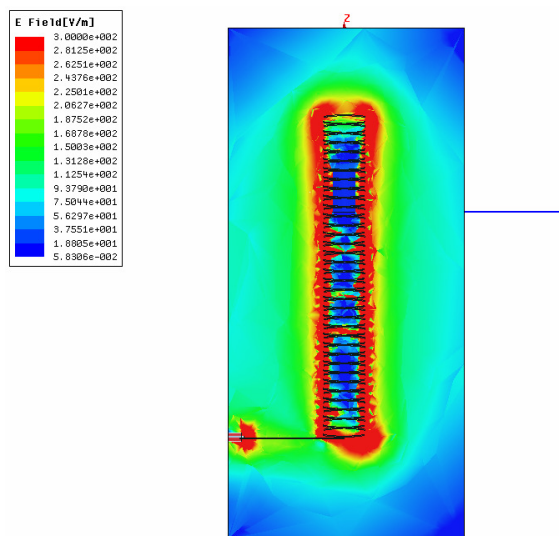
Fig. 7. 4. Electric field amplitude in the yz plane passing through the center of the helices.
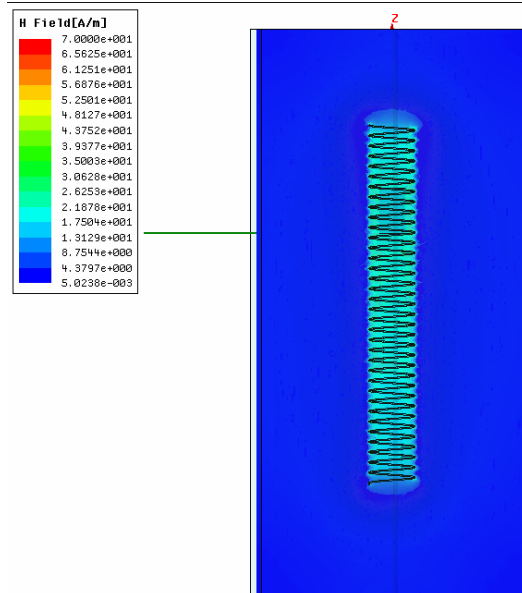
Fig. 7. 5. Magnetic field amplitude in the xz plane passing through the center of the helices.
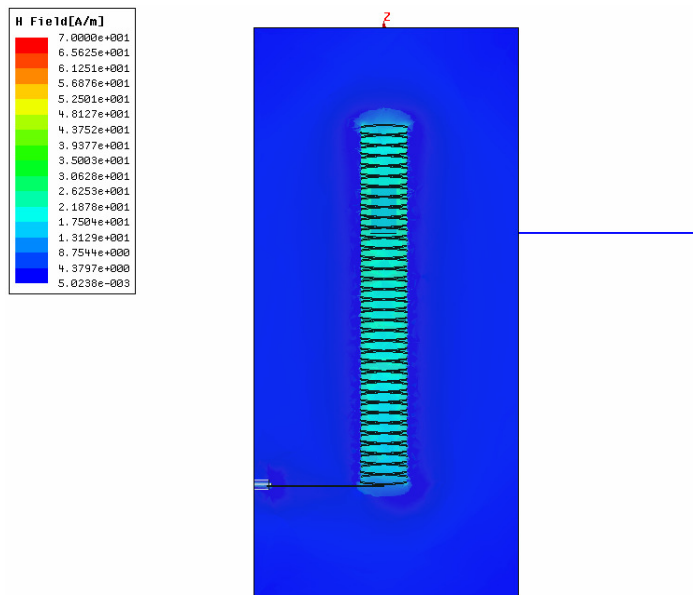
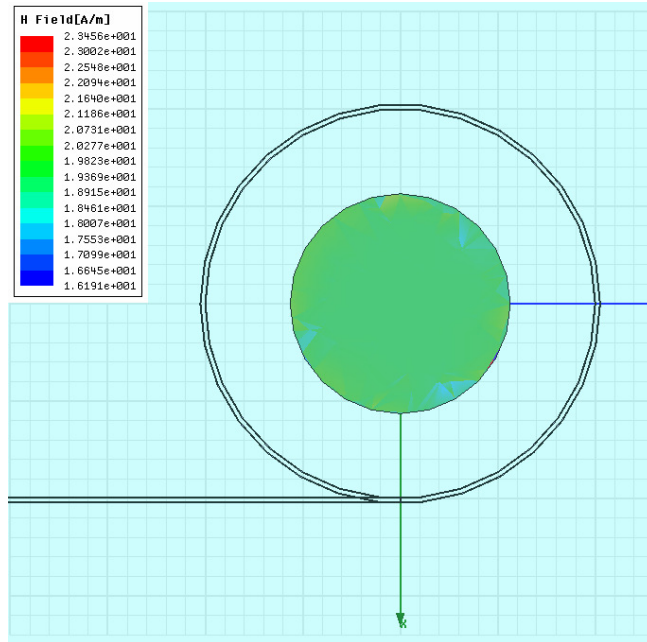**Fig. 7. 6. Magnetic field amplitude in the yz plane passing through the center of the helices**

In the following figures a zoom view into the sample of the electric and magnetic field distribution is reported.
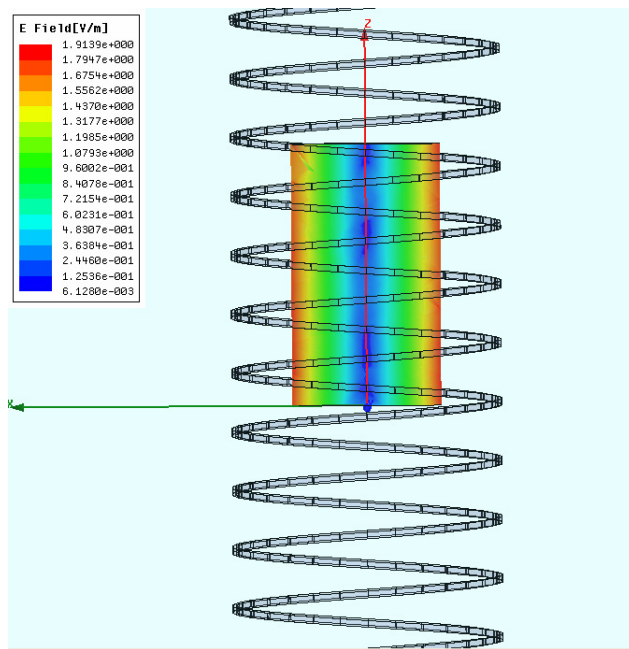
Fig. 7. 7. Electric field amplitude in the xz plane passing through the center of the sample.
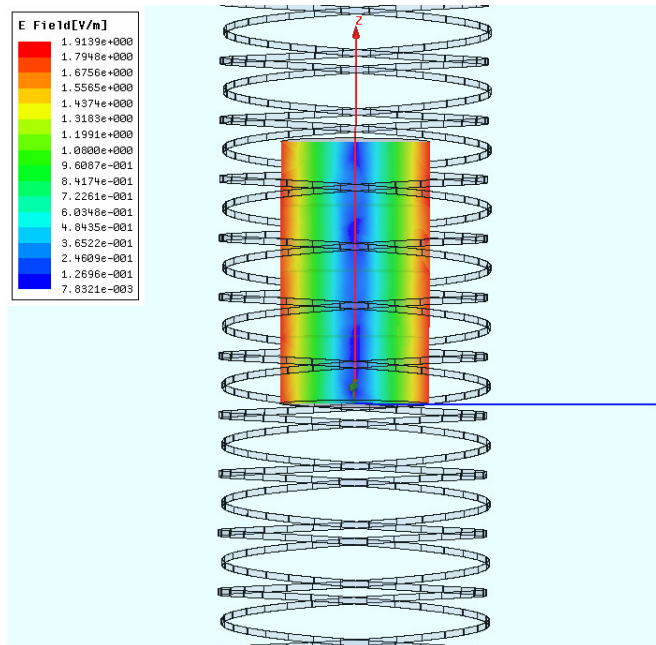
Fig. 7. 8. Electric field amplitude in the yz plane passing through the center of the sample.
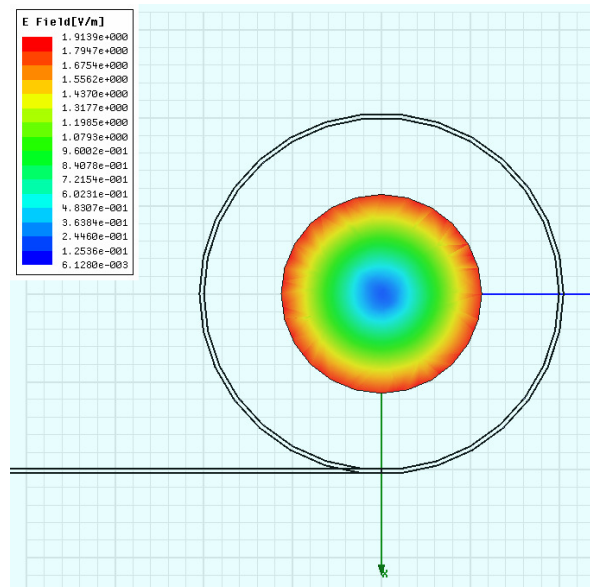
Fig. 7. 9. Electric field amplitude in the xy plane passing through the center of the sample.
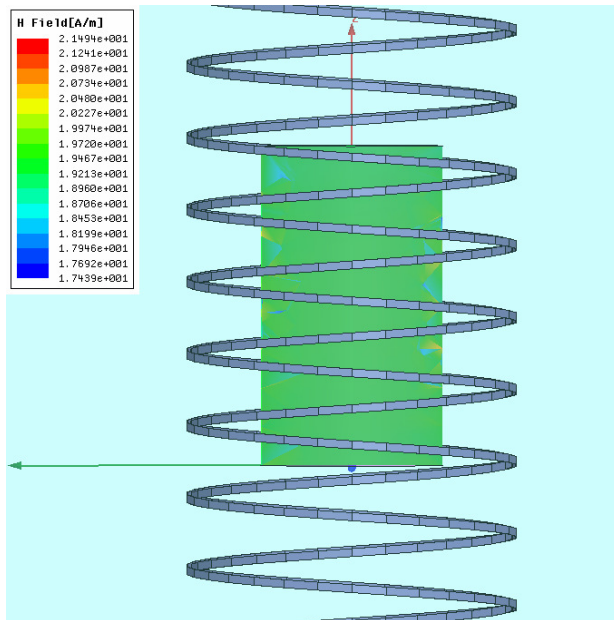
Fig. 7. 10. Magnetic field amplitude in the xz plane passing through the center of the sample.
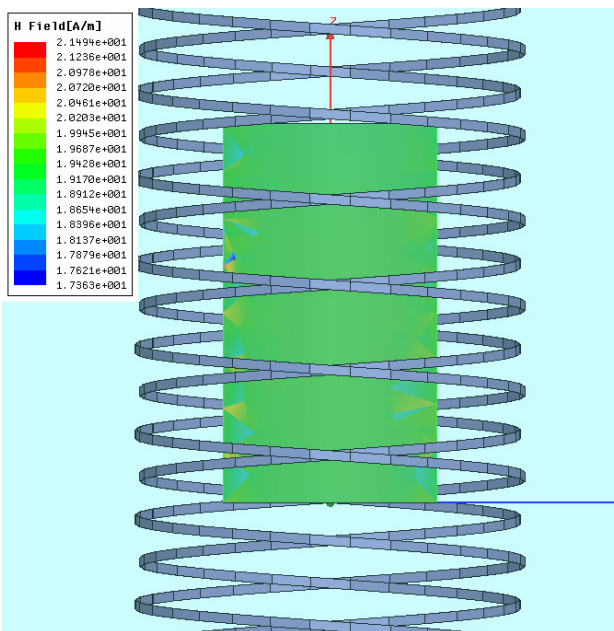
Fig. 7. 11. Magnetic field amplitude in the yz plane passing through the center of the sample.

Fig. 7. 12. Magnetic field amplitude in the xy plane passing through the center of the sample.

The average electric field distribution into the sample resulted to be 0.5 V/m given the input power P_0=1 W, while the average magnetic field distribution resulted to be 19 A/m; in this way the electric field is reduced by two magnitude orders with respect to the magnetic field.

These first numerical results have been very satisfactory and have been induced the possibility of realizing an exposure system to be used both for the remote control of biological nanomachines and for in vitro experiments of selective hyperthermia by using magnetic nanoparticles.

7.2.2 EM applicator for selective hyperthermia

Since the objective was to realize an exposure system integrated with a thermostating control of both samples and applicator, and integrated with a unit for the spectrophotometric analysis during the exposures, the numerical analysis dealt with an applicator which could satisfy these requirements. In order to perform in vitro experiment for the thermoablation of the tumoral cells by selective hyperthermia the

following requirements have to be taken into account in the designing phase of the applicator:

- The applicator dimensions must enable the insertion of two cylindrical cuvettes: a first filled with a solution of cellular culture medium plus a suspension of magnetic nanoparticles, simulating the cancerous cells, and a second one, coaxial to the first, filled with cellular culture medium alone, simulating the surrounding healthy cells.
- It is necessary to transfer a higher amount of energy in the tumoral tissue than the surrounding healthy tissue; therefore the field distribution must ensure a strong coupling with the magnetic nanoparticles.

Hence, the investigated applicator is constituted by two tape helices each one of 21 turns, with an open structure after 16 turns in order to maximize light passage. The tape of the helices is 1 mm width, 100 µm thick and the pitch p is 9 mm; the helices radii are quite similar (R1=25mm, R2=25.5mm) and are chosen in order to include the two cylindrical cuvettes (Fig. 7.13).
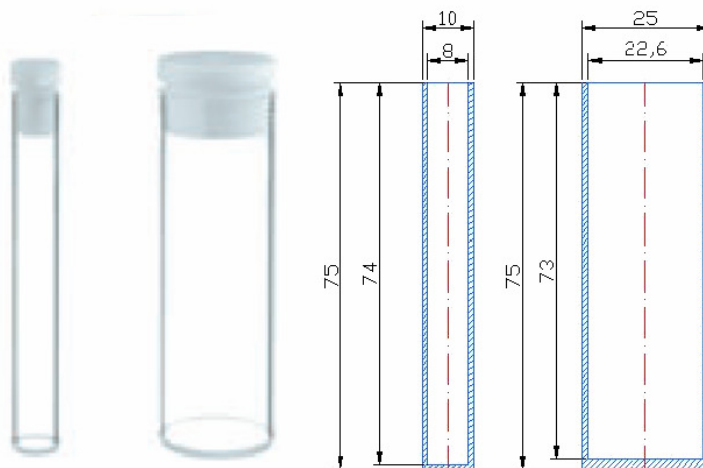
Fig. 7. 13. Cylindrical quartz cuvettes; dimensions are given in mm.

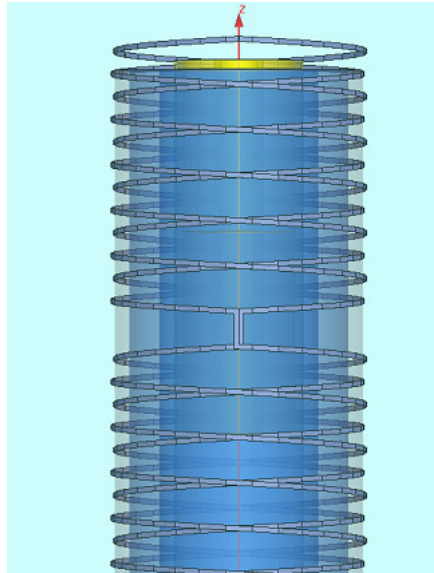The simulated structure is presented in the following figure.

Fig. 7. 14. Side view of the simulated structure. The gap enable the insertion of two optic fibers to be connected to the spectrophotometer.
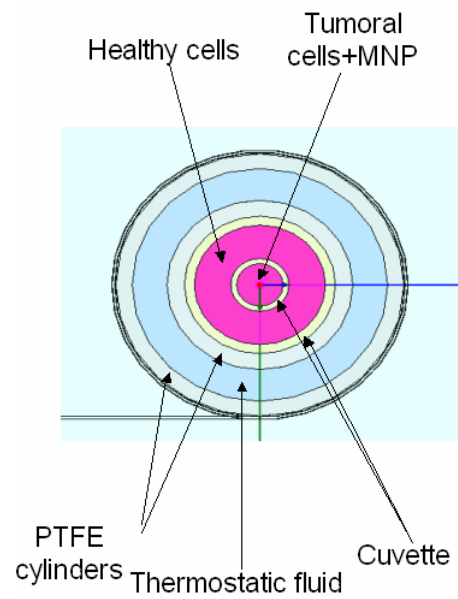

Fig. 7. 15. Top view of the simulated structure.

Relative permittivity ε_r and effective conductivity σ_{eff} at 37°C (5 MHz) were $\varepsilon_r = 80$ and $\sigma_{eff} = 0.16 S/m$ for the samples (DMEM) and $\varepsilon_r = 3.78$ and conductivity equal to zero for the quartz glass. The wire was considered to be a perfect electric conductor (p.e.c.) and the magnetic properties of the materials were taken as those of the free space ($\mu = \mu_0$). The region of interest was divided in tetrahedral elements (104676); in this case the maximum length of a tetrahedron l = 8mm was adopted. The following figures show the calculated electric and magnetic field distribution inside the two samples.
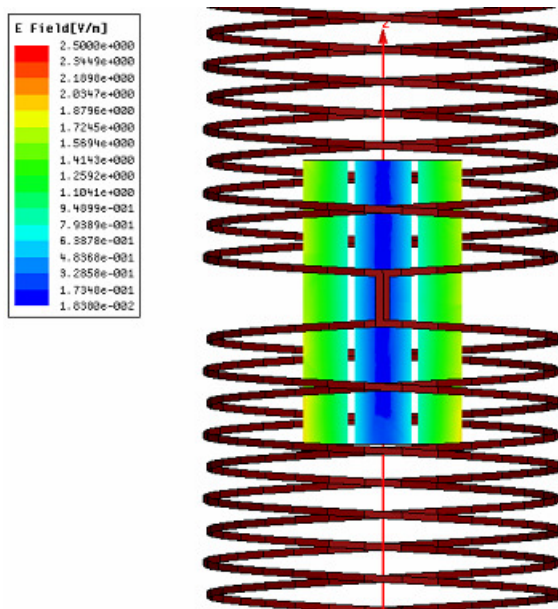
Fig. 7. 16. Electric field amplitude in the yz plane passing through the center of the two samples.
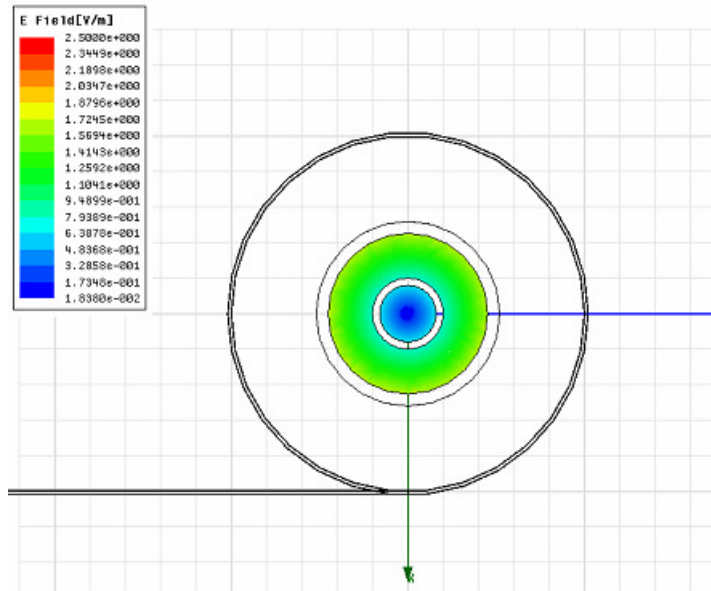
Fig. 7. 17. Electric field amplitude in the xy plane passing through the center of the two samples
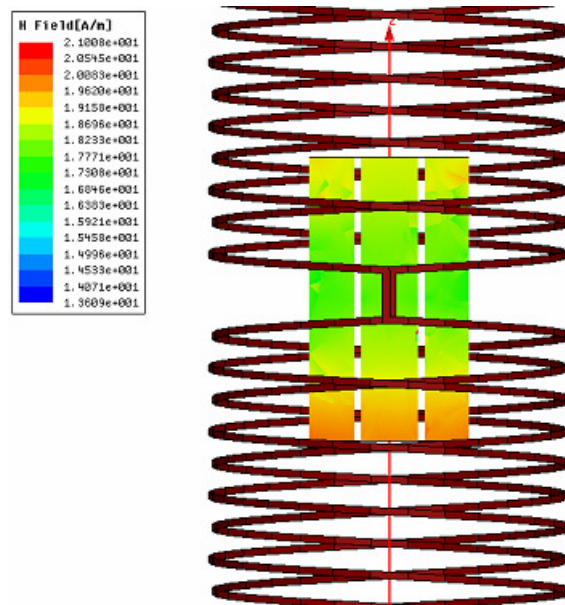

Fig. 7. 18. Magnetic field amplitude in the yz plane passing through the center of the two samples.
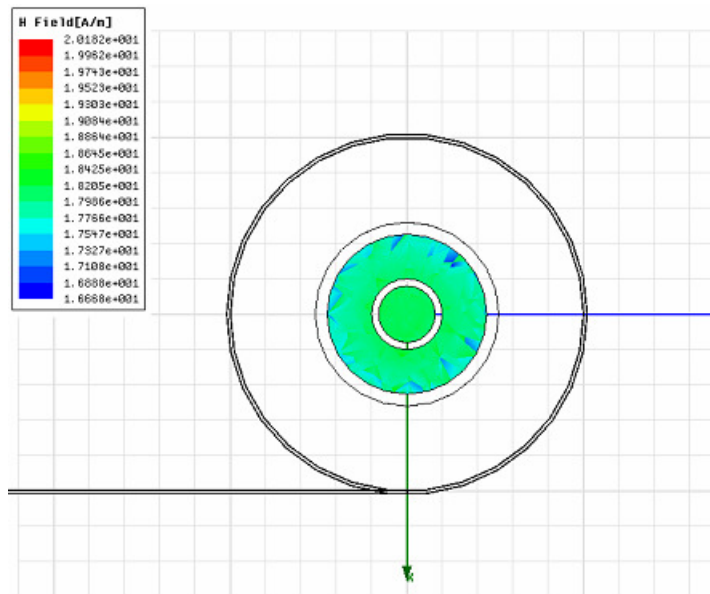
Fig. 7. 19. Magnetic field amplitude in the xy plane passing through the center of the two samples.

The above figures show the good results achieved in order to minimize the electric field with respect to the magnetic one.

For a more in depth analysis, calculated data have been post-processed by using simple Matlab scripts. In particular the electric and magnetic field data along a plane passing through the center of the samples (in the position of the gap) were exported in order to evaluate the electric and magnetic field vector norm. At the working frequency of 2MHz it turns out that for the internal sample the electric field vector norm is $\|E\| = 0.3$ V/m, while the magnetic field vector norm is $\|H\| = 16.5$ A/m; in this way a ratio between the two norms results equal to 0.02 Ω. In addition the calculated values have been processed in order to evaluate the electric and magnetic fields components inside both the cuvette (Figg. 7.20, 7.21).
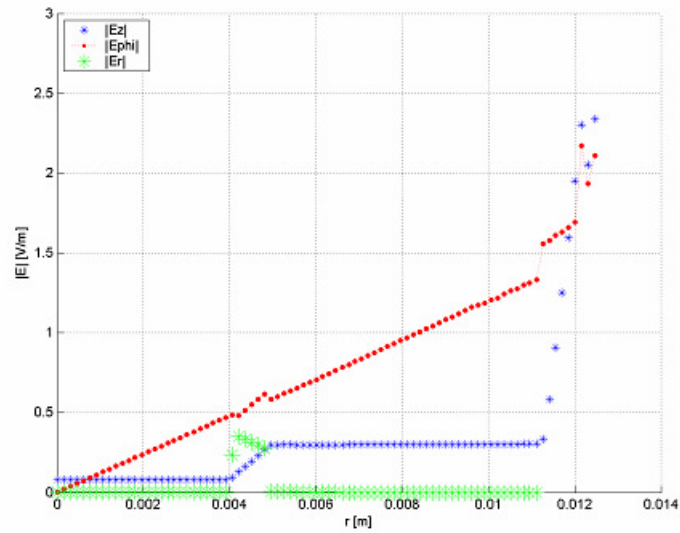
Fig. 7. 20. Electric field components along the radial axis.
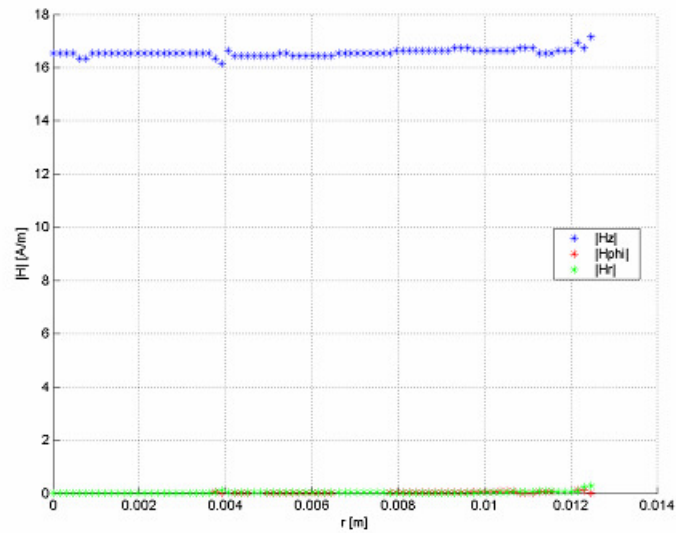

Fig. 7. 21. Magnetic field components along the radial axis

From these figures it is evident the behavior of the field distribution: the magnetic predominant component is H_z, while the electric predominant component is E_ϕ. The gap at r=0.004m occurs for the presence of the quartz cuvette and is justified by applying the continuity of tangential fields components and the continuity of the normal components of the inductions at the interfaces.

In order to obtain an EM characterization of the applicator as function of the frequency, the field's distributions inside the sample has been calculated in the range 500 kHz – 10 MHz (Fig. 7.22). As resulted in figure the ratio between the electric and magnetic field norms is linear with frequency.
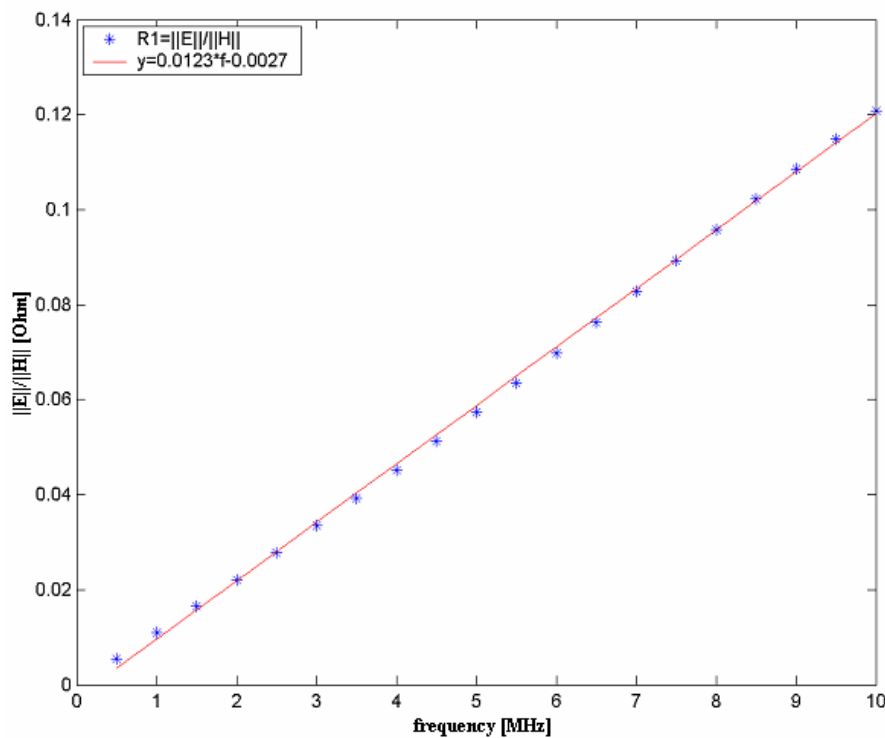

Fig. 7. 22. ‖E‖/‖H‖ as function of the frequency.

The above results are very satisfactory; in addition, since the applicator behavior has been characterized as function of frequency, in the range 500 kHz – 10 MHz it is possible to choose the working

frequency for the experiments. It is to be noted that the working frequency is a parameter depended also by the magnetic nanoparticles characteristics. By combining together the electromagnetic properties of the applicator and the characteristics (size, concentration and composition) of the magnetic nanoparticles to be applied, it is possible to define all the parameters necessary to the experiments.

7.3   Realization of the applicator

The simulated applicator has been realized according to the following procedure: 1) on two sides of a FR4 sheet of 100 µm thick the two tape helices has been printed (Fig. 7.23); 2) the sheet has been covered on both sides by an insulated material; 3) the sheet has been round on a cylindrical stand; 4) the two ends of the sheet has been put in electric contact by localized weldings.
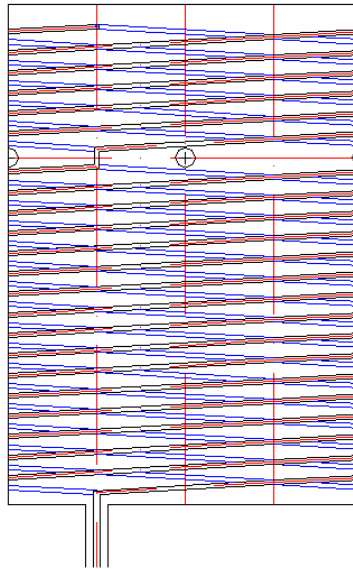

Fig. 7. 23

Finally, by using a vector network analyzer (Agilent), first preliminary measurements of the input impedance of the applicator have been carried out in the frequency range 300 kHz – 10 MHz.

7.4   Conclusions

This chapter dealt with the design of a magnetic field applicator, which could be used both for the remote control of nanomachines and for the selective hyperthermia for cancer therapy. To this end a theoretical model of a twin tape helical applicator has been developed in order to reduce the influence of the magnetic field with respect to the electric field. In addition, a numerical analysis of the applicator integrated with a thermostating control of the samples, and with a unit for the spectrophotometric analysis during the exposures, has been carryed out. The obtained numerical results have been very satisfactory; for this reason a prototype of the simulated model has been realized and a first preliminary experimental characterization has been performed in order to design the matching network.

References

[1] M. Chodorow, E.L. Chu, "Cross-Wound Twin Helices for Traveling-Wave Tubes", Journal of Applied Physics, vol. 26, no. 1, 1955.

[2] S. Sensiper, "Electromagnetic Wave Propagation on Helical Conductors", Ph. D. Dissertation, Research Laboratory of Electronics, Massachusetts Institute of Technology, Cambridge, Massachusetts, 1951.

[3] C. K. Birdsall, T.E. Everhart, "Modified contra-Wound Helix Circuit for High-Power Traveling-Wave Tube", IRE Transactions on Electron Devices, 1956.

[4] S. D'Agostino, F. Emma, C. Paglioni, "Accurate Analysis of Helix Slow-Wave Structures", IEEE Transactions on Electron Devices, vol. 45, no. 7, 1998.

[5] K. Hamad-Schifferli, J.J. Schwartz, A.T. Santos., S. Zhang, and J.M. Jacobson: "Remote electronic control of DNA hybridization through inductive coupling to an attached metal nanocrystal antenna". Nature, 415, 152-155, 2002.

Conclusions

This thesis dealt with the design and characterization of *in vitro* exposure systems for the bioelectromagnetic research.

A rigouros approach in the development of such apparatuses has been presented, in order to avoid conflicting results in the evaluations of interaction mechanisms between EMFs and biological structures. On the basis of this approach different exposure systems, which are currently used in various research programs for the evaluation of possible carcinogenic effects induced by EMFs, have been designed and characterized.

Great importance has been given to the design of exposure systems for the remote control of nanomachines by EMFs. In particular, an helical coil applicator has been realized and experiments have been carry out in order to better understand the interaction mechanism between EMFs and DNA structures conjugated to metal nanocrystals. The obtained results of the radiofrequency exposures of nanoparticle/biomolecule conjugates (the nanomachines) highlighted the thermal nature of the observed effect, due to a strong coupling of the sample with the electric field present inside the helical applicator. DNA denaturation under RF exposure is probably caused by bulk heating of the solution, and the differences between the conjugated and unconjugated U.V. behaviour are reduced to the intrinsinc different molar absorbance of the conjugated form with respect to the hairpin alone. In this frame, however, the possibility of remotely inducing a defined effect on a nanoparticle by means of non-optical electromagnetic radiations appeared particularly attractive, neverthless this sector of research requires multidisciplinary efforts. One of the main crucial aspects emerging from the preliminary study on the remote control of biological machine by EMFs was the need of realizing exposure systems opportunely designed for this kind of bioexperiments.

This work has been shown to originally contribute to the development of exposure systems for the remote control of nanomachines and biological processes by EMFs. Infact, in order to highlight reversible effects induced by the radiation, the designed applicator has been integrated with a fiber optic apparatus, to carry out spectrophotometric analysis contemporary to the exposures, and with a unit for the thermal monitoring. In addition, a new kind of EM applicator to be

used in this context has been designed. A theoretical model of a twin tape helical applicator has been developed in order to minimize the electric field with respect to the magnetic one; further the performances of the applicator, which included the sample, were determined by numerical simulations. The good numerical results encouraged to realize an exposure system to be used both for the remote control of biological nanomachines and for *in vitro* experiments of selective hyperthermia by using magnetic nanoparticles. To this end a numerical analysis of the applicator integrated with a thermostating control of the samples, and with a unit for the spectrophotometric analysis during the exposures, has been carryed out. The obtained numerical results have been very satisfactory; for this reason the simulated model has been realized and a first preliminary experimental characterization has been performed.

This exposure system, for our best knowledge, resulted to be quite innovative, and is the basis for the design and development of systems for industrial, diagnostic and therapeutic applications, although, as future perspectives it is necessary a full experimental characterization in order to best perform the optimization of the applicator.

Acknowledgments

I wish to thank people who helped me during this doctoral studies period.

In particular, I would like to give my most sincere thanks to my tutor, Professor Rita Massa, she patiently gave me many valuable suggestions during these years and helped me every day to improve my studies and results.

My gratitude also goes to Professor Ovidio Mario Bucci for his helpful suggestions and stimulating discussions on the remote control of nanomachines by EM fields and to Dr. Enrico Maria Bucci, Science Manager of the Bioindustry Park Canavese in Ivrea (TO), who encouraged and supported me in the development of my last research activity.

Moreover I want to thank the coordinator of the Ph. D. Course, Professor Giovanni Poggi, for his politeness and patience.

A great thank goes to Dr. Maria Rosaria Scarfì and the research group of the Bioelectromagnetic Laboratory at CNR-IREA in Naples for their support and suggestions during my doctoral study.

I wish also to thank Dr. Domenica Musumeci of the CNR-IBB in Naples for all days spent in laboratory with me during the experimental research activity.

A great thank goes to Giovanni Petraglia for his helpful suggestions and support and to all friends of the department of Electronic and Telecommunication Engineering, Michele, Raffaella, Gerardo, Giuseppe. Many thanks also to ADAG Group of Department of Aerospatial Engineering in Naples for helped me in solving some practical aspects of my activity.

Many other people deserve my thanks for they, in many ways, helped me in the years of my Ph.D. studies.

Finally I wish to thank my family for its support and express my loving thanks to my husband Ferdinando.